JOURNAL OF PETROLOGY | VOLUME 51 | NUMBER 7 | PAGES 1381–1416 | 2010 | doi:10.1093/petrology/egq023

Formation of High-Mg Diorites through Assimilation of Peridotite by Monzodiorite Magma at Crustal Depths

QING QIAN[1,2]* AND JÖRG HERMANN[2]

[1]KEY LABORATORY OF MINERAL RESOURCES, INSTITUTE OF GEOLOGY AND GEOPHYSICS, CHINESE ACADEMY OF SCIENCES, BEIJING 100029, CHINA

[2]RESEARCH SCHOOL OF EARTH SCIENCES, THE AUSTRALIAN NATIONAL UNIVERSITY, CANBERRA, ACT 0200, AUSTRALIA

RECEIVED OCTOBER 29, 2009; ACCEPTED APRIL 23, 2010
ADVANCE ACCESS PUBLICATION MAY 21, 2010

The 134–130 Ma Han-Xing diorite–monzodiorite complex intrudes the central part of the North China block (NCB). The high-Mg diorites have intermediate SiO_2, high MgO, Cr and Ni contents, elevated Mg-numbers (Mg#), and are characterized by high Sr and Ba, highly fractionated rare earth elements (REE), and strong Nb and Ta depletions. These geochemical signatures are similar to those of high-Mg adakite and sanukitoid magmas that form through complex crust–mantle interactions. We have investigated felsic magma–peridotite interactions in the Han-Xing diorite complex by undertaking a detailed petrological and bulk-rock and mineral trace element study. The high-Mg diorites contain olivine xenocrysts and dunite xenoliths that have been partly resorbed by the quartz-bearing matrix. These textures, coupled with the high Cr and Ni, and low Ca, Al, P, Y, Sc and Zr contents, provide evidence that the olivines were derived from a depleted peridotite. The assimilation of olivine produced diorite with highly variable MgO, Cr, Ni and Mg# values. However, all rocks have similar incompatible element patterns, indicating that they originate from a common pristine magma. The relative timing of olivine assimilation is constrained by reversely zoned clinopyroxene and amphibole crystals. The cores of the reversely zoned minerals have low Mg# values (clinopyroxene, ~75; amphibole, ~60) and REE characteristics indicating an origin by crystallization from a felsic magma compositionally similar to the monzodiorites. Inclusions of andesine, K-feldspar and biotite are present in the low-Mg# cores of reversely zoned clinopyroxenes, and are further proof of the felsic character of the pristine magma. The high-Mg (up to 90) midsections of the reversely zoned minerals have high Cr and Ni contents and lower but subparallel REE, indicating assimilation of peridotite by the monzodiorite magma. An eclogite residue for the pristine magma is precluded by the presence of plagioclase inclusions, and low Na_2O and Al_2O_3 and unfractionated heavy REE in the low-Mg# cores of the reversely zoned clinopyroxenes. The maximum depth of the peridotite assimilation is estimated to be ~20 km, using the Al-in-amphibole geobarometer for the high-Mg# midsection of a reversely zoned amphibole. This provides further evidence that the interaction of felsic magma with peridotite occurred at crustal rather than mantle depths. We suggest that the peridotite was emplaced at middle or upper crustal levels by previous orogenic processes. The original monzodiorite magma was probably produced in an extensional setting by partial melting of lower crust. Our observations indicate that the delamination model cannot be applied to the petrogenesis of the Han-Xing high-Mg diorite. The interaction of felsic melt with ultramafic rocks at crustal pressures has not been considered as a mechanism for the generation of high-Mg adakites and sanukitoids so far. This might have important implications for crustal evolution. Whereas in previous models sanukitoids have been related to either crustal growth by partial melting of enriched mantle peridotite or crust destruction through lower crust delamination, in the case reported here, they document crustal fractionation through anatexis of lower crustal rocks.

KEY WORDS: *high-Mg diorite; North China block; sanukitoid; intra-continental; trace element*

*Corresponding author. Present address: Key Laboratory of Mineral Resources, Institute of Geology and Geophysics, Chinese Academy of Sciences, Beijing 100029, China. Telephone: 86-10-82998248. Fax: 86-10-62010846. E-mail: qianqing@mail.igcas.ac.cn

INTRODUCTION

High-Mg andesitic rocks (HMAs, denoting high-Mg adakite and sanukitoid) are puzzling because they have geochemical characteristics typical of partial melts formed in the crust as well as in the mantle. On one hand they have high MgO, Ni and Cr abundances and high Mg-numbers [Mg#, =100Mg/(Mg + Fe)] as are common for melts originating in the mantle, but on the other hand they display an enrichment in large ion lithophile elements (LILE), strong depletion in high field strength elements (HFSE, e.g. Nb, Ta and Ti), and highly fractionated rare earth elements (REE) as are typical for partial melts of mafic crustal rocks (Martin *et al.*, 1983, 2005; Defant & Drummond, 1990; Rapp *et al.*, 1991, 1999; Yogodzinski *et al.*, 1995; Smithies & Champion, 2000). Therefore, there is general consensus that HMAs originate from a complex interplay of crust–mantle interactions.

The name 'sanukitoid' was originally introduced for the Miocene high-Mg andesites from the Setouchi volcanic belt, Japan (Tatsumi & Ishizaka, 1981, 1982*a*). Later it was adopted to describe some late Archean plutonic and volcanic rocks, including diorite, monzodiorite, monzonite and trachyandesite, which were considered to possess major and trace element characteristics similar to the Setouchi sanukitoids (Shirey & Hanson, 1984; Stern *et al.*, 1989, 1990; Stevenson *et al.*, 1999; Smithies & Champion, 2000; Lobach-Zhuchenko *et al.*, 2005, 2008; Heilimo *et al.*, 2010). Late Archean sanukitoids typically have silica contents of 55–60 wt % SiO_2, Mg# ≥60, Ni > 100 ppm and Cr > 200 ppm, K_2O > 1 wt %, Sr and Ba greater than 500 ppm, Rb/Sr ratios less than 0·1, and REE patterns strongly enriched in light REE (LREE) and have small or no Eu anomalies (Stern *et al.*, 1989). They are mostly late- to post-tectonic and are volumetrically minor, but are widely distributed in Archean granite–greenstone belts (Shirey & Hanson, 1984; Stern *et al.*, 1989; Smithies & Champion, 2000; Whalen *et al.*, 2004; Halla, 2005; Kovalenko *et al.*, 2005; Martin *et al.*, 2005; Lobach-Zhuchenko *et al.*, 2005, 2008). There is a great interest in how such sanukitoid magmas form because they compositionally approximate average continental crust (Shirey & Hanson, 1984; Kelemen, 1995; Tatsumi, 2008), and thus their genesis can provide insights into the formation and evolution of the late Archean continental crust (Shirey & Hanson, 1984; Kay & Kay, 1991; Kelemen, 1995; Rudnick, 1995; Smithies & Champion, 2000; Whalen *et al.*, 2004; Martin *et al.*, 2005; Tatsumi, 2008).

The petrogenesis of sanukitoids and high-Mg adakites is still open to debate, and several models have been proposed mainly to explain how and where the original magma is generated. Tatsumi and co-workers proposed that the Setouchi sanukitoids represent a primary andesitic magma derived from melting of an enriched mantle peridotite (Tatsumi & Ishizaka, 1981, 1982*a*, 1982*b*; Tatsumi *et al.*, 2002, 2003). Observations favoring this explanation include the following: (1) the Setouchi sanukitoids contain magnesian olivine phenocrysts (Tatsumi & Ishizaka, 1981, 1982*a*, 1982*b*); (2) sanukitoids have high-Mg# and MgO, Ni and Cr values, typical of mantle-derived primitive magmas; (3) experiments show that high-Mg andesitic liquids can be in equilibrium with and produced by partial melting of hydrous peridotite (Kushiro, 1974, 2007; Mysen & Boettcher, 1975; Tatsumi, 1981, 1982; Kawasaki *et al.*, 1993; Hirose, 1997). Although late Archean sanukitoids tend to have lower MgO, Ni, Cr and Rb/Sr and much higher Na_2O, K_2O, P_2O_5, Sr and Ce abundances and Ce/Yb ratios compared with the Setouchi sanukitoids, this model has been widely accepted for the formation of Archean sanukitoids (Shirey & Hanson, 1984; Stern *et al.*, 1989; Stern & Hanson, 1991; Stevenson *et al.*, 1999; Smithies & Champion, 2000; Whalen *et al.*, 2004; Kovalenko *et al.*, 2005; Martin *et al.*, 2005). A two-stage process has been proposed (Smithies & Champion, 2000): (1) hybridization of a mantle peridotite by pristine (low-Mg#, high-silica) adakite melts derived from a subducted slab; (2) partial melting of the hybridized mantle peridotite. Similarly, some low-silica, high-Mg adakites compositionally analogous to Archean sanukitoids have also been suggested to be produced by partial melting of enriched mantle peridotite (Martin *et al.*, 2005; Danyushevsky *et al.*, 2008).

A second model suggests that HMAs form through assimilation of mantle peridotite by slab-derived melts (Kay, 1978; Kelemen, 1995; Yogodzinski *et al.*, 1995; Rapp *et al.*, 1999, 2010; Moyen *et al.*, 2003). Rapp (2003) incorporated adakite, tonalite–trondhjemite–granodiorite (TTG) and sanukitoid melts into one granitoid family, suggesting that these rocks mainly differ from each other by the extent of reaction between pristine slab-derived adakite magmas and mantle peridotite. High-pressure experiments provide evidence that with increasing degree of reaction Mg#, MgO, Cr and Ni increase and SiO_2 decreases, whereas the overall shape of the incompatible element patterns in the hybridized HMAs magma does not change significantly with respect to that of the pristine adakite melts, despite some increase in the absolute concentrations because melt is consumed in the assimilation reaction (Rapp *et al.*, 1999, 2010; Rapp, 2003).

Both models presented above of sanukitoid and high-Mg adakite magma formation are closely related to subduction processes, where the required SiO_2 and trace element enriched melt derives from partial melting of subducted mafic crust (generally assumed to be eclogitized) at high-pressure conditions. However, granitoids with chemical characteristics similar to HMAs have also been observed in intra-continental settings, such as in the North China block (NCB) (Fig. 1). These magmatic rocks are not related to a subduction process and thus a third model has been put forward. In this model, the SiO_2 and

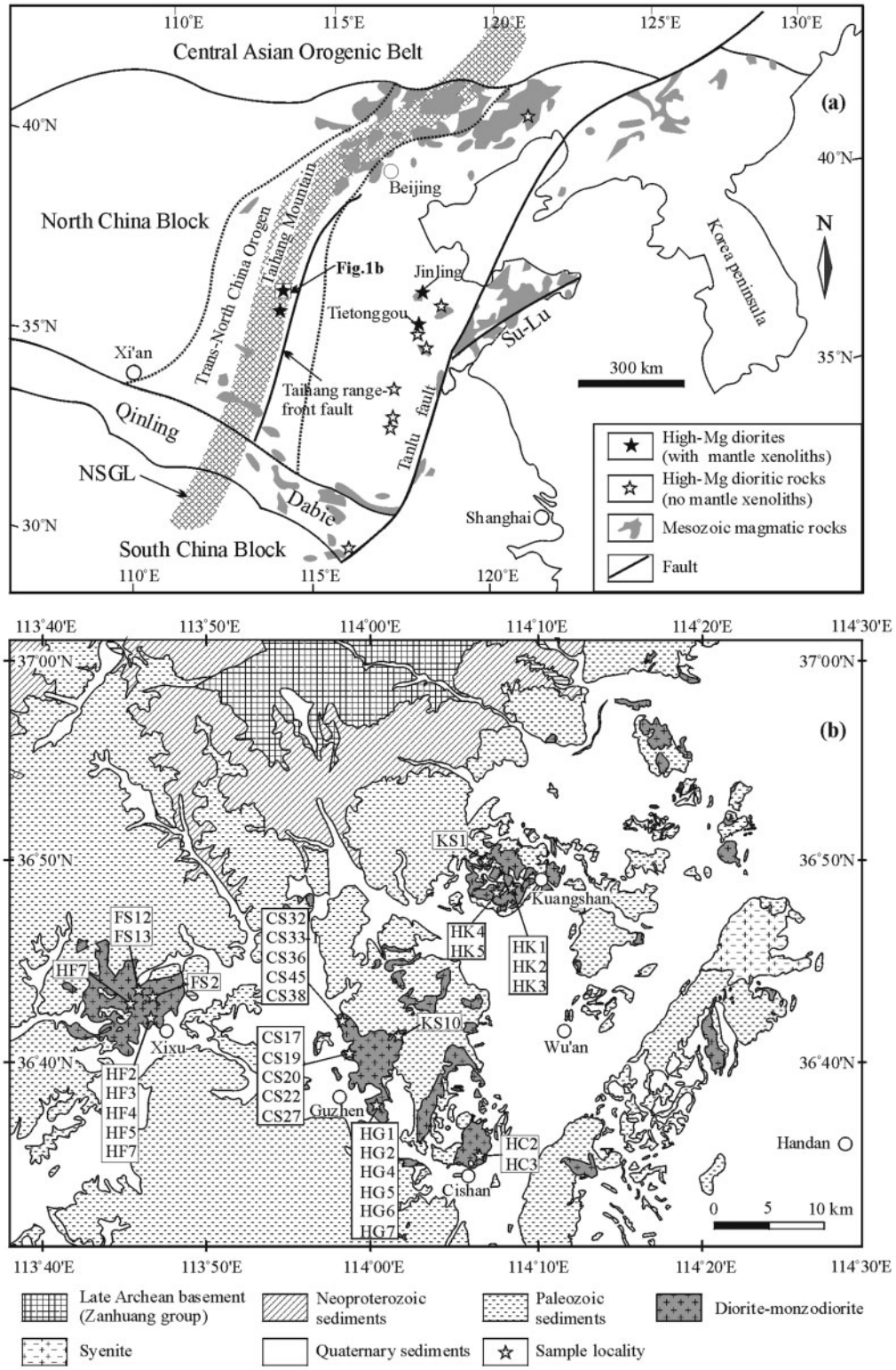

Fig. 1. (a) Simplified tectonic map showing the distribution of Mesozoic high-Mg dioritic rocks from the North China block (NCB) and the Dabie orogen. The high-Mg diorites mostly formed in the early Cretaceous (~130 Ma). Trans-North China Orogen (area between the dotted lines), after Zhao *et al.* (2001). NSGL, North–South Gravity Lineament (or Daxin'anling–Taihang gravity lineament), after Xu *et al.* (2007). (b) Regional geological map of the Han-Xing dioritic complex, modified after BGHP (1972).

trace element enriched melt derives from partial melting of delaminated and eclogitized lower-crustal mafic rocks. The partial melts then rise and interact with the inflowing mantle peridotite between the sinking, delaminated block and the lower crust (Gao *et al.*, 2004, 2006; Xu *et al.*, 2006*a*, 2006*b*, 2008, 2009; Huang *et al.*, 2008). Whalen *et al.* (2004) proposed that post-collisional delamination of thickened lower crust was probably responsible for formation of Archean sanukitoids in the western Superior Province, Canada. Lower-crust delamination is believed to be an important mechanism not only for generating magmas with typical trace element signatures of the continental crust but also for creating the andesitic bulk composition of the continental crust (Kay & Kay, 1991l, 1993; Rudnick, 1995; Rudnick & Gao, 2003). It is notable that in all three of the models proposed, the initial partial melting of the mafic crust and/or assimilation of ultramafic rocks occurs at mantle depths.

In this study, we present the results of a petrological and geochemical study of a Mesozoic high-Mg diorite–monzodiorite complex from Handan-Xingtai (Han-Xing) in the central part of the NCB. The main aims are: (1) to show that high-Mg diorites from the Han-Xing complex are geochemically similar to sanukitoids and high-Mg adakites elsewhere; (2) to provide detailed major and trace element compositional profiles through magmatic clinopyroxene and amphibole crystals, which can be used to characterize the original 'adakite-like' melt as well as the relative timing of the interaction of this melt with peridotite; and (3) to provide constraints on the depth of peridotite assimilation by this felsic 'adakite-like' magma. The results show that none of the proposed models so far is able to explain the key observations on these rocks and, thus, we propose an alternative petrogenetic model for formation of sanukitoids and high-Mg adakites.

GEOLOGICAL BACKGROUND

The NCB is underlain by Archean–Paleoproterozoic basement rocks, including granulite, amphibolite, TTG gneiss, charnockite, migmatite and supercrustal formations. It was formed mainly by collision of the Eastern and Western blocks at ~1·8 Ga along the Trans-North China Orogen (Zhao *et al.*, 2001l, 2005) (Fig. 1a). From the Mesoproterozoic to the Paleozoic, the block was relatively stable and thick layers of platform sediments were deposited on the basement. The NCB was amalgamated with the Siberian block probably in the late Paleozoic (Sengör *et al.*, 1993; Zhang *et al.*, 2009) and collided with the South China block in the late Permian–early Triassic (Li *et al.*, 2000; Ayers *et al.*, 2002), leading to the formation of the Central Asian and Qinling–Dabie–Sulu orogenic belts, respectively.

The eastern part of the NCB (to the east of the Taihang Mountains, Fig. 1a) experienced complex compression and extension from late Triassic to Jurassic times, accompanied by the formation of substantive granitic and mafic rocks (Deng *et al.*, 2004; Wu *et al.*, 2005*c*; Lin *et al.*, 2007, 2008). In the late Mesozoic (from ~140 Ma to ~60 Ma), crustal extension and lithosphere thinning were widespread in East Asia, including Baikal, eastern Mongolia, NE China, and the eastern parts of North and South China (Liu *et al.*, 2008). A series of NE–SW- to NNE–SSW-trending strike-slip faults (e.g. the Tan-Lu fault and the Taihang range-front fault), metamorphic core complexes and widespread magmatic rocks (dominantly intermediate to acid) developed in the eastern NCB during this period, most intensively at about 125 ± 5 Ma (Yang & Li, 1980; Xu *et al.*, 1987; Ratschbacher *et al.*, 2000; Zhu *et al.*, 2001l, 2003, 2004, 2005; Wu *et al.*, 2005*a*; Lin *et al.*, 2007, 2008; Liu *et al.*, 2008). The processes that are responsible for the tectonics and magmatism in the late Mesozoic may be related to the deep-angle, oblique (to the north) subduction of the Izanagi plate (Engebretson *et al.*, 1985; Maruyama *et al.*, 1997; Zhou & Li, 2000), but are still open to debate. Currently the NCB is separated into two topographically and tectonically different regions by a giant NNE–SSW-trending linear zone of Bouguer gravity gradient (the North–South Gravity Lineament) which overlaps the Trans-North China Orogen and the Taihang Mountains (Ma, 1989; Xu *et al.*, 2007, and references therein) (Fig. 1a), with crustal thickness varying from ~30 km beneath the eastern part to ~40 km beneath the central part of the NCB (Zheng *et al.*, 2006; Chen, 2009).

FIELD RELATIONS AND SAMPLE DESCRIPTION

The Han-Xing diorite complex is located at the southern part of the Taihang Mountains. Exposed plutons dominantly consist of diorites and monzodiorites, cropping out over an area of ~340 km^2 in Cambrian–Permian strata (mainly Ordovician carbonates) (Fig. 1b). Emplacement of the plutons was controlled by NNE–SSW-trending faults (BGHP, 1972; Xu & Gao, 1990). Major plutons include the Fushan (NW of the Xixu county), Guzhen, Cishan and Kuangshan bodies, which are connected below the surface according to drill-hole exploration (Huang & Xue, 1990*a*). Amphibole diorites dominate the Fushan and Guzhen bodies, whereas monzodiorites dominate the Cishan and Kuangshan bodies, showing a trend of becoming less mafic from west to east. A syenite pluton, the Hongshan body, crops out ~20 km to the east of the Kuangshan body. Sensitive high-resolution ion microprobe (SHRIMP) zircon U–Pb ages of the dioritic rocks and syenites are in the range 134–130 Ma (Chen *et al.*, 2008; our unpublished SHRIMP zircon U–Pb data). Mantle xenoliths of harzburgite, lherzolite and dunite have been found

in the Fushan diorites (Huang & Xue, 1990*b*; Xu & Lin, 1991; Song & Feng, 1999; Xu *et al.*, 2009, 2010). Angular enclaves of Archean–Permian country rocks (e.g. gneiss, plagioclase amphibolite, quartzite, and carbonate) occur in all of the plutons.

Amphibole diorite samples were taken from the Fushan and Guzhen plutons (Fig. 1b). They are grayish, massive and dominantly medium-grained, with amphiboles locally reaching ~1 cm in length. Greenish olivine crystals (0·5–4 mm in size) are abundant (0–10·2 vol. %, by microscope statistics, Table 1) and evenly distributed in some diorite samples, which are dark in color and have fine-grained dioritic matrix. The olivine-bearing diorite samples are all from the chilled margin of the Guzhen pluton. Monzodiorite samples (e.g. CS38, HK1 and HK4) from the Guzhen, Cishan and Kuangshan bodies are pink-colored and medium-grained.

PETROGRAPHY

Rock-forming minerals of the major diorites include amphibole (up to 40%), clinopyroxene (0–15%), biotite (0–5%), plagioclase (45–65%), K-feldspar (3–10%) and quartz (<5%). Accessory minerals are magnetite, titanite, apatite, zircon, and rare epidote. Euhedral–subhedral plagioclase crystals with well-developed compositional zoning form a connected framework, and K-feldspar and quartz occur as intergranular phases. Amphibole is euhedral–subdedral and brown–greenish. Clinopyroxene is euhedral to anhedral and mostly less than 1·5 mm in size, locally replaced by amphibole and/or biotite at the rim. Rarely, reversely zoned (higher Mg# in the midsection than in the core) amphibole crystals are found, containing inclusions of plagioclase, K-feldspar, apatite, rutile, titanite and magnetite at the core.

Olivine xenocrysts and rare dunite xenoliths are present in some fine-grained (plagioclase mostly 0·2–1·2 mm in length) diorite samples (e.g. CS17, CS19, CS20, CS27, CS32, CS33-1, CS36 and CS45). The dunite xenoliths are elliptical in outline, and olivine crystals contact each other with arcuate or serrated boundaries (Fig. 2a and b). Separate olivine crystals are round, elliptical or skeletal in shape, indicating that they have been resorbed. Some of them are deformed and display kink bands (Fig. 2c) or wavy extinction. Locally the olivine is partially or completely serpentinized (Fig. 2f). All investigated olivine crystals are normally zoned with Mg-rich cores and Fe enrichment at the rims (Fig. 2d). Interstitial quartz is ubiquitous in the dioritic matrix, even in close proximity to dunite and olivine xenocrysts (Fig. 2e and g). Reactions between dunite or olivine and the matrix lead to the formation of a thin corona (<100 μm wide) of orthopyroxene, clinopyroxene and magnetite symplectite (orthopyroxene always forms at the inside) (Fig. 2e) and amphibole, or an overgrowth of normally zoned clinopyroxene microcrystals. Occasionally, tiny patches of mineral aggregates composed of orthopyroxene, clinopyroxene, amphibole, phlogopite, andesine and/or chromite occur inside the olivine xenocrysts by reaction between olivines and melt that infiltrated through cracks (e.g. Fig. 2d). Reversely zoned clinopyroxene phenocrysts (1–3 mm in size) form beside olivine (Fig. 2f and g) or separately. Some of the reversely zoned clinopyroxenes contain plagioclase, K-feldspar and biotite inclusions in the core (Fig. 2g and h).

The monzodiorite is composed of amphibole (0–10%), clinopyroxene (0–5%), plagioclase (60–75%), K-feldspar (10–15%) and quartz (3–10%). Accessory magnetite, titanite, apatite, and zircon are present. Plagioclase is euhedral and normally zoned, forming a connected framework. Feldspars are slightly to moderately sericitized, and have analcime grains at the interstices.

ANALYTICAL METHODS

Rock samples of diorite and monzodiorite were crushed in a jaw crusher and then 30 g subsamples were ground in an agate mill to less than 200 mesh (~80 μm). Major oxides were analyzed by X-ray fluorescence (XRF) using a Rigaku RIX-2100 spectrometer at National Taiwan University and Key Laboratory of Continental Dynamics in Northwest University, China. Analytical precision and accuracy are estimated to be <2% for most major oxides and <5% for MnO and P_2O_5, with totals within 100·0 ± 1·0 wt %. Loss on ignition (LOI) was measured after heating to 1000°C. Trace element concentrations were determined by inductively coupled plasma mass spectrometry (ICP-MS) using a Finnigan Element at the Institute of Geology and Geophysics (IGG), Chinese Academy of Sciences in Beijing, China. Sample powders were digested in a mixture of super-pure HNO_3 and HF in high-pressure Teflon bombs, evaporated to near dryness and refluxed with super-pure HNO_3, using 1 ml 500 ppb indium as an internal standard. Duplicate analysis of samples and rock standards (GSR1, GSR2, GSR3, PM-S and MRG1) gives relative standard deviations better than 10% for most trace elements and <20% for V, Cr, Co, Ni, Th and U.

Major element compositions of rock-forming minerals were determined by electron microprobe (EMP) using a Cameca SX 51 and a Jeol JXA 8100 at the IGG and a Jeol 6400 scanning microscope in EMU, Australian National University (ANU). Accelerating voltage, beam current, spot diameter and peak counting time for EMP analyses were 15 kV, 20 nA, 5 μm and 20 s, respectively. Trace element profiles across clinopyroxene and amphibole crystals were determined by laser-ablation (LA)-ICP-MS using an Agilent 7500 coupled to an ArF (193 nm) Excimer laser, at the Research School of Earth Sciences (RSES) in ANU. A circular beam of 70, 112, 142 or 247 μm in diameter

Table 1: Representative analyses of high-Mg diorites and monzodiorites

	High-Mg diorite											
Sample:	ENCB	CS17	CS19	CS20	CS27	CS32	CS33-1	CS36	CS45	FS2	FS12	FS13
Olivine:		5·8%	3·5%	yes	yes	yes	10·2%	yes	yes	no	no	no
SiO_2	59·33	53·62	53·58	54·99	52·72	54·44	47·36	54·31	54·02	55·86	57·98	53·07
TiO_2	0·71	0·63	0·63	0·63	0·64	0·69	1·51	0·65	0·62	0·67	0·66	0·77
Al_2O_3	15·53	13·12	13·15	14·46	12·78	14·37	11·63	14·63	13·58	15·28	16·71	15·46
Fe_2O_3	6·54	8·34	8·29	8·26	8·55	8·40	11·32	8·59	8·07	8·25	7·11	9·49
MnO	0·10	0·13	0·12	0·12	0·12	0·12	0·13	0·12	0·12	0·09	0·08	0·14
MgO	4·10	10·02	10·19	7·32	11·29	8·49	14·39	8·04	9·28	5·39	3·17	6·10
CaO	5·32	6·51	6·49	6·72	6·58	6·40	8·86	6·92	6·50	6·49	5·99	8·05
Na_2O	4·28	3·08	3·17	3·48	2·95	3·45	2·16	3·88	3·25	4·32	4·40	3·20
K_2O	2·04	2·45	2·40	2·63	2·35	2·36	1·94	1·78	2·46	1·62	2·45	1·83
P_2O_5	0·25	0·30	0·30	0·31	0·29	0·30	0·13	0·33	0·29	0·32	0·32	0·35
LOI		1·31	1·18	0·71	1·40	0·53	0·33	0·33	1·34	1·29	0·67	1·51
Total		99·51	99·50	99·63	99·67	99·55	99·73	99·58	99·53	99·58	99·54	99·97
Mg#	60	72·8	73·2	66·3	74·6	69·2	73·9	67·5	71·9	59·2	49·8	58·8
A/CNK	0·83	0·67	0·67	0·69	0·66	0·72	0·53	0·70	0·68	0·74	0·80	0·71
Li	18·9	15·3	14·9	17·1	16·0	12·3	11·3	10·6	15·8	7·2	13·8	22·3
Sc	14·7	18·7	18·9	21·4	19·3	18·8	39·7	18·4	19·2	22·5	16·3	25·5
V	120	146	161	183	149	169	335	173	156	175	154	212
Cr	183	538	529	318	538	398	759	330	470	169	29·4	180
Co	35·2	37·2	42·3	34·2	45·1	36·1	60·2	34·5	38·7	25·0	16·1	30·8
Ni	96·4	323	345	191	416	255	487	213	321	48·6	7·47	58·3
Cu	36·1	54·2	48·8	23·5	25·4	19·1	8·75	8·01	58·3	6·80	1·24	45·6
Zn	66·6	79·956	74·8	67·0	76·8	75·2	94·8	73·1	78·8	58·8	33·0	92·3
Ga	18·6	16·6	16·1	18·1	15·9	17·8	15·3	17·9	17·3	18·4	19·7	19·3
Rb	49·9	55·4	55·5	62·0	54·6	54·2	40·3	39·0	61·1	15·7	31·4	34·6
Sr	733	673	721	770	690	671	428	790	728	704	769	761
Y	15·6	14·3	14·8	15·6	14·1	15·7	20·9	15·0	15·6	17·5	15·9	18·3
Zr	157	124	110	112	111	111	79	93	114	114	140	102
Nb	6·87	4·94	5·07	5·01	4·67	5·14	4·66	4·27	4·95	6·45	5·92	5·97
Cs	4·72	1·96	1·63	0·84	1·72	1·76	1·20	1·42	1·19	0·269	0·260	0·805
Ba	934	834	1032	1024	920	1078	728	989	1148	1340	1441	954
La	29·1	24·6	25·3	26·1	23·8	25·4	14·2	24·9	26·0	27·5	25·6	25·7
Ce	58·0	49·2	48·2	50·5	47·7	49·8	35·2	48·8	51·2	52·6	49·6	52·4
Pr	6·87	6·17	6·25	6·42	6·08	6·28	5·34	6·20	6·47	6·74	6·29	6·91
Nd	26·6	22·5	25·0	24·9	24·1	24·1	26·0	24·1	25·5	27·0	25·0	27·8
Sm	4·76	4·38	4·97	5·11	4·88	4·84	6·58	4·75	5·06	5·49	4·80	5·76
Eu	1·38	1·39	1·41	1·57	1·49	1·42	1·87	1·58	1·47	1·67	1·66	1·82
Gd	3·98	3·77	3·73	4·01	3·94	3·77	5·55	3·95	3·85	4·37	4·11	4·71
Tb	0·55	0·524	0·540	0·575	0·572	0·553	0·845	0·583	0·546	0·669	0·587	0·695
Dy	2·91	2·80	2·85	2·89	2·98	2·95	4·64	3·05	2·93	3·53	3·13	3·77
Ho	0·56	0·548	0·552	0·594	0·604	0·588	0·925	0·608	0·591	0·690	0·618	0·750
Er	1·53	1·41	1·50	1·59	1·58	1·61	2·28	1·61	1·59	1·93	1·63	2·03
Tm	0·23	0·209	0·235	0·243	0·232	0·250	0·321	0·243	0·249	0·297	0·249	0·309
Yb	1·46	1·35	1·55	1·58	1·49	1·60	2·07	1·52	1·58	1·86	1·64	1·84
Lu	0·23	0·211	0·235	0·238	0·236	0·238	0·295	0·235	0·238	0·293	0·264	0·291
Hf	4·23	3·12	2·75	2·89	2·95	2·82	2·58	2·57	2·84	3·24	3·65	2·96
Ta	0·49	0·268	0·261	0·366	0·232	0·253	0·236	0·206	0·248	0·371	0·357	0·297
Pb	15·7	9·40	9·79	5·98	8·87	9·17	5·76	7·75	9·16	4·16	4·65	9·04
Th	6·19	2·43	2·49	3·37	2·31	2·65	1·31	2·08	2·65	4·25	3·85	2·63
U	2·14	0·710	0·726	0·844	0·679	0·622	0·314	0·529	0·711	0·819	0·541	0·521
Nb/La	0·26	0·20	0·20	0·19	0·20	0·20	0·33	0·17	0·19	0·23	0·23	0·23
La/Yb	20	18	16	17	16	16	7	16	17	15	16	14
Sr/Y	51	47	49	49	49	43	20	53	47	40	49	42
Dy/Yb	2·0	2·1	1·8	1·8	2·0	1·8	2·2	2·0	1·9	1·9	1·9	2·0

(Continued)

Table 1: Continued

	High-Mg diorite						Monzodiorite				
Sample:	HF2	HF3	HF4	HF5	HF7	HG7	CS38	CS43	HG1	HG2	HG4
Olivine:	no	no	no	no	no	no	no	no	no	no	no
SiO_2	52·88	56·93	57·55	57·37	54·13	57·46	58·65	56·37	58·58	58·52	58·28
TiO_2	0·82	0·66	0·67	0·68	0·80	0·75	0·56	0·57	0·54	0·53	0·58
Al_2O_3	15·19	16·30	16·82	16·04	16·53	16·31	17·23	17·44	17·31	17·22	17·57
Fe_2O_3	9·55	7·74	7·13	7·43	9·27	7·39	6·50	8·10	6·53	6·29	6·26
MnO	0·15	0·12	0·07	0·07	0·09	0·06	0·12	0·06	0·07	0·08	0·05
MgO	6·28	4·11	2·93	4·17	3·95	3·43	2·00	2·73	2·09	2·00	2·09
CaO	7·79	6·08	5·35	5·68	6·55	4·87	5·27	5·59	5·18	5·31	3·92
Na_2O	3·83	4·29	4·78	6·63	5·20	5·65	4·26	4·54	5·56	5·05	8·83
K_2O	2·24	2·71	2·81	0·51	2·05	3·03	3·16	2·85	2·07	2·90	0·53
P_2O_5	0·37	0·30	0·33	0·32	0·38	0·35	0·29	0·41	0·27	0·28	0·28
LOI	0·72	0·64	1·21	1·13	0·91	0·73	1·58	1·23	0·91	0·97	1·58
Total	99·81	99·86	99·66	100·02	99·86	100·03	99·62	99·89	99·12	99·14	99·97
Mg#	59·4	54·1	47·8	55·5	48·7	50·8	40·6	42·8	41·6	41·4	42·6
A/CNK	0·66	0·77	0·81	0·74	0·73	0·76	0·86	0·84	0·83	0·82	0·79
Li	11·3	16·7	8·0	13·6	13·4	0·7	26·8	7·2	5·0	5·6	0·1
Sc	21·0	15·3	12·7	15·0	17·2	12·4	8·9	11·3	9·1	8·6	4·2
V	219	176	153	171	207	177	117	127	119	99	113
Cr	236	91·7	23·3	121	50·7	77·0	0·537	2·47	26·8	35·8	24·3
Co	31·1	21·7	15·1	19·2	20·7	17·2	12·9	13·3	8·39	9·95	7·16
Ni	58·7	31·2	8·24	37·1	23·4	65·7	0·384	4·17	13·1	84·6	12·0
Cu	18·4	11·0	12·1	14·8	15·7	29·9	3·90	12·9	14·8	41·3	13·7
Zn	58·6	48·5	27·4	28·8	36·4	27·7	58·5	26·2	30·5	31·9	14·0
Ga	80·1	96·5	96·7	39·0	99·4	79·6	20·9	20·9	139	129	30·5
Rb	30·4	45·2	31·4	3·52	16·2	23·8	51·2	39·9	20·7	37·6	9·01
Sr	661	741	737	776	775	713	719	838	869	755	551
Y	18·5	15·6	16·8	15·6	18·5	14·7	17·4	16·4	18·3	18·0	18·1
Zr	113	149	147	137	135	167	163	112	167	82	171
Nb	6·35	6·65	5·93	6·41	6·77	7·50	6·34	3·94	6·23	6·04	6·44
Cs	0·171	0·349	0·144	0·195	0·118	0·084	0·416	1·15	0·179	0·169	0·170
Ba	1027	1294	1256	386	1303	945	1212	1254	1957	1812	231
La	27·7	30·8	31·5	34·5	34·8	36·1	31·5	33·1	32·1	33·2	28·8
Ce	57·8	59·1	64·2	65·7	69·9	63·2	58·6	60·8	63·2	65·4	60·3
Pr	7·44	6·64	7·61	7·51	8·14	6·88	7·54	7·69	7·47	7·71	7·00
Nd	30·6	25·2	29·8	28·9	32·1	26·2	29·2	30·8	29·6	30·7	28·4
Sm	6·01	4·75	5·36	5·25	5·98	4·90	5·58	6·16	5·56	5·51	5·19
Eu	1·92	1·59	1·79	1·69	1·96	1·67	1·70	2·02	1·92	1·95	1·66
Gd	5·39	4·20	4·65	4·56	5·34	4·45	4·46	4·87	5·02	4·91	4·59
Tb	0·714	0·566	0·611	0·576	0·688	0·539	0·654	0·687	0·640	0·631	0·619
Dy	3·83	3·14	3·37	3·17	3·90	2·95	3·56	3·36	3·64	3·52	3·49
Ho	0·726	0·621	0·663	0·601	0·758	0·550	0·681	0·677	0·711	0·683	0·700
Er	2·05	1·78	1·93	1·81	2·11	1·62	1·94	1·74	2·08	2·10	2·06
Tm	0·295	0·259	0·270	0·240	0·290	0·231	0·295	0·269	0·310	0·291	0·301
Yb	1·91	1·70	1·79	1·65	1·93	1·45	1·91	1·67	1·99	1·87	2·01
Lu	0·274	0·260	0·276	0·248	0·268	0·223	0·301	0·240	0·305	0·289	0·299
Hf	3·52	4·12	4·31	4·07	3·83	4·62	4·19	3·13	4·86	3·02	4·95
Ta	0·348	0·427	0·353	0·368	0·341	0·393	0·309	0·284	0·358	0·330	0·393
Pb	5·34	7·29	3·71	2·76	9·23	4·25	8·95	4·81	7·56	7·72	1·85
Th	4·89	4·45	4·16	7·18	3·47	3·43	2·96	3·30	3·04	3·23	3·12
U	1·16	1·16	0·856	1·40	0·995	1·89	0·790	1·29	0·843	0·906	0·984
Nb/La	0·23	0·22	0·19	0·19	0·19	0·21	0·20	0·12	0·19	0·18	0·22
La/Yb	15	18	18	21	18	25	17	20	16	18	14
Sr/Y	36	48	44	50	42	49	41	51	48	42	31
Dy/Yb	2·0	1·8	1·9	1·9	2·0	2·0	1·9	2·0	1·8	1·9	1·7

(Continued)

Table 1: Continued

	Monzodiorite										
Sample:	HG5	HG6	HC2	HC3	KS1	KS10	HK1	HK2	HK3	HK4	HK5
Olivine:	no	no	no	no	no	no	no	no	no	no	no
SiO_2	60·95	57·61	58·38	58·92	60·16	61·12	56·06	57·53	57·20	63·03	66·07
TiO_2	0·53	0·82	0·57	0·57	0·58	0·51	0·64	0·63	0·64	0·38	0·34
Al_2O_3	17·05	16·44	17·24	17·73	16·99	16·48	16·87	16·73	17·16	16·68	17·06
Fe_2O_3	5·52	8·17	7·08	6·67	5·98	5·59	7·84	7·47	8·00	4·58	3·26
MnO	0·07	0·09	0·12	0·14	0·04	0·06	0·13	0·13	0·14	0·09	0·07
MgO	1·87	2·65	2·02	1·88	1·61	2·38	2·24	2·04	2·27	1·31	0·84
CaO	4·73	4·67	5·44	5·86	4·37	4·15	5·12	4·06	4·32	2·49	1·77
Na_2O	6·29	5·49	4·95	4·89	4·63	4·65	5·46	5·75	5·59	5·51	5·60
K_2O	1·63	3·26	2·50	2·45	4·23	3·42	3·66	3·81	3·49	5·13	4·93
P_2O_5	0·27	0·34	0·31	0·30	0·29	0·26	0·40	0·36	0·39	0·21	0·13
LOI	0·63	0·83	0·65	0·49	0·67	1·03	1·43	1·11	1·26	0·43	0·52
Total	99·53	100·38	99·28	99·89	99·55	99·65	99·84	99·60	100·45	99·82	100·58
Mg#	42·9	41·8	38·8	38·5	37·4	48·6	38·8	37·7	38·6	38·8	36·4
A/CNK	0·82	0·78	0·83	0·83	0·0·84	0·87	0·76	0·80	0·82	0·87	0·96
Li	5·7	3·5	—	—	6·1	8·3	12·2	10·2	—	14·9	11·2
Sc	7·3	12·2	10·1	12·2	8·4	9·5	11·3	10·5	15·8	6·4	4·4
V	115	179	105	84	90	101	142	122	115	77	50
Cr	12·2	30·5	8·47	11·1	3·93	12·5	15·7	14·5	9·8	12·5	15·6
Co	8·25	16·5	10·6	9·74	10·8	11·0	14·9	21·7	18·8	7·81	6·27
Ni	8·39	14·4	6·40	5·58	2·24	7·96	10·9	10·1	7·87	7·33	7·06
Cu	13·7	55·0	10·3	14·0	31·1	2·85	75·2	93·6	28·9	21·3	14·3
Zn	31·9	41·9	55·9	89·8	27·0	30·7	90·5	67·3	70·0	65·1	34·9
Ga	76·8	122	21·9	22·2	21·0	19·85	83·9	68·8	21·7	62·3	59·5
Rb	19·8	61·7	38·1	44·3	50·4	42·3	92·2	97·5	90·7	112	113
Sr	681	665	936	1029	707	629	849	763	858	469	360
Y	16·8	16·9	20·0	20·8	18·7	16·4	17·5	18·3	19·6	14·8	18·2
Zr	162	180	166	167	147	144	146	173	166	156	263
Nb	6·85	8·26	6·55	6·67	8·79	6·24	6·10	7·19	5·83	8·08	9·49
Cs	0·151	0·128	0·184	0·459	0·315	0·220	0·670	0·701	0·467	1·52	1·43
Ba	946	1668	1387	1346	1109	1683	991	764	863·1	682	645
La	35·4	35·3	34·9	37·3	32·0	30·9	40·1	40·0	40·7	38·0	40·7
Ce	71·8	69·7	70·4	72·9	64·7	57·8	78·6	78·2	79·7	68·8	78·8
Pr	8·08	8·18	8·00	8·28	8·92	7·33	9·08	8·89	8·95	7·23	8·76
Nd	30·7	32·4	32·2	33·0	32·4	27·7	35·4	33·8	35·5	25·8	30·5
Sm	5·42	6·04	5·83	5·89	6·15	5·27	6·34	5·97	6·38	4·34	5·17
Eu	1·76	1·98	1·81	1·85	1·71	1·63	1·92	1·88	1·74	1·34	1·23
Gd	4·59	5·39	4·73	4·88	4·73	3·92	5·47	5·41	5·21	3·91	4·55
Tb	0·598	0·644	0·691	0·706	0·707	0·568	0·706	0·695	0·733	0·500	0·618
Dy	3·25	3·49	3·55	3·67	3·80	2·98	3·70	3·65	3·64	2·69	3·42
Ho	0·654	0·665	0·695	0·723	0·757	0·608	0·678	0·671	0·674	0·553	0·684
Er	1·85	1·80	1·98	2·06	1·97	1·66	1·89	1·94	1·83	1·56	2·01
Tm	0·273	0·255	0·300	0·320	0·304	0·259	0·255	0·280	0·267	0·225	0·299
Yb	1·82	1·66	1·94	2·06	1·98	1·68	1·67	1·78	1·66	1·59	1·99
Lu	0·271	0·231	0·306	0·325	0·300	0·259	0·235	0·265	0·251	0·230	0·291
Hf	4·68	5·10	4·13	4·15	3·98	3·66	4·20	4·72	4·03	4·72	7·02
Ta	0·410	0·466	0·416	0·428	0·503	0·339	0·328	0·461	0·338	0·429	0·577
Pb	8·19	4·51	8·65	9·86	9·23	7·28	13·9	17·0	9·73	20·05	16·50
Th	3·59	3·85	2·79	3·00	4·60	3·67	4·11	4·26	3·93	5·85	6·24
U	0·994	1·21	0·739	0·724	0·692	0·891	1·14	1·08	0·951	1·24	1·36
Nb/La	0·19	0·23	0·19	0·18	0·27	0·20	0·15	0·18	0·14	0·21	0·23
La/Yb	20	21	18	18	16	18	24	23	25	24	21
Sr/Y	41	39	47	50	38	38	48	42	44	32	20
Dy/Yb	1·8	2·1	1·8	1·8	1·9	1·8	2·2	2·1	2·2	1·7	1·7

ENCB is an average ($n = 28$) of Mesozoic high-Mg adakites (SiO_2 <62 wt %) from the eastern part of the NCB (Gao *et al.*, 2004; Xu *et al.*, 2006*a*, 2006*b*; Huang *et al.*, 2008); olivine phenocryst contents (in volume) were estimated by microscope statistics; Fe_2O_3, total Fe as ferric iron; $Mg = Mg/(Mg + 0{\cdot}9Fe^T)$; —, not analyzed.

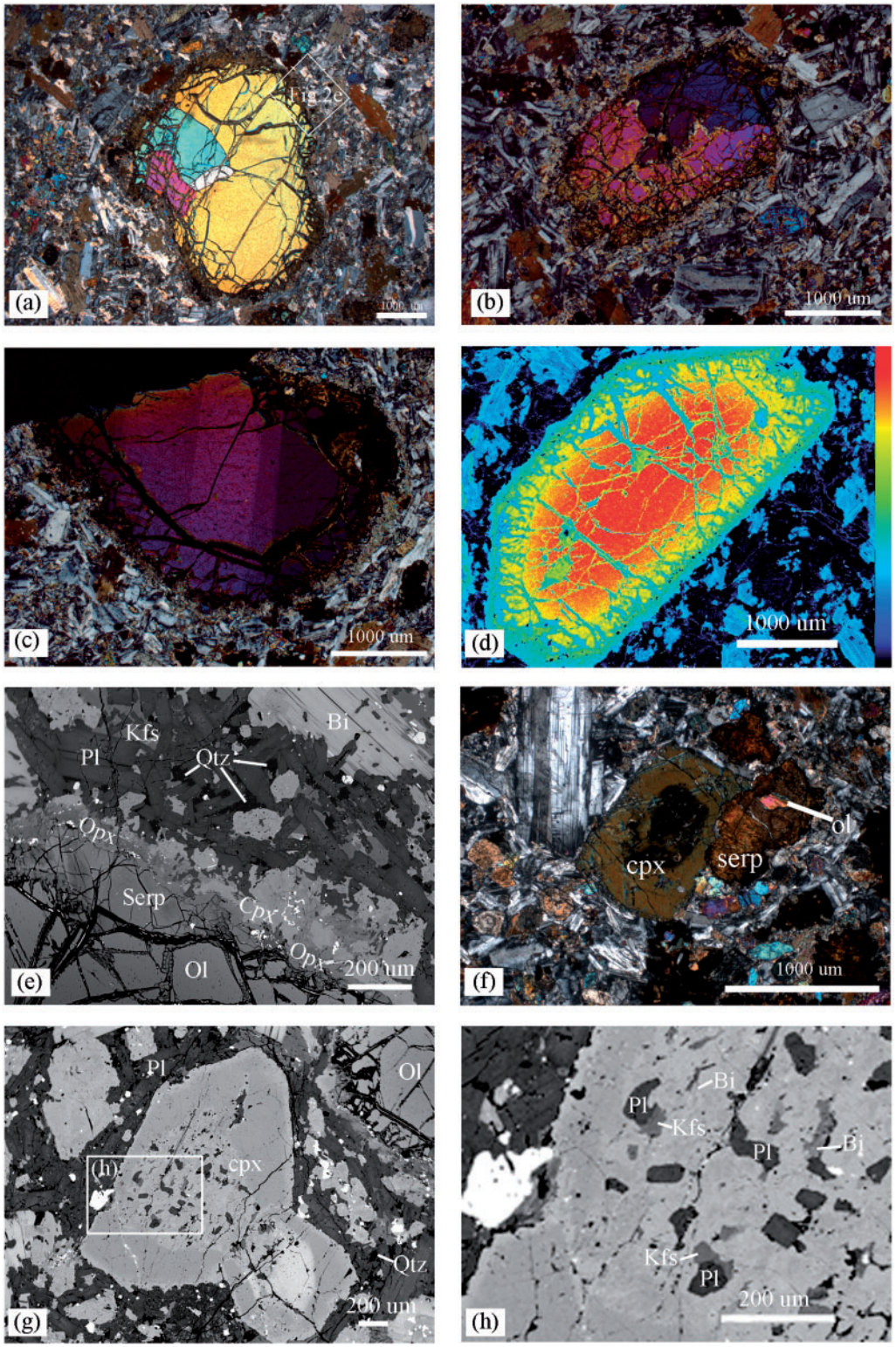

Fig. 2. Photomicrographs, X-ray map and backscattered electron (BSE) images illustrating the petrographic characteristics of the olivine-bearing high-Mg diorites. (a) An olivine aggregate (dunite xenolith) in a dioritic matrix; olivine crystals contact each other with arcuate boundaries. (b) An olivine aggregate in which olivine crystals have serrated boundaries. (c) An olivine xenocryst with kink bands (~6° variation in extinction angle). (d) X-ray map of Mg for a normally zoned olivine xenocryst with Fo = 93 at the core and Fo = 81 at the rim. The tiny patches within the olivine are aggregates of orthopyroxene, clinopyroxene, amphibole, phlogopite, andesine and/or low-Mg# chromite microcrystals, formed by reaction between olivine and melt that flowed in through the cracks. (e) BSE image showing the reaction between the dunite in (a) and quartz-bearing dioritic matrix. Orthopyroxene, clinopyroxene and magnetite (white in appearance) symplectite forms around the olivine. (f) A reversely zoned clinopyroxene next to an olivine xenocryst; the olivine has been intensively serpentinized. (g) BSE image of a reversely zoned clinopyroxene next to an olivine xenocryst; the sieve-textured core of the clinopyroxene contains plagioclase, K-feldspar and biotite inclusions. The ubiquity of interstitial quartz in the matrix should be noted. (h) An enlargement of part of (g). Bi, biotite; Cpx, clinopyroxene; Kfs, K-feldspar; Ol, olivine; Opx, orthopyroxene; Pl, plagioclase; Qtz, quartz; Serp, serpentine.

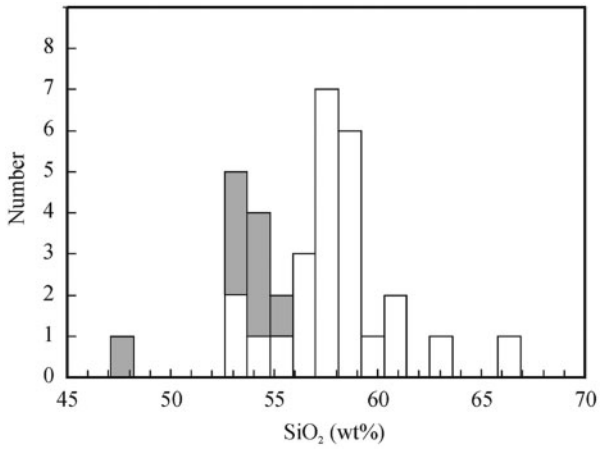

Fig. 3. Histogram for SiO_2 distribution in bulk-rock analyses. The distribution peaks at 57–59 wt %. The secondary peak at 53–55 wt % is caused by a priority in sampling and analysis of the olivine-bearing diorites (grey shading), which crop out only locally in the field.

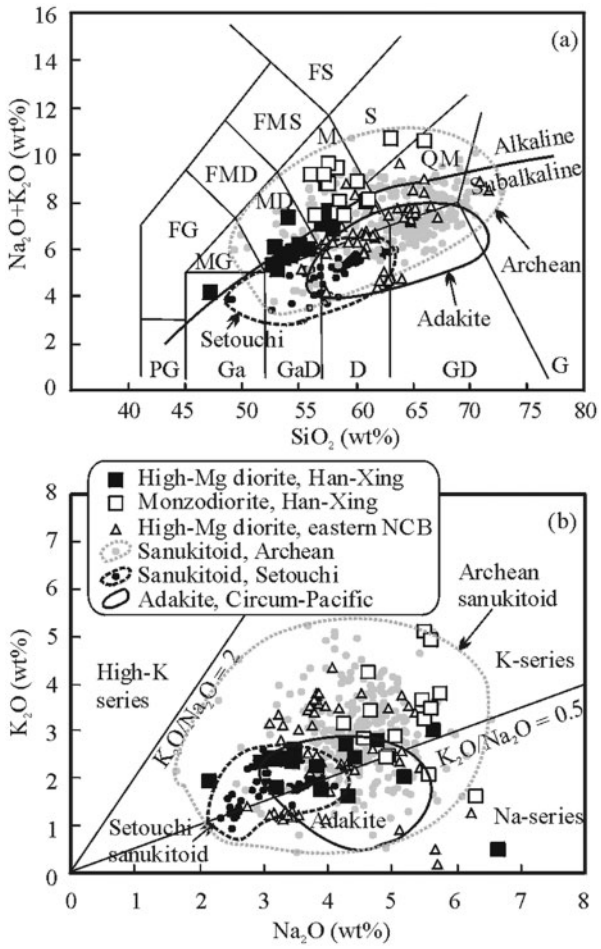

Fig. 4. (a) TAS (total alkali vs silica) diagram (after Middlemost, 1994); (b) K_2O vs Na_2O diagram. Mesozoic high-Mg adakites from the eastern part of China (Gao *et al.*, 2004; Xu *et al.*, 2006*a*, 2006*b*; Huang *et al.*, 2008), Cenozoic adakites from the circum-Pacific (Kay, 1978; Defant *et al.*, 1991*a*, 1991*b*; Morris, 1995; Yogodzinski *et al.*, 1995; Stern & Kilian, 1996; Danyushevsky *et al.*, 2008), Archean sanukitoids (Shirey & Hanson, 1984; Stern *et al.*, 1989; Stern & Hanson, 1991; Stevenson *et al.*, 1999; Smithies & Champion, 2000; Kamei *et al.*, 2004; Lobach-Zhuchenko *et al.*, 2005, 2008; Heilimo *et al.*, 2010) and Miocene sanukitoids from the Setouchi volcanic belt, Japan (Tatsumi & Ishizaka, 1982*a*, 1982*b*; Tatsumi *et al.*, 2006) are shown for comparison. D, diorite; FG, foid gabbro; FMD, foid monzodiorite; FMS, foid monzosyenite; FS, foid syenite; G, granite; Ga, gabbro; GaD, gabbroic diorite; GD, granodiorite; M, monzonite; MD, monzodiorite; MG, monzogabbro; PG, peridote-gabbro; QM, quartz monzonite; S, syenite.

was used with pulse rate of 5 Hz. Counting times were 20 s and 40 s for background and analysis, respectively. Pit depth was ~20 μm. NIST 612 glass was used as a standard for the raw counts, and ^{29}Si as the internal standard, with absolute SiO_2 values determined by EMP. Relative standard deviations from replicate LA-ICP-MS analyses of BCR-2G glass were better than 10% for most elements and <40% for phosphorus.

ANALYTICAL RESULTS

Major and trace elements of bulk-rock samples

Major and trace element compositions of the representative diorite–monzodiorite samples are given in Table 1. SiO_2 contents vary between 47 and 66 wt % (mostly between 53 and 61 wt %) and peak at 57–59 wt % in the probability distribution diagram (Fig. 3), highlighting the intermediate character of the rocks. These have moderate total alkali ($Na_2O + K_2O$) contents, and belong to the K-series according to their K_2O/Na_2O values (Fig. 4). The monzodiorites have high Al_2O_3 (16·4–17·7 wt %) contents, and low MgO (2·7–0·8 wt %), Cr (<36 ppm), Ni (mostly <20 ppm) and Mg# values (mostly between 43 and 36). The diorites have lower Al_2O_3 (11·6–16·8 wt %), and highly variable MgO (14·4–2·9 wt %), Cr (759–23 ppm), Ni (487–7 ppm) and Mg# values (75–48). The olivine-bearing diorites have the lowest SiO_2 and Al_2O_3 and highest MgO, Cr, Ni and Mg# values. With increasing MgO content, Cr, Ni and Co increase with a linear trend whereas SiO_2, Al_2O_3, Na_2O, K_2O and the alumina saturation index A/CNK [molar $Al_2O_3/(CaO + Na_2O + K_2O)$, mostly between 0·8 and 0·7] decrease (Fig. 5). TiO_2, FeO* (total Fe as ferrous iron) and CaO first increase and then remain constant for most samples, except that they are significantly elevated in one olivine-bearing diorite sample (CS33-1) that contains much more amphibole. Incompatible elements (e.g. Zr, Y and REE) decrease slightly with increasing MgO, whereas incompatible element ratios (e.g. Nb/La ~0·20, La/Yb ~20, Sr/Y ~40, and Dy/Yb ~2·0) are constant in all samples (Table 1), except sample CS33-1.

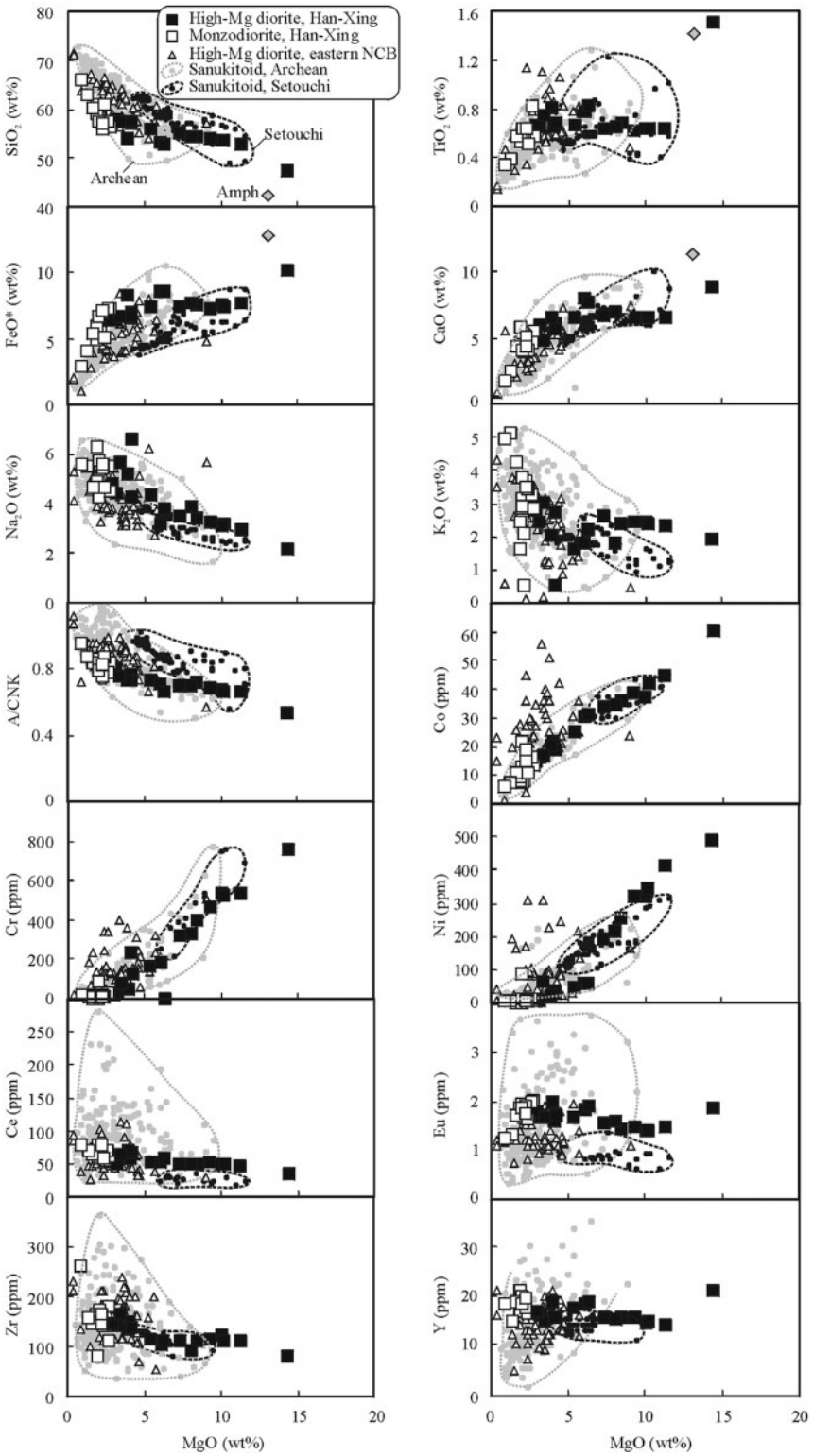

Fig. 5. Major and trace element variation diagrams for the Han-Xing diorite–monzodiorite samples. Samples with MgO >7 wt % are olivine-bearing. Grey diamond represents an average of 51 analyses of amphibole (Electronic Appendix 1) from the Han-Xing dioritic rocks. Data sources for sanukitoids are the same as in Fig. 4.

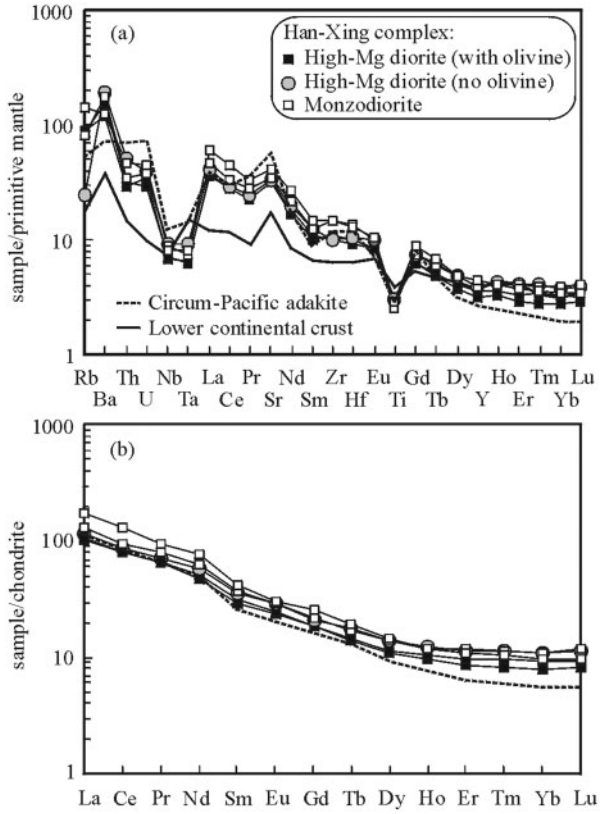

Fig. 6. (a) Primitive mantle-normalized incompatible element patterns; (b) chondrite-normalized rare earth element (REE) patterns. The close similarities between the Han-Xing diorite and monzodiorite and Cenozoic circum-Pacific adakites should be noted. The olivine-bearing high-Mg diorite of the Han-Xing complex is represented by samples CS17 and CS32, the high-Mg diorite without olivine is represented by sample FS2, and the monzodiorite is represented by samples CS38 and HK3. The circum-Pacific adakite is an average of 90 samples from Cenozoic circum-Pacific subduction zones (data source the same as in Fig. 4). The composition of the lower continental crust is from Rudnick & Gao (2003). Normalization constants are after Sun & McDonough (1989).

All diorite–monzodiorite samples have high Sr and Ba concentrations, in the range of 360–1030 and 230–1960 ppm (mostly >600 ppm), respectively (Fig. 6). Sr/Y ratios are high (mostly ~40) (Fig. 7). The REE are strongly fractionated, characterized by low heavy REE (HREE) abundances (Yb ≤2·0 ppm) and high $(La/Yb)_N$ ratios (10–18; N indicates chondrite normalization). However, fractionation between the HREE is mild, as is indicated by the Y/Yb ratios (mostly 9–10) and flat HREE patterns (Fig. 6b). In addition, the rocks are characterized by strong depletions of Nb, Ta and Ti and a positive Sr anomaly and display no Eu anomaly (Fig. 6). It is important to note that all samples with highly variable MgO have similar incompatible element characteristics, and resemble adakites and some sanukitoids in terms of incompatible elements (Table 1, Figs 6 and 7; see discussion for a detailed comparison).

Composition of rock-forming minerals

Electron microprobe data for rock-forming minerals of the high-Mg diorites and monzodiorites are presented in Electronic Appendix 1 (available for downloading at http://www.petrology.oxfordjournlas.org/). Major and trace element profiles across clinopyroxene and amphibole crystals are given in Electronic Appendices 2 and 3, respectively, and representative data are reported in Tables 2 and 3. Trace element compositions of olivine, plagioclase, orthopyroxene, biotite, K-feldspar, titanite and epidote are given in Electronic Appendix 3.

Olivine

All the investigated olivine crystals are normally zoned. The forsterite content $[Fo = 100 \times Mg/(Mg + Fe^T)]$ decreases gradually from core (89–93) to rim (73–84). Wide flat compositional plateaux of major and most trace elements are well preserved in the cores of some large olivine crystals. In these cores, NiO contents are high (0·34–0·48 wt %, i.e. 2670–3770 ppm Ni), Cr (300–360 ppm) and Co (~150 ppm) contents are elevated, whereas Ca (<450 ppm), Al (<250 ppm), P (~16 ppm), Sc (~2·3 ppm), Y (5·5 ppb) and Zr (<35 ppb, the limit of detection) contents are very low (Table 3, Electronic Appendix 3). Detailed major and trace element profiles across a normally zoned olivine were presented by Qian *et al.* (2010). The gradual enrichment of Fe and depletion of Mg from the core to the rim (Fig. 2d) has been interpreted as modification of the mantle xenocrysts by diffusion rather than crystallization of Fe-rich olivine from the diorite magma (Qian *et al.*, 2010).

Clinopyroxene

Clinopyroxenes (dominantly diopside) have variable compositions ($Wo_{43·0–49·6}En_{37·3–49·1}Fs_{6·2–22·2}$) and relatively low Al_2O_3 (<3·5 wt %), TiO_2 (<0·5 wt %) and Na_2O (<1·0 wt %) contents (Electronic Appendix 1). Normally and reversely zoned clinopyroxenes coexist in the high-Mg diorites. These zoned pyroxenes provide the most complete record of the chemical evolution and crystallization of the diorite magma and provide the basis for the core arguments of this study. Major and trace element variations across two normally zoned clinopyroxenes (CS32-1 and CS17-1) and three reversely zoned clinopyroxenes (CS45-1, CS22-1 and CS17-3) (Tables 2 and 3, Electronic Appendices 2 and 3) are described below.

CS32-1 (Fig. 8a) is a euhedral crystal (0·4 mm × 1·3 mm) developed from clinopyroxene overgrowths around an olivine core within high-Mg diorite CS32 (whole-rock Mg# ~69·2). From core to rim on profile A–B, Mg#, Ni and Cr decrease from ~85, 210 ppm and 2960 ppm to 75–76·5, 180–190 ppm and 2350–2670 ppm, respectively,

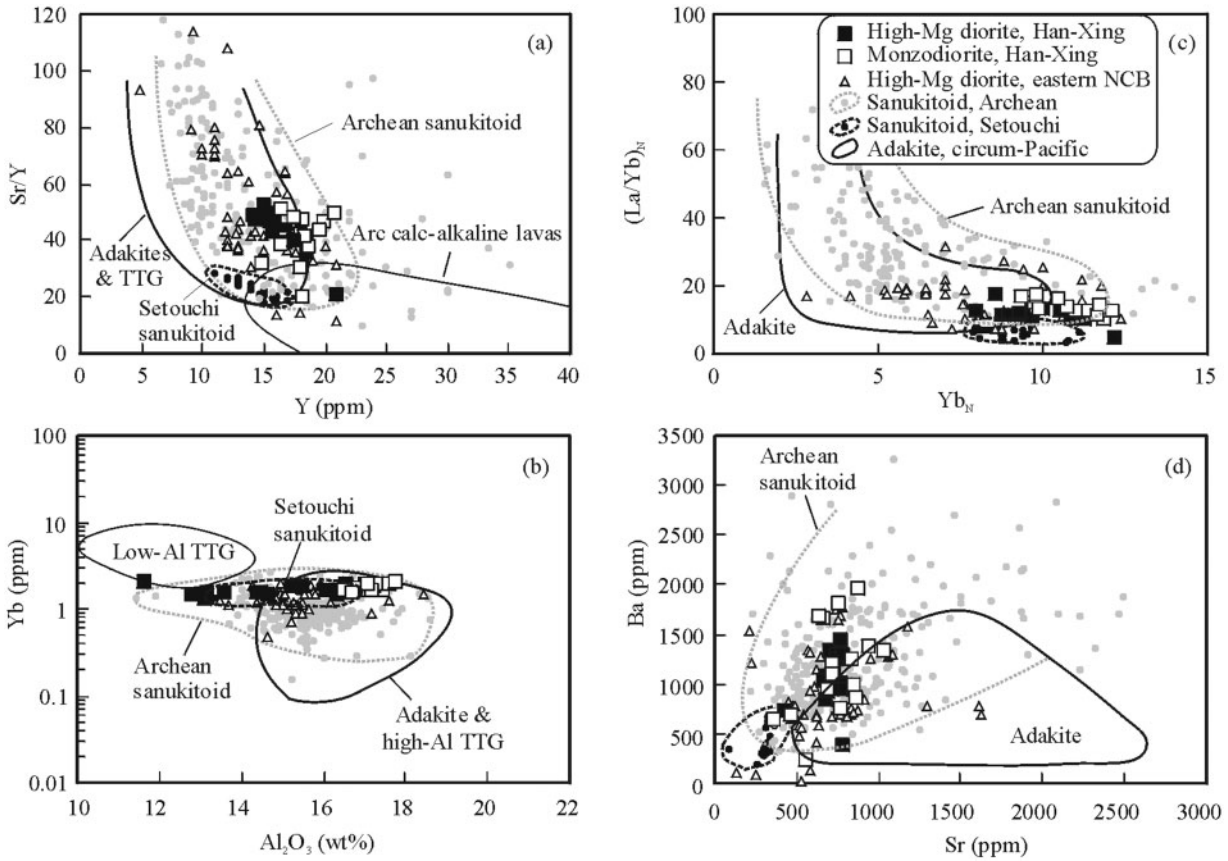

Fig. 7. (a) Sr/Y vs Y, (b) Yb vs Al_2O_3, (c) $(La/Yb)_N$ vs Yb_N, and (d) Ba vs Sr. Sanukitoids from Archean terranes and the Setouchi volcanic belt in Japan are shown for comparison. Data sources are the same as in Fig. 4. It should be noted that the Han-Xing diorite–monzodiorite samples fall within the field of Archean sanukitoid suites. The olivine-bearing diorites tend to have lower Al_2O_3 concentrations.

whereas incompatible elements (Sr, Zr, Hf, Ti, Y and REE) increase (Fig. 9). REE abundances increase by a factor of ~2. Incompatible element patterns are subparallel from core to rim (Fig. 9f and g). The incompatible trace element patterns are characterized by negative HFSE anomalies. There is no significant Eu anomaly in the REE patterns through the traverse. A negative Sr anomaly appears in the midsection and is even more pronounced at the rim of the clinopyroxene.

CS17-1 (Fig. 8b) is a euhedral crystal (0·5 mm × 0·8 mm) from an olivine-bearing high-Mg diorite CS17 (whole-rock Mg# ~72·8). From core to rim, Mg# and Ni values decrease from ~90 and 220 ppm to 77–78 and 190 ppm, respectively, whereas incompatible elements increase (Fig. 10). Cr decreases smoothly from 4960 to 3780 ppm across the profile A–B–C. CS17-1 is similar to CS32-1 in its incompatible element patterns, except that the REE contents of the former are ~2 times lower (Fig. 10f and g). A negative Eu anomaly is lacking in the core, but is clearly present at the rim (Eu/Eu* = 0·7–0·9). Sr displays an interesting behaviour. Although absolute Sr contents increase slightly from core to rim, the relative increase (in terms of percentages) is far smaller than the simultaneous enrichment of LREE. Thus, there is a pronounced positive Sr anomaly in the core and midsection whereas the rim is characterized by a negative Sr anomaly.

CS45-1 (Fig. 8c) is a subhedral crystal (2·2 mm × 2·5 mm) from the olivine-bearing high-Mg diorite CS45 (whole-rock Mg# ~71·9). The crystal contains a deformed low-Mg# core (1·2 mm × 1·5 mm) and an undeformed midsection and rim. Mg#, Ni and Cr increase abruptly from 76–78, 7–14 ppm and 2–12 ppm in the core to 86–88, 210 ppm and 2400–4700 ppm in the high-Mg# midsection, and then decrease to about 77–78, 120 ppm and 1700 ppm at the rim, respectively (Fig. 11). Incompatible elements display opposite trends to Mg#, Ni and Cr (Fig. 11d and e). For example, REE decrease by a factor of ~3 from core to high-Mg# midsection, and then increase by a factor of ~2 from high-Mg# midsection to the rim. From core to rim, incompatible element patterns are subparallel to those of CS32-1 and CS17-1 (Fig. 11f and g). The most interesting feature in the

Table 2: Representative major element analyses of normal- and reverse-zoned clinopyroxene and amphibole crystals

Mineral and spot	Position	SiO_2	TiO_2	Al_2O_3	Cr_2O_3	FeO	MnO	MgO	CaO	Na_2O	K_2O	Total	Mg#
Clinopyroxene													
CS32-1													
AB13	core	54·07	0·27	1·50	0·43	5·17	0·17	16·19	23·00	0·25	—	101·12	84·9
AB22	midsection	53·00	0·33	2·23	0·77	5·18	0·12	15·45	22·89	0·35	—	100·34	84·3
AB28	rim	51·91	0·49	2·65	0·27	7·55	0·24	13·61	22·65	0·48	—	99·89	76·4
CS17-1													
BC03	core	54·34	0·06	0·82	0·66	3·55	0·12	17·28	23·64	0·27	—	100·75	89·8
BC12	midsection	54·78	0·09	0·84	0·56	3·88	0·10	16·95	23·26	0·27	—	100·75	88·7
BC18	rim	53·92	0·13	1·05	b.d.l.	7·69	0·32	14·69	22·70	0·58	—	101·14	77·5
CS45-1													
AB74	core	51·99	0·41	2·41	b.d.l.	8·08	0·22	14·16	22·92	0·49	—	100·74	75·9
AB23	midsection	54·12	0·12	1·47	0·62	4·16	0·13	16·77	23·50	0·37	—	101·32	87·9
AB01	rim	52·73	0·35	2·03	0·07	8·11	0·39	14·90	21·84	0·49	—	100·91	76·8
CS22-1													
AB28	core	49·99	0·42	3·29	b.d.l.	8·28	0·27	13·38	22·61	0·36	—	98·59	74·4
AB43	midsection	52·54	0·14	1·13	0·50	4·25	0·24	15·35	24·31	0·21	—	98·67	86·7
AB51	rim	52·60	0·14	0·68	0·03	7·66	0·21	13·63	22·74	0·92	—	98·60	76·2
CS17-3													
AB23	core	49·77	0·42	3·20	b.d.l.	13·27	0·39	11·31	19·88	0·77	—	99·02	60·6
AB04	midsection	53·77	0·12	0·88	0·39	4·16	0·13	16·25	24·47	0·14	—	100·30	87·6
AB01	rim	52·05	0·26	1·95	0·07	7·83	0·27	15·29	21·09	0·48	—	99·30	77·9
Amphibole													
FS2-1													
AB23	core	40·20	1·46	13·97	—	16·33	0·32	9·97	11·33	2·32	1·00	96·90	60·8
AB06	midsection	43·71	1·00	11·73	—	10·56	0·21	15·22	10·98	2·41	1·04	96·79	89·7
AB01	rim	52·70	0·67	3·17	—	11·19	0·26	16·46	12·27	1·00	0·30	98·03	75·3

$Mg = Mg^{2+}/(Mg^{2+} + Fe^{T})$ for clinopyroxene; Mg# was calculated as $Mg^{2+}/(Mg^{2+} + Fe^{2+})$ for amphibole, assuming that total cations without Ca, Na and K add up to 13 with 23 total oxygen p.f.u.; —, not analyzed; b.d.l., below detection limit.

incompatible trace element patterns is the variation in Sr anomaly. The low-Mg# core has a significant negative Sr anomaly whereas the high-Mg# midsection has a distinct positive anomaly, which then disappears towards the outermost rim.

CS22-1 (Fig. 8d) is a subhedral crystal (~1·3 mm in diameter) within high-Mg diorite CS22, which contains no olivine. The Mg# increases from 74 in the core to 86 in the high-Mg# midsection, and then decreases rapidly to 70 at the inner part of the rim and increases slightly again to 76 at the outer part of the rim. Ni and Cr increase from about 40–60 and 120–280 ppm in the core to 130–140 and 3200–5000 ppm in the high-Mg# midsection, and then decrease rapidly to <20 and <25 ppm in the rim, respectively. Incompatible elements vary in trends opposite to Mg#, Ni and Cr (Fig. 12). Incompatible element patterns of the core and high-Mg# midsection are subparallel to those in the other clinopyroxenes (e.g. CS32-1) (Fig. 12f and g). Like sample CS45-1, the low-Mg# core of CS22-1 has a slight negative Sr anomaly, whereas the high-Mg# midsection has a small positive anomaly. A distinct trace element pattern that has not been observed in the other samples is present at the rim. REE increase by a factor of ~10 from the high-Mg# midsection to the rim and there are pronounced negative anomalies in Sr and Eu ($Eu/Eu^* = 0·6–0·8$).

CS17-3 (Fig. 8e) is a subhedral crystal (1·3 mm × 1·7 mm) from sample CS17, containing a low-Mg# core (1·0 mm × 1·3 mm) with a homogeneous composition. Mg#, Ni and Cr increase abruptly from about 60, 50 ppm and 60–190 ppm in the core to 87, 180 ppm and 3500–3750 ppm in the high-Mg# midsection, and then decrease gradually to 78–84, 160 ppm and 1240 ppm in the rim, respectively (Fig. 13). The Al_2O_3 content is 3·5 wt %

Table 3: Representative trace element analyses of olivine, clinopyroxene and amphibole crystals

Rock:	CS32				CS17			CS45		
Grain:	Ol CS32	Cpx CS32-1			Cpx CS17-1			Cpx CS45-1		
Position:	core	core	midsection	rim	core	midsection	rim	core	midsection	rim
Spot:	Ol	077	076	075	167	166	165	77	73	70
Li	2·84	9·53	8·01	6·37	13·7	14·9	14·8	8·59	9·55	8·39
Be	3·25	0·05	0·06	0·12	0·03	0·04	0·21	0·21	0·06	0·10
Al_2O_3	0·023	1·50	1·80	2·98	0·83	0·94	1·37	3·02	1·53	2·15
P	16·0	15·1	18·8	24·2	14·1	19·1	114	29·3	8·03	12·3
CaO	0·042	22·1	22·1	23·2	21·2	21·2	21·1	23·5	23·4	23·6
Sc	2·25	69·6	74·6	96·7	46·9	50·6	53·7	106	72·7	80·3
Ti	49·0	1360	1700	2750	710	840	1240	2580	1190	1760
V	—	127	146	209	67·0	79·8	101	228	162	189
Cr	320	2960	2550	2670	4110	3720	3780	4·00	2520	1740
Co	148	33·5	33·9	34·2	31·9	34·5	34·9	44·2	41·6	40·4
Ni	3560	214	203	181	216	207	190	10·7	106	118
Rb	—	b.d.l.	b.d.l.	b.d.l.	2·15	3·89	4·14	b.d.l.	b.d.l.	b.d.l.
Sr	—	62·6	65·4	79·2	61·8	60·8	62·1	95·3	74·4	87·6
Y	0·006	6·74	7·96	11·5	3·01	3·56	8·94	10·8	4·20	6·80
Zr	0·030	4·92	7·39	16·2	1·40	1·78	9·42	15·2	3·09	6·80
Nb	0·012	0·013	0·015	0·025	0·073	0·132	0·297	0·012	0·026	0·019
Cs	—	b.d.l.	0·009	b.d.l.	0·043	0·061	0·095	b.d.l.	b.d.l.	b.d.l.
Ba	—	b.d.l.	0·093	b.d.l.	12·4	32·5	85·9	0·57	0·07	b.d.l.
La	—	0·94	1·28	2·06	0·49	0·58	2·84	2·10	0·65	1·14
Ce	—	3·95	5·17	8·38	2·03	2·37	9·60	8·65	2·69	4·66
Pr	—	0·77	0·99	1·60	0·40	0·45	1·57	1·73	0·52	0·91
Nd	—	4·87	6·22	9·69	2·43	2·78	8·33	10·6	3·04	5·57
Sm	—	1·63	1·97	2·99	0·79	0·91	2·42	3·39	1·06	1·80
Eu	—	0·58	0·69	1·02	0·27	0·30	0·57	1·06	0·38	0·60
Gd	—	1·70	2·20	3·16	0·90	1·03	2·33	3·35	1·20	1·83
Tb	—	0·24	0·29	0·43	0·12	0·13	0·32	0·44	0·15	0·26
Dy	—	1·51	1·77	2·57	0·69	0·81	1·89	2·62	0·91	1·51
Ho	—	0·28	0·33	0·50	0·12	0·15	0·37	0·45	0·17	0·28
Er	—	0·72	0·89	1·25	0·32	0·37	0·94	1·15	0·41	0·76
Tm	—	0·09	0·11	0·16	0·04	0·04	0·13	0·14	0·06	0·09
Yb	—	0·54	0·67	0·96	0·23	0·28	0·79	0·84	0·34	0·54
Lu	—	0·07	0·09	0·13	0·03	0·04	0·12	0·11	0·05	0·08
Hf	—	0·25	0·37	0·83	0·07	0·09	0·43	0·78	0·16	0·35
Ta	—	b.d.l.	b.d.l.	b.d.l.	b.d.l.	b.d.l.	0·01	b.d.l.	b.d.l.	b.d.l.
Pb	—	0·05	0·06	0·07	0·17	0·13	0·44	0·61	4·44	0·11
Th	—	b.d.l.	b.d.l.	0·02	b.d.l.	b.d.l.	0·11	0·01	b.d.l.	0·01
U	—	b.d.l.	b.d.l.	b.d.l.	b.d.l.	b.d.l.	0·03	b.d.l.	b.d.l.	0·00

(Continued)

Table 3: Continued

Rock:	CS22			CS17			FS2		
Grain:	Cpx CS22-1			Cpx CS17-3			Amph FS2-1		
Position:	core	midsection	rim	core	midsection	rim	core	midsection	rim
Spot:	109	106	113	123	132	133	20	6	1
Li	13·5	8·35	10·9	11·62	9·36	16·3	11·6	2·79	9·39
Be	0·16	0·09	3·38	1·83	0·08	0·66	0·66	0·25	1·71
Al_2O_3	2·82	1·32	0·82	3·55	2·31	2·42	13·5	10·9	10·3
P	25·5	12·4	5·09	47·2	15·3	823	67	125	1162
CaO	22·6	22·6	22·2	19·7	22·8	21·2	10·3	10·4	11·2
Sc	83·5	66·5	104	121	71·5	76·8	38·2	46·7	57·3
Ti	1960	1060	772	2640	1570	1840	8300	6020	8370
V	200	116	178	286	177	178	306	382	257
Cr	127	3173	25·9	62·8	3460	1240	45·3	968	41·7
Co	42·0	34·4	30·4	56·8	37·0	37·9	44·5	60·6	48·2
Ni	43·9	131	20·0	50·5	153	157	27·2	209	56·5
Rb	0·080	0·144	0·146	0·048	0·037	9·14	3·95	3·58	2·69
Sr	94·7	74·9	23·0	8·62	76·5	60·5	235	214	212
Y	8·79	4·54	42·2	107	7·34	29·4	22·8	13·2	48·8
Zr	13·7	2·89	35·3	207	7·06	51·0	38·1	20·5	79·8
Nb	0·015	0·025	0·034	0·076	0·019	0·728	2·94	1·31	11·9
Cs	b.d.l.	0·012	b.d.l.	b.d.l.	0·011	1·04	0·08	b.d.l.	0·13
Ba	1·62	1·78	1·54	0·09	b.d.l.	4·54	269	166	259
La	1·43	0·76	7·71	13·0	1·19	13·0	4·95	3·68	21·3
Ce	6·14	3·15	31·0	56·5	5·01	40·0	20·9	15·0	69·9
Pr	1·17	0·63	5·63	9·01	0·95	6·10	3·59	2·56	11·3
Nd	7·39	4·06	31·6	45·5	5·97	30·7	20·5	14·0	58·8
Sm	2·44	1·31	9·34	13·9	1·85	7·72	5·63	3·77	13·7
Eu	0·83	0·48	1·74	2·45	0·64	1·67	2·21	1·28	3·36
Gd	2·43	1·49	9·71	17·3	2·01	7·11	5·66	3·90	12·9
Tb	0·32	0·18	1·38	2·89	0·27	0·97	0·75	0·49	1·71
Dy	2·06	1·09	8·79	19·8	1·59	6·00	4·84	2·88	9·67
Ho	0·39	0·19	1·66	4·15	0·31	1·12	0·94	0·52	1·81
Er	0·97	0·48	4·62	12·4	0·78	3·12	2·51	1·48	5·04
Tm	0·13	0·05	0·63	1·72	0·10	0·41	0·34	0·15	0·63
Yb	0·78	0·37	4·41	11·6	0·63	2·74	2·15	1·18	4·15
Lu	0·11	0·05	0·66	1·62	0·08	0·37	0·32	0·15	0·64
Hf	0·66	0·14	2·78	7·07	0·37	2·07	1·67	0·91	3·38
Ta	b.d.l.	b.d.l.	b.d.l.	0·03	b.d.l.	0·06	0·10	0·06	0·37
Pb	0·16	0·18	0·40	0·37	0·07	1·24	1·94	0·88	1·37
Th	0·01	0·01	0·07	0·69	b.d.l.	0·56	b.d.l.	0·11	0·81
U	b.d.l.	0·01	b.d.l.	0·09	b.d.l.	0·14	b.d.l.	b.d.l.	0·10

Data for the core of olivine are an average of nine analyses (see Electronic Appendix 3) with spot size of 70 μm, except that Y was analyzed with spot size of 247 μm. —, not analyzed; b.d.l., below detection limit. Al_2O_3 and CaO in weight per cent; other elements in ppm.

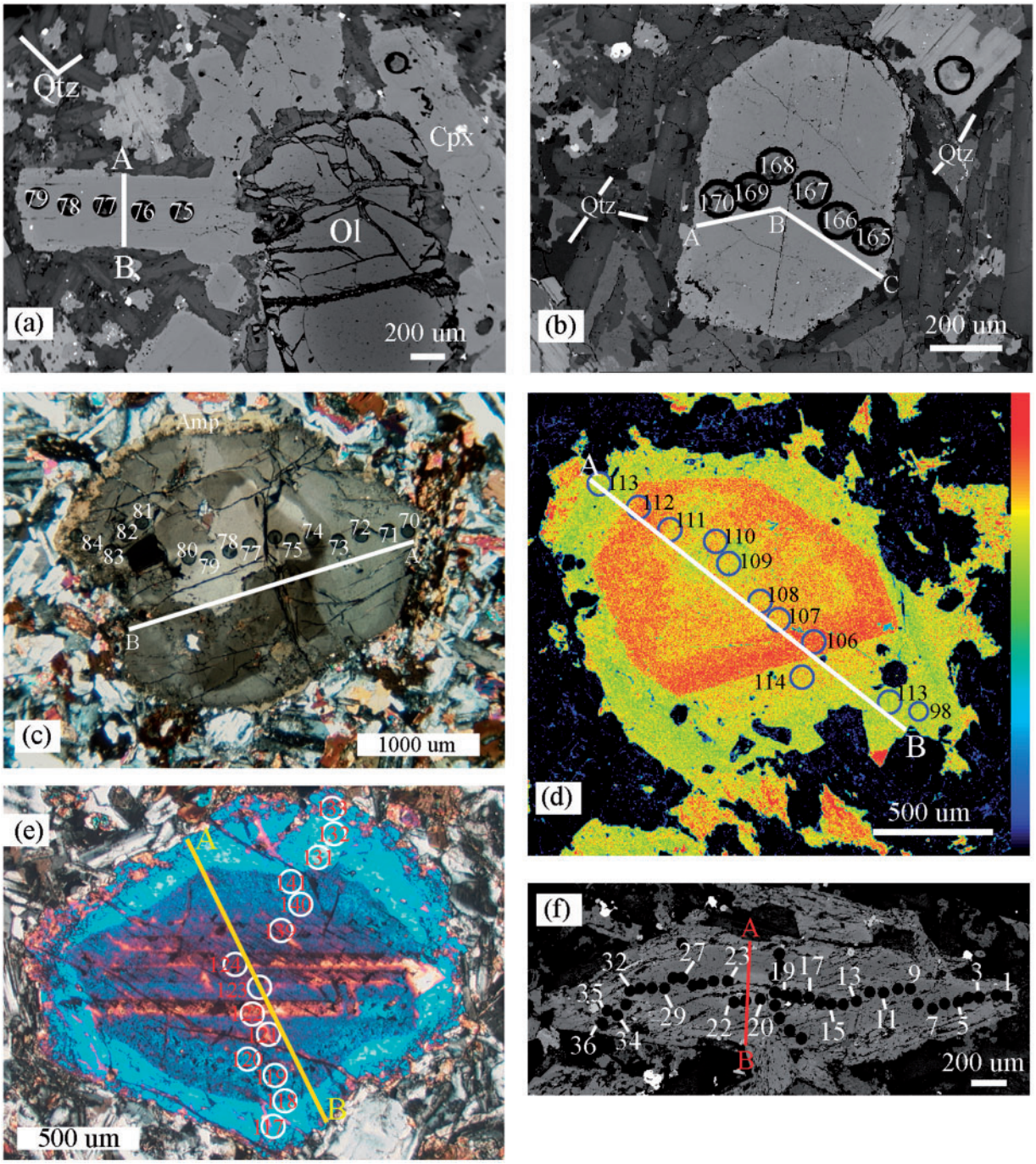

Fig. 8. (a) BSE image showing a normally zoned clinopyroxenes forming around an olivine xenocryst in a high-Mg diorite (sample CS32). Major and trace elements on profiles across one clinopyroxene (CS32-1) have been analyzed. It should be noted that quartz is ubiquitous in the matrix. (b) BSE image of a separate normally zoned clinopyroxene (CS17-1) from a high-Mg diorite (sample CS17). (c) Photomicrograph of a reversely zoned clinopyroxene (CS45-1) from a high-Mg diorite (sample CS45). The core is deformed. Amphibole microcrystals form around the clinopyroxene. (d) X-ray image of Mg for a reversely zoned clinopyroxene (CS22-1) from a diorite (sample CS22). (e) Photomicrograph of a reversely zoned clinopyroxene (CS17-3) from a high-Mg diorite (sample CS17). (f) BSE map of a reversely zoned amphibole (FS2-1) from a high-Mg diorite (sample FS2). EMP and LA-ICP-MS profiles are marked by straight lines and spots across the minerals, respectively.

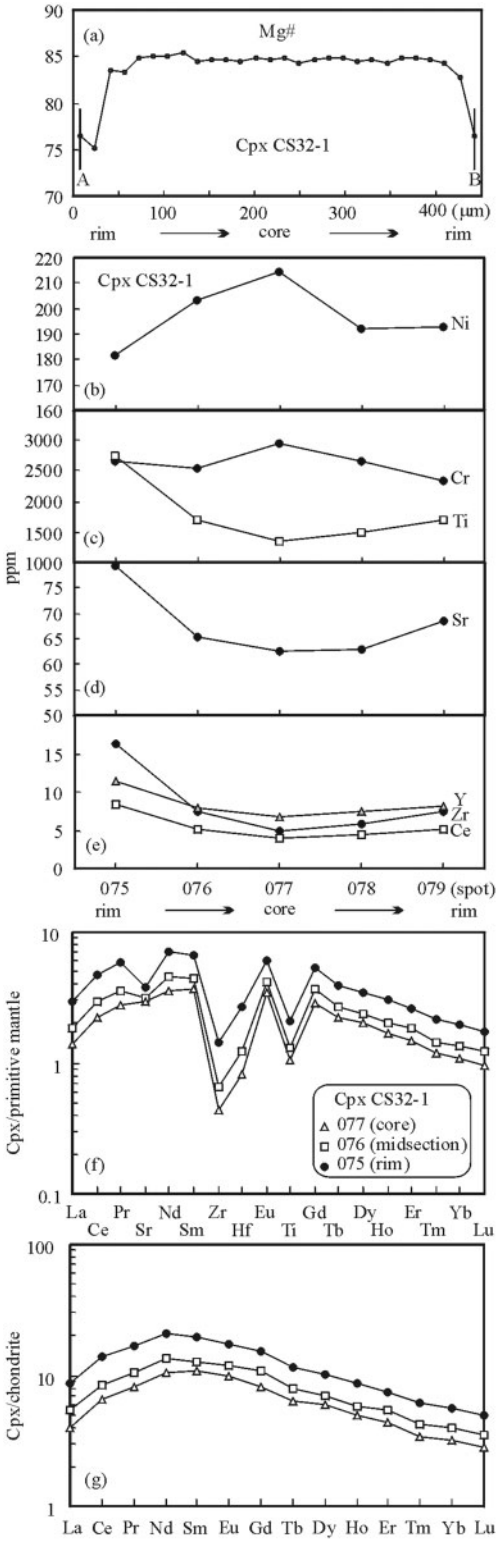

Fig. 9. (a) Mg# values on profile A–B across normally zoned clinopyroxene CS32-1. (b)–(e), variations of trace elements (Ni, Cr, Ti, Sr, Y, Zr and Ce) across CS32-1. Representative incompatible element contents in the core, midsection and rim are illustrated by the primitive mantle-normalized trace element patterns (f) and chondrite-normalized REE patterns (g). Normalization data are after Sun & McDonough (1989). It should be noted that the element patterns across the clinopyroxene are subparallel. Spot size of the LA-ICP-MS determination is 142 μm.

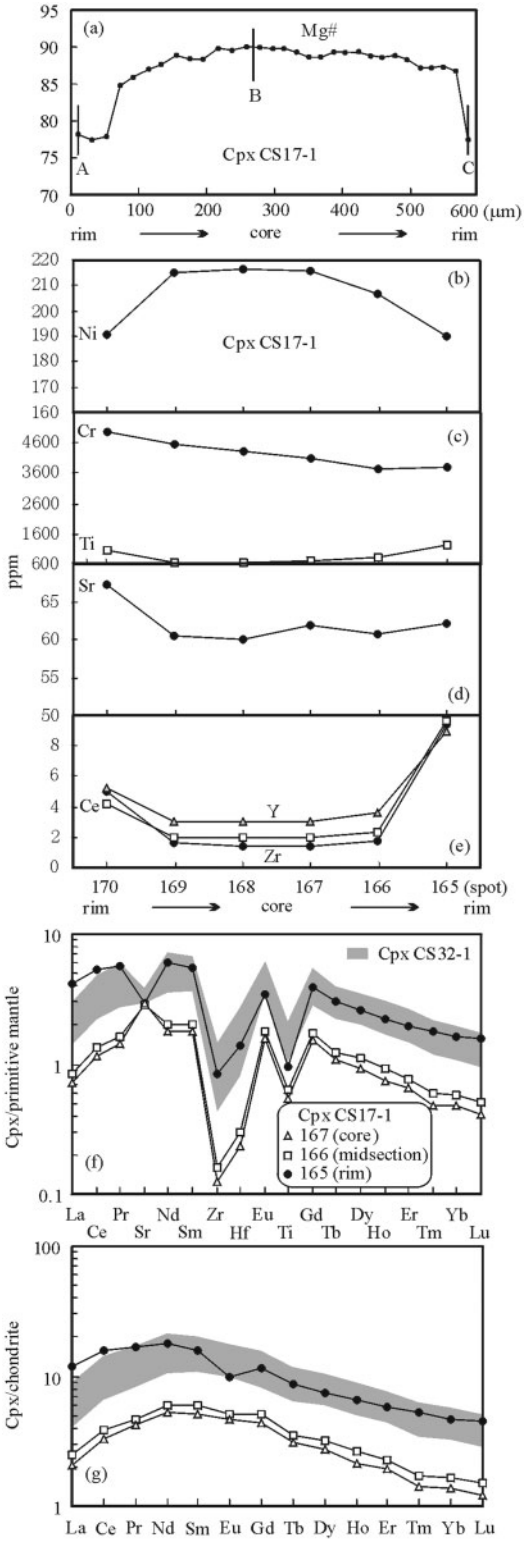

Fig. 10. (a) Mg# values on profile A–B–C across normally zoned clinopyroxene CS17-1. (b)–(e), variations of trace elements (Ni, Cr, Ti, Sr, Y, Zr and Ce) across CS17-1. Representative incompatible element contents in the core, midsection and rim are illustrated by primitive mantle-normalized trace element patterns (f) and chondrite-normalized REE patterns (g). Normalization data are after Sun & McDonough (1989). Spot size of the LA-ICP-MS analysis is 112 μm. Compositional field for clinopyroxene CS32-1 is shown for comparison.

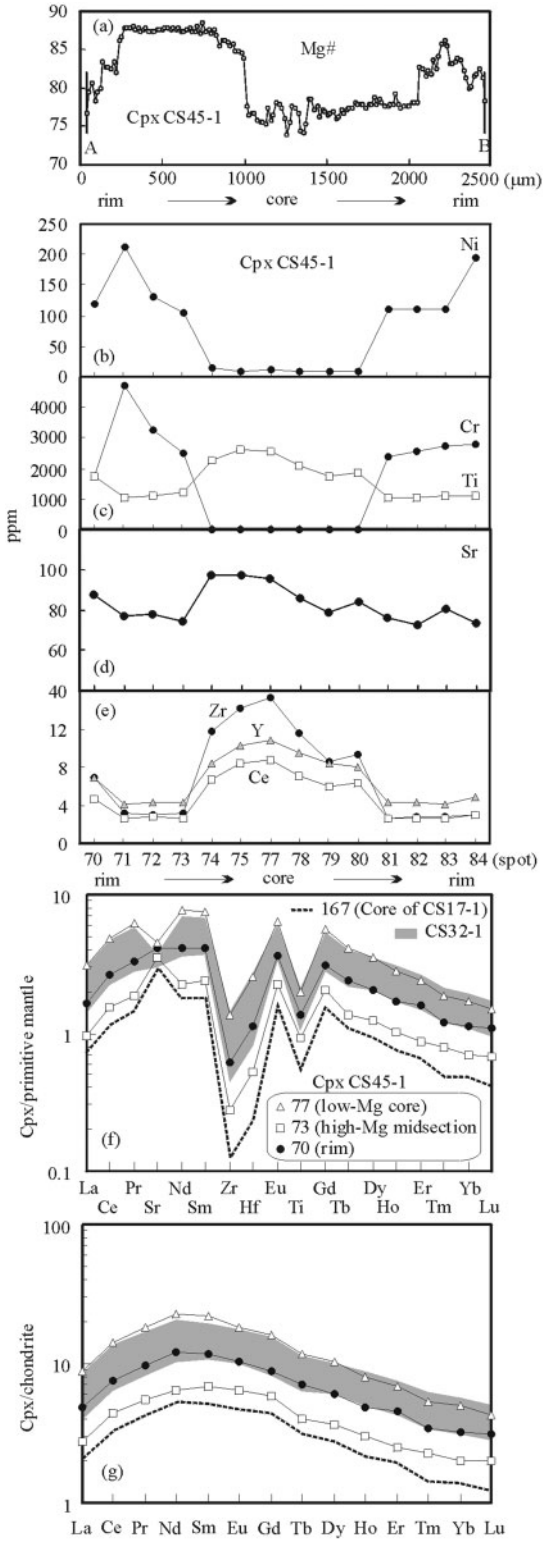

Fig. 11. (a) Mg# values along profile A–B across reversely zoned clinopyroxene CS45-1. (b)–(e), variations of trace elements (Ni, Cr, Ti, Sr, Y, Zr and Ce) across CS45-1. Representative incompatible abundances in the core, high-Mg# midsection and rim are illustrated in the primitive mantle-normalized trace element patterns (f) and chondrite-normalized REE patterns (g). Normalization data are after Sun & McDonough (1989). Spot size of LA-ICP-MS analysis is 112 μm. Compositions of clinopyroxenes CS32-1 and CS17-1 are shown for comparison. It should be noted that the core and high-Mg# midsection of CS45-1 resemble the rim of CS32-1 and the core of CS17-1, respectively, and all the distribution patterns are subparallel.

in the core and significantly lower (~1·5 wt %) in the high-Mg# midsection. Incompatible trace elements (Ti, Zr, Y and REE) vary with a trend opposite to that of Cr and Ni (Fig. 13c and e). The low-Mg# core of CS17-3 has REE abundances 6–18 times higher than those of the low-Mg# cores of CS45-1 and CS22-1. Surprisingly, the incompatible trace element pattern in the core of CS17-3 is most similar to that in the outermost part of the sample CS22-1, with strong negative anomalies in Sr and Eu (Fig. 13f and g). These anomalies are lacking in the high-Mg# midsection where the overall REE abundances are much lower. Indeed, the trace element patterns in the high-Mg# midsection and rim are similar to those of CS22-1.

Amphibole

The investigated amphiboles are mainly magnesiohastingsite and pargasite of the calcic-amphibole group of Leake *et al.* (1997), and are subordinately edenite, magnesiohornblende and actinolite. Usually, the main part of an amphibole crystal consists of magnesiohastingsite and pargasite, whereas the rim is composed of edenite, magnesiohornblende or actinolite. Separate interstitial microcrystals (<0·3 mm) are also edenite, magnesiohornblende or actinolite in composition. Major and trace elements profiles across a euhedral, reversely zoned amphibole (FS2-1) are described below.

Amphibole FS2-1 (Fig. 8f) is about 0·6 mm × 2·6 mm in size and contains a euhedral core (0·2 mm × 0·6 mm). Mg# increases from 60 in the core to 86–90 in the high-Mg# midsection, and then decreases to 67 in the inner part of the rim and increases again to 70–75 in the outer part of the rim (Fig. 14). Al_2O_3 decreases from ~14·4 wt % in the core to 11·3 wt % in the high-Mg# midsection, and then to 3·2–5·5 wt % in the rim. Ni and Cr increase from about 30–100 ppm and 45–330 ppm in the core to 200–220 ppm and 1000 ppm in the high-Mg# midsection, and then decrease to 40–60 ppm and 30–50 ppm in the rim, respectively (Fig. 14c and d). Nb, Ta, Zr, Hf, Ti, REE and Y decrease slightly from the core to the high-Mg# midsection, and then increase significantly towards the rim (REE increase by a factor of 4–6 from the high-Mg# midsection to the rim). The incompatible trace element patterns of the amphiboles are characterized by negative HFSE anomalies with respect to REE (Fig. 14f and g). The low-Mg# core has a small negative Sr anomaly whereas the high-Mg# midsection has a small positive

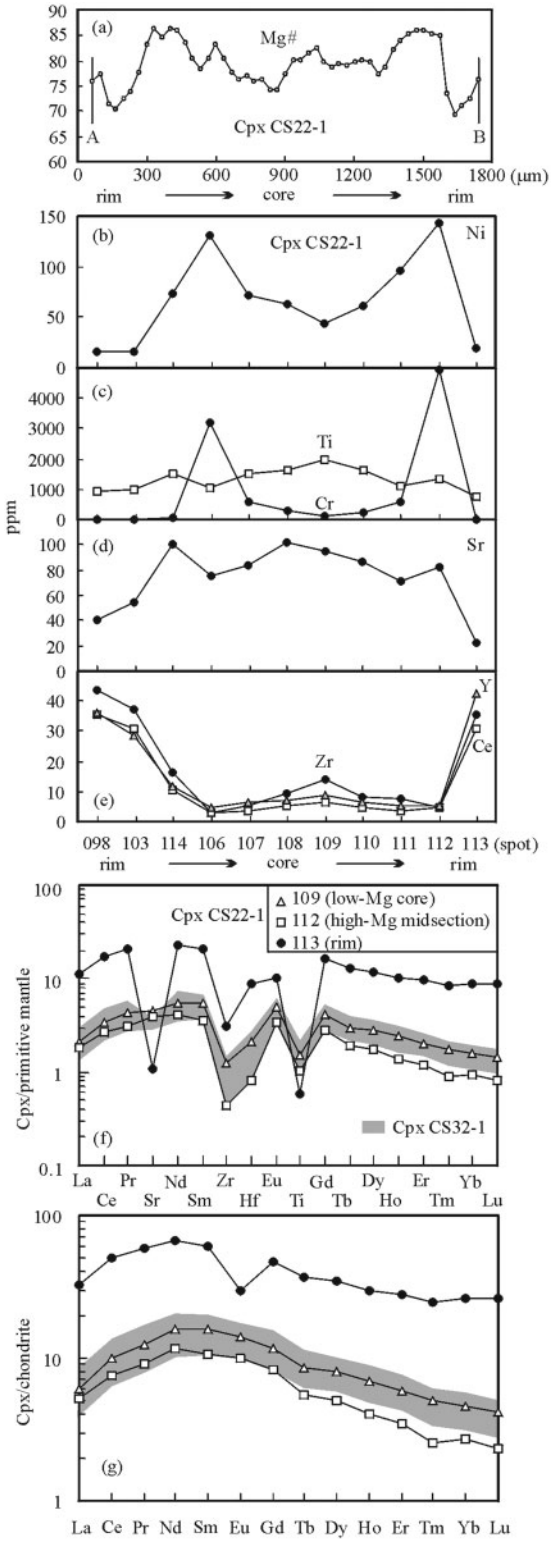

Fig. 12. (a) Mg# values along profile A–B across reversely zoned clinopyroxene CS22-1. (b)–(e), variations of trace elements (Ni, Cr, Ti, Sr, Y, Zr and Ce) across CS22-1. Representative incompatible element characteristics of the core, midsection and rim are illustrated by the primitive mantle-normalized trace element patterns (f) and chondrite-normalized REE patterns (g). Normalization data are after Sun & McDonough (1989). Spot size is 86 μm for spot 098 and 112 μm for the other spots. Compositional range of CS32-1 is shown for comparison. It should be noted that the trace element pattern of the low-Mg# core and high-Mg# midsection of CS22-1 resembles that of the rim and core of CS32-1, respectively.

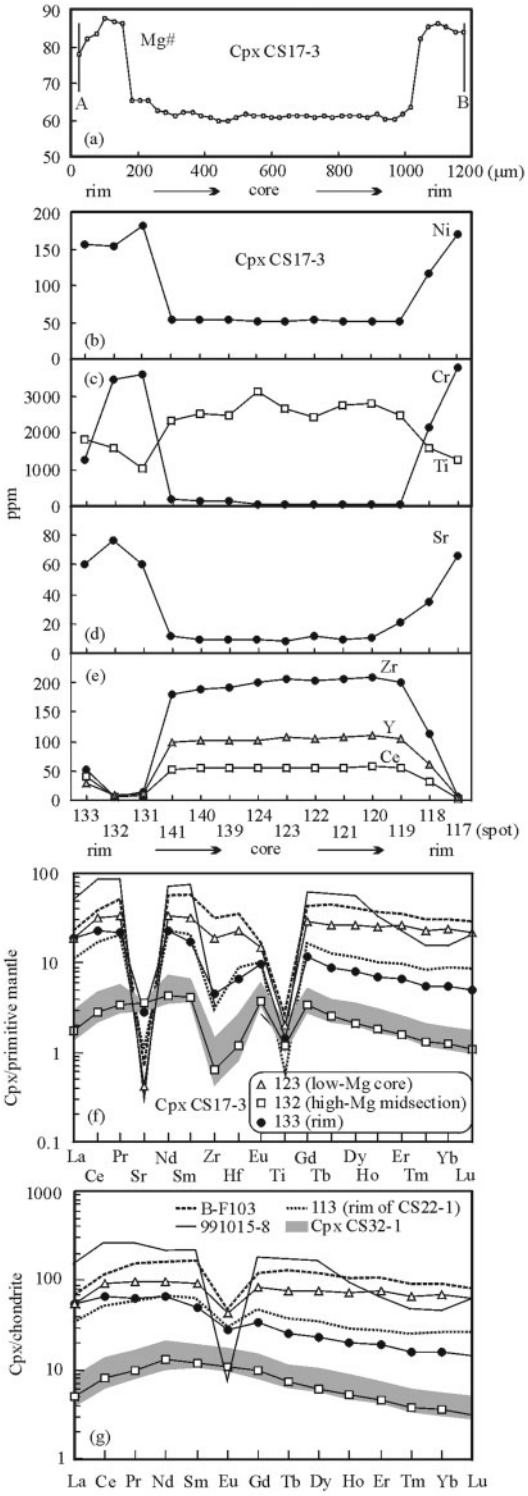

Fig. 13. (a) Mg# values along profile A–B across reversely zoned clinopyroxene CS17-3. (b)–(e), variations of trace elements (Ni, Cr, Ti, Sr, Y, Zr and Ce) across CS17-3. Representative incompatible element characteristics of the core, midsection and rim are illustrated by the primitive mantle-normalized trace element patterns (f) and chondrite-normalized REE patterns (g). Normalization data are after Sun & McDonough (1989). Spot size is 112 μm for LA-ICP-MS analysis. Compositions of CS32-1 and CS22-1, as well as a clinopyroxene (B-F103) from a lower-crustal Fe-gabbro (Hermann *et al.*, 2001) and a clinopyroxene (991015-8) from an adakitic quartz diorite vein in a mantle xenolith (Shimizu *et al.*, 2004) are shown for comparison. It should be noted that the trace element patterns of the high-Mg# midsection of CS17-3 are similar to that of the core of CS32-1.

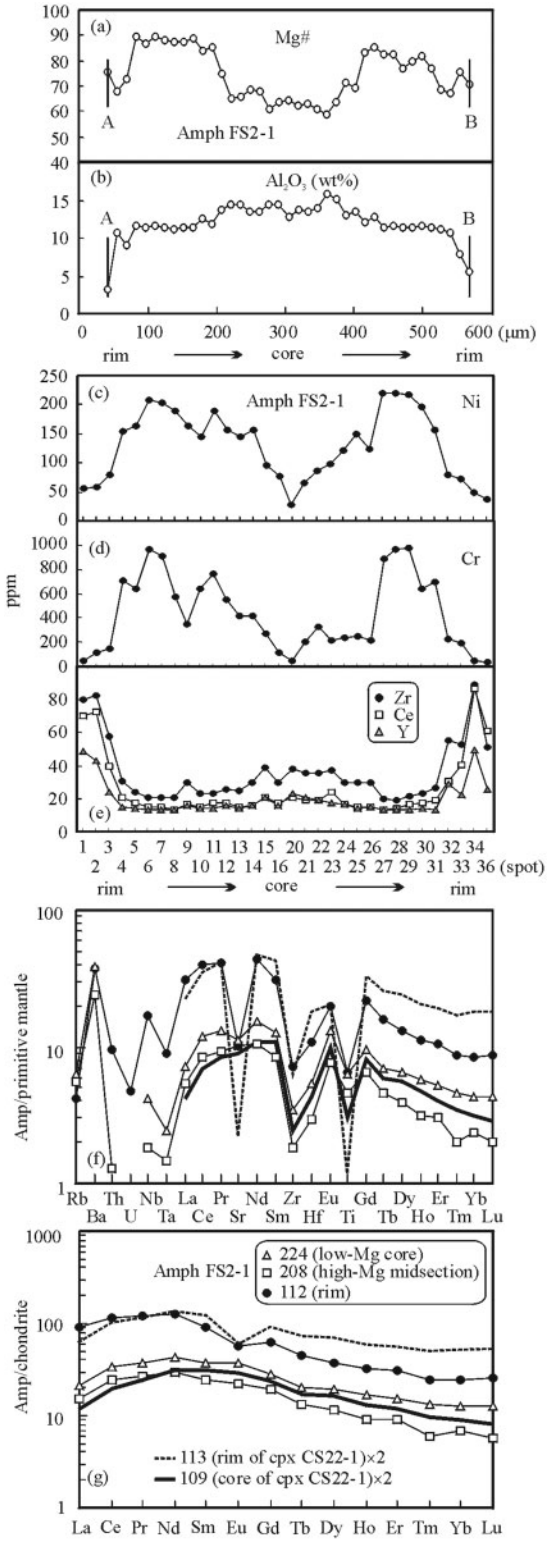

Fig. 14. (a) and (b) are Mg# and Al_2O_3 values along profile A–B across FS2-1, respectively. (c)–(e), variations of trace elements (Ni, Cr, Y, Zr and Ce) across FS2-1. Spots 221, 222 and 223 sampled plagioclase and K-feldspar inclusions and therefore are excluded. Representative incompatible element contents of the core, midsection and rim of FS2-1 are illustrated in the primitive mantle-normalized trace element patterns (f) and chondrite-normalized REE patterns (g). Normalization data are after Sun & McDonough (1989). Spot size is 70 μm for LA-ICP-MS analysis. It should be noted that the REE concentrations of the core and rim of FS2-1 are about two to five times that of the core and rim of clinopyroxene CS22-1, respectively.

anomaly. The rim is characterized by a very strong negative Sr anomaly. There is no negative Eu anomaly in the core, and a slight anomaly at the rim (Eu/Eu* = 0·8–0·9). It is notable that core and rim of FS2-1 have incompatible element abundances about 2 to 5 times that of clinopyroxene CS22-1, respectively.

Plagioclase, orthopyroxene, biotite, K-feldspar, titanite and epidote

Plagioclase crystals have well-developed normal zoning, with $An_{58–39}$ in the core and $An_{37–7·6}$ in the rim. Rarely, plagioclase phenocrysts with high-An cores (up to 74) and low-An rims (~9·7) occur. Sr is higher in the cores (3100–3300 ppm) than in the rims (2700–800 ppm). REE are fractionated and the REE contents are similar for the core and rim. A positive Eu anomaly is present throughout plagioclase.

Orthopyroxene overgrowths around olivine have Mg# values of 75–84 and low Al_2O_3 (0·5–2·0 wt %), CaO (0·3–1·5 wt %), TiO_2 (<0·5 wt %) and Cr_2O_3 (mostly <0·3 wt %) contents. REE patterns are U-shaped, with a trough and negative anomaly at Eu (Eu/Eu* = 0·4–0·95). Normalized contents of La–Sm vary by a factor of 2–6, whereas those of Gd–Lu are similar for all spots.

Biotite has MgO and FeO contents of 15·4–22·6 wt % and 3·7–5·7 wt %, respectively. Rb (240–340 ppm) and Ba (2400–9700 ppm) contents are high, whereas REE contents are very low (e.g. La, Ce <1·7 ppm). Nb, Ta, Sr and Ti show marked positive anomalies in incompatible element distributions.

K-feldspar has compositions in the range $Ab_{2·3–39·1}An_{0·0–2·9}Or_{59·1–97·7}$. Rb, Sr and Ba contents are about 89–130 ppm, 2000–5700 ppm and 1300–5600 ppm, respectively. REE contents are low (e.g. La = 2·6–3·6 ppm) and fractionated. Sr and Eu show strong positive anomalies.

Titanite has high Th (80–700 ppm), U (16–180 ppm), Nb (140–1860 ppm), Ta (6·3–124 ppm), Zr (440–6400 ppm), and REE (La = 800–6750 ppm, Yb = 24–96 ppm) contents. Negative anomalies are small for Nb, Ta, Zr and Hf, but strong for Sr in normalized incompatible element patterns. LREE are fractionated [$(La/Sm)_N = 3·4–21$], whereas HREE patterns are relatively flat [$(Gd/Yb)_N = 1·1–2·3$]. Eu anomalies are lacking.

Epidote has low and fractionated REE (La = 6–8 ppm), as well as strong positive Sr and Eu anomalies. Sr contents are as high as 9100–20800 ppm. Ba and Y contents are 25–56 ppm and ~0·2 ppm, respectively.

Composition of mineral inclusions

Compositions of plagioclase, K-feldspar and biotite inclusions in the low-Mg# cores of reversely zoned clinopyroxene and amphibole crystals are given in Electronic Appendix 4. Plagioclase inclusions (An = 20–42) from the core of reversely zoned clinopyroxene are andesine in composition. A plagioclase inclusion from the core of amphibole FS2-1 has An ~55. Compositions of K-feldspar inclusions from the cores of reversely zoned clinopyroxene and amphibole have compositions of $Ab_{2·5–20}An_{0·4–1·2}Or_{79–97}$. Biotite inclusions in the cores of reversely zoned clinopyroxene have low MgO (14·6–14·8 wt%) and Mg# (~65) values.

Stages of mineral crystallization

The detailed trace element profiles in clinopyroxene and amphibole can be used to infer three principal stages of mineral crystallization. The first stage is documented in the lower Mg# cores of reversely zoned crystals. The cores of CS22-1 and CS45-1 have similar REE contents and patterns, and have negative Sr anomalies and Mg# values of ~75. This suggests that they represent cumulus crystals formed from a melt similar to the monzodiorites. The amphibole cores in FS-1 formed at a similar stage and display high Ba, negative HFSE and Sr anomalies, and high LREE contents, also indicating that they were in equilibrium with a monzodioritic melt characterized by significant LREE enrichment. The negative Sr anomaly in the cores indicates co-precipitation of cumulus plagioclase. This is supported by inclusions of plagioclase in the cores of these amphiboles and clinopyroxenes. The core of CS17-3 is fundamentally different, with much higher REE contents, lower Mg# and much stronger negative anomalies in Sr and Eu than the cores of the other two clinopyroxenes. Detailed study of trace element distributions in deeply crystallized mafic rocks has shown that these features are typical of pyroxenes that are not cumulus crystals but form from 'frozen melts' during the complete crystallization of a melt pod (Hermann *et al.*, 2001). Indeed, the incompatible element patterns of the core of CS17-3 are analogous to those of clinopyroxenes from 'frozen melts' such as a Fe-gabbro (sample B-F 103) in the Braccia gabbro complex, Eastern Central Alps (Hermann *et al.*, 2001) and an adakitic quartz-diorite vein (sample 991015-8) within mantle xenoliths in a Tallante (Spain) alkali basalt (Shimizu *et al.*, 2004). It is worth noting that the lower Mg# cores of clinopyroxene and amphibole have the highest Al_2O_3 contents.

The second stage is documented by a sudden increase in Mg#, Cr and Ni in all reversely zoned clinopyroxenes and equally high Mg#, Cr and Ni values in the cores of normally zoned crystals in samples CS32-1 and CS17-1. Trace element abundances in general are slightly lower but similar to those of the low-Mg# cores of the reversely zoned clinopyroxenes. The same trends are also observed in reversely zoned amphibole. The most interesting feature is the change from a negative to an absent or positive Sr anomaly. This suggests that dissolution of plagioclase occurred at the transition from lower Mg# cores to high-Mg# midsection domains of clinopyroxene and amphibole.

The third stage documents crystallization of the outer rims of clinopyroxenes and amphiboles. This stage is characterized by a gradual increase in incompatible trace elements. There is a decrease in Sr with respect to REE, which leads first to the disappearance of the positive Sr anomaly and then to the formation of a pronounced negative Sr anomaly. This indicates that plagioclase was again crystallizing at the same time. Some rims (cpx CS22-1, amph FS2-1) show extreme enrichment in all REE and a very strong negative Sr and a pronounced negative Eu anomaly similar to the core of CS17-3, and by analogy this is interpreted to represent clinopyroxene and amphibole crystallization during the solidification of the residual melt.

Pressure of crystallization

The presence of plagioclase inclusions in the cores of reversely zoned clinopyroxene and amphibole crystals provides the foremost evidence that the first and second stages of crystallization must occur at depths shallower than that required for the stability of eclogite. Pressures of the first and second stage of crystallization were further estimated from the compositional zoning of amphibole FS2-1, using the Al-in-hornblende geobarometer (Schmidt, 1992). This barometer requires that a buffering mineral assemblage is present consisting of quartz, K-feldspar, plagioclase, amphibole, biotite, titanite and magnetite. K-feldspar, plagioclase, biotite, titanite and magnetite have been observed in the cores of reversely zoned clinopyroxene and amphibole crystals whereas quartz and titanite are present in the matrix of the samples. Thus the requisite mineral assemblage for applying the geobarometer to the amphibole is satisfied. The low-Mg# core of FS2-1 has a higher Al content and yielded an average pressure of about 9 kbar, whereas the high-Mg# midsection yielded average pressures of about 6–7 kbar (Fig. 15). It is important to note that the calibration of Schmidt (1992) was obtained at 655–700°C, which is significantly lower than the temperature of amphibole formation. The total Al (p.f.u.) that is used to calculate pressure also increases with increasing temperature (Blundy & Holland, 1990). A formation temperature of 900°C (with a likely error of ±50°C) can be estimated using the two-pyroxene geothermometer of Brey & Köhler (1990) for coexisting orthopyroxene and clinopyroxene microcrysts around the olivine xenocrysts (P is assumed to be 6 kbar) and using the amphibole–plagioclase geothermometer of Blundy & Holland (1990) for the amphibole midsection and the core of idiomorphic

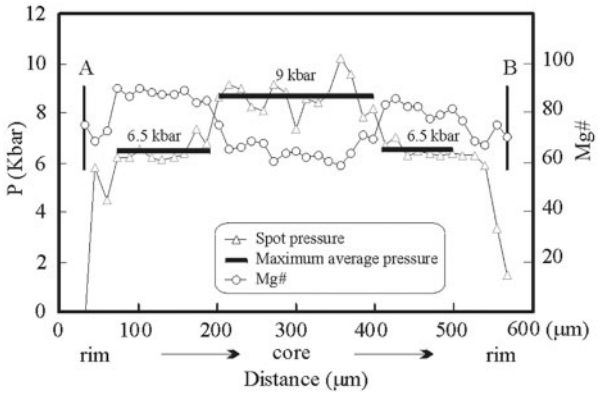

Fig. 15. Maximum average pressure (in kbar) for the low-Mg core and high-Mg midsection of the reversely zoned amphibole FS2-1, estimated using the Al-in-hornblende geobarometer of Schmidt (1992) for profile A–B. Pressure and Mg# value for each electron microprobe spot on the profile are also shown.

plagioclase with $An_{42–52}$. For these higher temperatures of amphibole crystallization the pressure will be overestimated (Anderson & Smith, 1995). It is difficult to quantify a pressure correction and thus we conclude that the pressures for the formation of the high-Mg# midsection (6–7 kbar) and low-Mg# core (9 kbar) represent maximum values.

The pressure for the outer part of the rim of FS2-1 was estimated to be less than 2 kbar (Electronic Appendix 5). A similar pressure range was obtained for amphibole rims around clinopyroxene (e.g. CS45-1) and for subhedral amphibole microcrystals interstitial to plagioclase.

DISCUSSION

Petrogenesis of high-Mg diorite

Source of olivine

The first question that needs to be addressed is whether the olivine crystals in the diorites represent phenocrysts or xenocrysts. The overall high SiO_2 content of the bulk-rocks is in conflict with a magmatic origin of the olivine. The normal zoning of olivine with $Fo_{89–93}$ in the core and the continous enrichment in iron towards the rim might be at first sight taken as evidence for crystallization of olivine in an evolving magma. However, Ca (<400 ppm) and Al (<250 ppm) contents are very low, indicating a mantle origin (Thompson & Gibson, 2000; De Hoog *et al.*, 2010), and are inconsistent with a magmatic origin, based on experimentally determined olivine–melt partition coefficients for CaO (Jurewicz & Watson, 1988; Libourel, 1999). Moreover, Y contents increase gradually from about 6 ppb in the core to 200–350 ppb in the rim of olivine (Qian *et al.*, 2010); that is, by a factor of 30–60. This would imply that during olivine crystallization the Y content of the melt would have changed by a factor of 30–60, which is impossible. Alternatively, the gradual decrease in Fo and Ni content and increase of Mn, Ca, Sc and Y from core to rim can be perfectly explained by diffusion-related modification of xenocrystic mantle olivine (Qian *et al.*, 2010). The major element zoning of olivine has been successully reproduced by diffusion modelling with a residence time of 10^2–10^3 years in the dioritic magma (Qian *et al.*, 2010). Therefore, the textures and composition of the olivine demonstrate that the olivine crystals from the Han-Xing high-Mg diorites are relict xenocrysts.

Large olivines retain their original compositions in the core with wide plateaux in Mg–Fe, Mn, Ca, Sc and Y abundances (Qian *et al.*, 2010), providing evidence for their provenance. The cores of the olivines have high Fo (89–93) and Ni (2670–3770 ppm), moderate Cr (300–350 ppm), and low incompatible elements P (~16 ppm), Y (~5·5 ppb), Sc (~2·3 ppm), and Zr (~30 ppb) (Table 3, Electronic Appendix 3). The incompatible element abundances are within the compositional range of mantle olivines reported by De Hoog *et al.* (2010) but lower than those of mantle olivines from lherzolites reported by Witt-Eickschen & O'Neill (2005) (P 20–160 ppm, Y 12–76 ppb, Sc 2·3–4·8 ppm, Zr 11–117 ppb). The concentrations of incompatible trace elements and the elevated Cr contents indicate a provenance from a highly depleted peridotite, most probably a dunite.

Harzburgite and dunite xenoliths have been found in the Fushan pluton of the Han-Xing complex (Huang & Xue, 1990*b*; Xu & Lin, 1991; Xu *et al.*, 2009, 2010) and in several other Mesozoic (~130 Ma) diorite plutons near the Tan-Lu fault in the eastern NCB (Xu *et al.*, 2003*a*, 2003*b*, 2008; Chen & Zhou, 2005). Late Archean to Paleoproterozoic Re-depletion model ages have been obtained for spinel harzburgite and lherzolite xenoliths from the Fushan pluton (see Xu *et al.*, 2010). Peridotite xenoliths from high-Mg diorites from the eastern NCB yield Archean Re-depletion model ages of 2·6–2·7 Ga (Gao *et al.*, 2006). These peridotite xenoliths are interpreted to represent old subcontinental lithospheric mantle beneath the NCB (Gao *et al.*, 2006, 2008; Xu *et al.*, 2010).

Original magma of high-Mg diorite

The olivine-bearing diorites are the most mafic rocks in the Han-Xing complex. They have been referred to as gabbroic rocks (Huang & Xue, 1990*a*; Xu & Gao, 1990; Song & Feng, 1999; Chen *et al.*, 2004, 2008; Wang *et al.*, 2006), and proposed to be partial melts of an EM1-type subcontinental lithospheric mantle (Chen *et al.*, 2004, 2008; Wang *et al.*, 2006). Our petrographic observations (Fig. 2), however, strongly suggest a felsic original magma for the high-Mg diorites: (1) the most mafic olivine-bearing high-Mg diorites contain widespread interstitial quartz, and the olivines are xenocrysts and therefore these rocks cannot represent a mantle melt; (2) reversely zoned clinopyroxene and amphibole crystals have low-Mg# cores

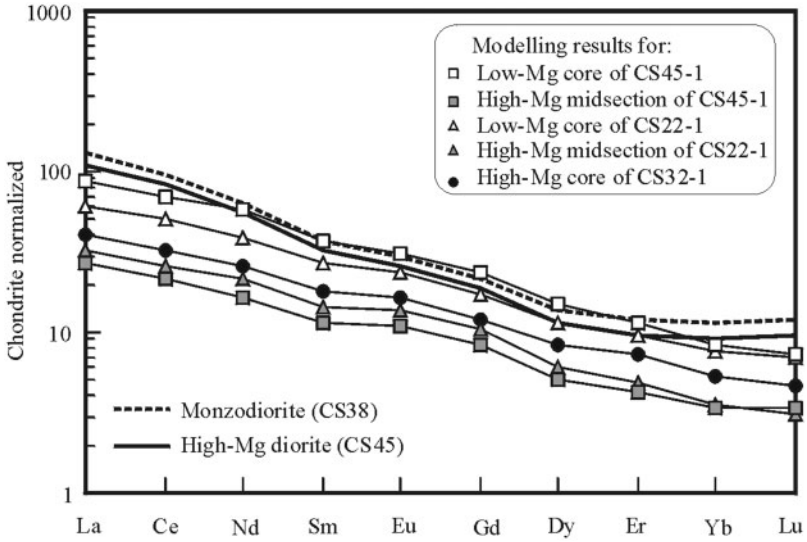

Fig. 16. REE-modelling results for clinopyroxenes CS32-1, CS45-1 and CS22-1, which represent cumulus phases. The mineral–melt partitioning is $K_d = C^i_{mineral}/C^i_{melt}$, where K_d is the Nernst partition coefficient between clinopyroxene and melt, and C^i is the concentration of a trace element *i*. K_d values are from Martin (1987): La, 0·1; Ce, 0·2; Nd, 0·4; Sm, 0·6; Eu, 0·6; Gd, 0·7; Dy, 0·7; Er, 0·6; Yb, 0·6; Lu, 0·6. Spot analyses for modelling are given in Table 3. Monzodiorite and high-Mg diorite are represented by sample CS38 and CS45, respectively. Normalization data are after Sun & McDonough (1989).

and low Ti contents, which are incompatible with either a primitive or evolved mafic original melt; (3) mineral inclusions of andesine, K-feldspar and low-Mg biotite occur in the cores of reversely zoned clinopyroxenes.

The geochemical data indicate that the monzodiorites most probably represent the pristine magma of the high-Mg diorites. Indeed, the trace element patterns of all diorites and monzodiorites are remarkably similar (Fig. 6), pointing to a common original magma of monzodiorite composition for the whole sample suite. The textural, major and trace element characteristics of some of the analyzed crystals provide evidence that they formed as cumulus phases. Hence, the composition of the coexisting liquid can be estimated using appropriate mineral–melt partition coefficients. The Mg# value of the magma present in the first stage of crystallization was estimated to be 41–34 based on the Mg# of the cores of reversely zoned clinopyroxene (CS45-1 and CS22-1) and amphibole (FS2-1) crystals, using clinopyroxene–liquid and amphibole–liquid partition coefficients [$K_d = (Fe/Mg)_{mineral}/(Fe/Mg)_{liquid}$] of 0·23 and 0·35 (Grove & Bryan, 1983; Sisson & Grove, 1993), respectively. This value is similar to the Mg# of the monzodiorites (41–36). The REE composition of the melts in equilibrium with the low-Mg# cores of reversely zoned clinopyroxenes CS45-1 and CS22-1 can be calculated using the partition coefficients of Martin (1987). The resulting melts show close similarities to the REE patterns of the monzodiorites (Fig. 16). The calculated REE patterns of the melts in equilibrium with the cores of normally zoned clinopyroxenes and the high-Mg# midsections of reversely zoned clinopyroxenes are subparallel. However, they are ~2 times lower than the bulk-rock REE of the high-Mg diorites (Fig. 16). This can be explained by an enhanced dilution of the immediately adjacent magma during olivine assimilation (see below).

Assimilation of mantle peridotite by felsic magma

Resorption of mantle dunite and olivine xenocrysts by the quartz-bearing dioritic matrix (Fig. 2) provides important petrological evidence for the formation of high-Mg diorites through assimilation of mantle peridotite by felsic magma. The pyroxene–spinel symplectite and high-Mg zonings of clinopyroxene and amphibole crystals may be produced by the following reactions:

$$\text{Olivine} + SiO_2 + O_2 = \text{Orthopyroxene} + \text{Spinel} \quad (1)$$

$$\text{Olivine} + \text{Plagioclase} + \text{Melt}_1 = \text{Clinopyroxene} + \text{Amphibole} + \text{Melt}_2 \quad (2)$$

The production of orthopyroxene, clinopyroxene and amphibole at the expense of olivine during hybridization of adakitic melts by reaction with peridotite has been experimentally documented by Rapp *et al.* (1999). Although the resultant orthopyroxene microcrystals are minor in quantity and largely confined around olivine, they may play an important role in the overall assimilation process as an armor preventing further reaction between olivine and melt. An olivine consuming reaction has also been recorded geochemically by an abrupt increase of Mg#, Cr

and Ni in the reversely zoned clinopyroxene and amphibole crystals.

The compositions of the high-Mg diorites can be well approximated by mixing monzodiorite and mantle dunite in varying proportions. The differences between the calculated and actual values are within 10% of each other for most of the major elements and Ni, Y, Sr, Zr, Nb, Th and REE except Lu (Electronic Appendix 6). The regular increase of Co and Ni with MgO (Fig. 5), elements for which olivine is the major host, also indicates a process of mixing olivine and felsic magma but not of olivine fractionation. Dunite has been chosen here as an end-member because of the close similarities in composition between our olivine and that from dunite xenoliths in the Fushan pluton (Xu *et al.*, 2010). Mass-balance calculations show that a total of ~13·5 wt % and 10·5 wt % dunite are needed to be added into a pristine monzodiorite magma (Mg# = 37, represented by an average of CS38 and HK1) to form the bulk compositions of CS17 and CS32, respectively. Because assimilation of dunite alone cannot account for the CaO and TiO_2 contents of the high-Mg diorites, accumulation of some clinopyroxene and amphibole crystals is required. This is obvious in sample CS33-1, which is rich in amphibole and contains the highest CaO and TiO_2 contents. For the modelled samples (Electronic Appendix 6) we estimate that about 9% of clinopyroxene and 5–6% of amphibole are formed by reaction (2). The amount of dissolved olivine is about 3 ± 0·5 wt %, calculated from the Mg# difference between the pristine magma and the hybridized liquid assumed to be in equilibrium with the rim of olivine (Mg# ~75), using an olivine–melt partition coefficient of 0·30 for Fe–Mg (Roeder & Emslie, 1970).

Production of HMAs through assimilation of mantle peridotite by felsic magma has been observed in high-pressure experiments, by infiltrating pristine adakite melt through peridotite (Rapp *et al.*, 1999, 2010; Rapp, 2003). For our samples (Fig. 5), variations in SiO_2, Al_2O_3, FeO, CaO, TiO_2, A/CNK, Cr and Ni are consistent with the changes in melt compositions that were observed by Rapp *et al.* (1999) and Rapp (2003). However, incompatible elements decrease slightly with increasing MgO, contrary to observations in the experiments. According to Rapp *et al.* (1999), the initial melt is partially consumed by reaction with peridotite, leading to an increase of incompatible elements in the hybridized melt. This mechanism does not seem to play an important role in the formation of the high-Mg diorites in this study. Rather, the decrease of SiO_2, Al_2O_3, Na_2O, K_2O and incompatible elements with increasing MgO indicates that simple mixing of an initial monzodiorite melt with dunite played a major role during the assimilation process (see Electronic Appendix 6 for mixing modelling results). Because dunite has negligible incompatible element contents (but very high MgO, Co, Cr and Ni) compared with the initial adakitic liquids, the incompatible element abundances of the hybridized liquids decrease only slightly through dilution of the liquids by addition of dunite (Table 1, Fig. 6).

The role of plagioclase

The presence of plagioclase inclusions and the negative Sr anomaly in the lower Mg# clinopyroxene cores provide evidence that plagioclase was forming during the first stage of crystallization. There is a significant change from a negative to an absent or positive Sr anomaly at the transition from the lower Mg# core to the high-Mg# midsection of inverse-zoned clinopyroxene, indicating that the earlier crystallized plagioclase was consumed during the peridotite assimilation, probably through reaction (2). Plagioclase crystallization started again as documented by the gradual change of Sr anomaly from the midsection to the rim of reversely zoned and from core to rim of normally zoned clinopyroxene. This indicates that plagioclase records mainly the latest stage of the evolution of the diorites after the interaction of the magma with the peridotite.

A mantle-derived mafic original magma has been proposed by Chen *et al.* (2008) for the Han-Xing high-Mg diorites, partially based on patchy zoning (i.e. resorbed An-rich core mantled abruptly by normally zoned Ab-rich rim) of plagioclase phenocrysts. We alternatively interpret the formation of the patchy zoning in terms of an interplay of falling pressure, falling temperature and volatile saturation, as the magma rises from mid-crustal levels to its final shallow emplacement depth. Moreover, the AFC (assimilation–fractionation–crystallization) process proposed by Chen *et al.* (2004, 2008) cannot explain the consistent incompatible element patterns of the rock samples and mineral zoning with highly different Mg# values.

Crustal source for the original magma

The Han-Xing diorite and monzodiorite have εNd (t) (t = 130 Ma) values ranging between −12 and −20 (Chen *et al.*, 2004, 2008; our unpublished data). Such values are similar to that of early Cretaceous lower continental crust beneath the central and eastern NCB, based on the Sm–Nd isotope composition of the exposed Archean amphibolites and granulites in the NCB (Wu *et al.*, 2005*b*; Jiang *et al.*, 2007). The Nd depleted mantle model ages vary between 1·8 and 3·3 Ga, pointing to a magma source with a late Archean–Paleoproterozoic crustal residence time. Moreover, the Han-Xing complex is situated in the central region of the NCB, more than 400 km away from the Qinling–Dabie–Sulu and Central Asian orogenic belts. Therefore, both the Nd isotopic characteristics and tectonic setting indicate that the pristine monzodiorite magma was most probably produced by partial melting of mafic lower crust. Similarly, Mesozoic high-Mg diorites from the eastern part of the NCB have also been interpreted to originate from mafic lower continental crust (Xu *et al.*, 2002; Gao *et al.*, 2004; Xu *et al.*, 2006*b*; Huang *et al.*, 2008).

The Han-Xing monzodiorites have intermediate SiO_2, low MgO, Mg#, Y and HREE values, high Al_2O_3, Sr and Ba contents and Sr/Y and La/Yb ratios (Fig. 7), and are characterized by strong HFSE depletion, positive Sr anomalies and lack of Eu anomalies in mantle-normalized trace element patterns (Fig. 6), similar to adakites (Defant & Drummond, 1990). A number of experiments show that intermediate or felsic magmas with major and trace element characteristics similar to those of adakites and TTGs can be produced by partial melting of mafic rocks (garnet amphibolite, eclogite or granulite) at temperatures ranging from 850 to 1100°C and at pressures higher than ~10 kbar (above the garnet-in reaction curve, which depends on bulk composition; Arth & Hanson, 1972; Rapp *et al.*, 1991; Wyllie & Wolf, 1993; Peacock *et al.*, 1994; Sen & Dunn, 1994; Rapp & Watson, 1995; Springer & Seck, 1997; Skjerlie & Patiño Douce, 2002; Xiong, 2006; Xiao & Clemens, 2007). These adakite melts can be produced by partial melting of either subducting slabs (Defant & Drummond, 1990; Peacock *et al.*, 1994) or thickened lower continental crust (Atherton & Petford, 1993; Petford & Atherton, 1996; Waight *et al.*, 1998; Defant *et al.*, 2002; Rapp *et al.*, 2002; Chung *et al.*, 2003; Stevenson *et al.*, 2005; Wang *et al.*, 2005), which is dominantly mafic in composition (Condie, 1999; Rudnick & Gao, 2003). Stevenson *et al.* (2005) observed adakite generation by partial melting of mafic lower continental crust (granulite, $P = 12$–14 kbar). From all these studies it is clear that the trace element characteristics of the resultant partial melts depend on the residual mineralogy (presence or absence of garnet, plagioclase, amphibole and Ti-phase) as well as on the trace element contents of the rocks that underwent melting. The Nd isotope compositions of the monzodiorites suggest that they were derived from the lower continental crust beneath the NCB. The average lower continental crust is characterized by high Ba, Sr and Sr/Y and strong HFSE depletion (Gao *et al*, 1998; Rudnick & Gao, 2003) (Fig. 6a). Therefore we suggest that the characteristic trace element signature (e.g. high Ba, Sr and Sr/Y and Nb–Ta depletion) of the Han-Xing rocks might be partly inherited from their lower crustal source as has been recently proposed for other examples by Moyen (2009). This hypothesis will be tested with experiments in a subsequent study.

Reversely zoned clinopyroxene and amphibole

Reversely zoned pyroxene crystals, with maximum Mg# values of about 85–90, occur in HMAs from the Setouchi volcanic belt (Kawabata & Shuto, 2005; Tatsumi *et al.*, 2006), Mount Shasta in the Cascades (Streck *et al.*, 2007) and Kadavu Island, Fiji (Danyushevsky *et al.*, 2008). In the Setouchi HMAs, the coexistence of normally and reversely zoned pyroxenes, as well as Mg-rich olivine and quartz have been recognized (Kawabata & Shuto, 2005; Tatsumi *et al.*, 2006). These petrological features were explained by mixing of felsic and mantle-derived mafic (basaltic or HMA) magmas (Kawabata & Shuto, 2005; Tatsumi *et al.*, 2006; Streck *et al.*, 2007; Danyushevsky *et al.*, 2008). However, we do not favor such a model for the petrogenesis of the clinopyroxenes and amphiboles from this study that show similar features. To form sample FS2 (Mg# = 57) by mixing a mafic magma (assuming that MgO = 10 wt %, Mg# ~76) with a felsic magma (represented by monzodiorite HK4, MgO = 1·3 wt %, Mg# ~36), about 23 wt % mafic magma is required. To form the dioritic matrix of sample CS17 (Mg# ~65, after subtracting 5·8 vol. % olivine xenocrysts), about 43 wt % mafic magma is required. A higher percentage of the mafic end-member is required in the above calculations if the mafic magma has lower MgO and Mg#. These proportions of the magma end-member would significantly decouple the incompatible element patterns of the bulk-rocks. The fact that the incompatible element patterns and ratios of the diorite–monzodiorite samples remain relatively consistent (Fig. 6, Table 1) and that the trace element patterns of the mineral zonations remain subparallel (Figs 9–14), despite the highly variable Mg#s, strongly argue against a petrogenesis involving mixing of mafic and felsic magmas. Instead, such petrological and chemical characteristics can be better understood by assimilation of mantle peridotite by the monzodiorite magma as discussed above.

Depth of melt generation, peridotite assimilation and pluton emplacement

Any model for the generation of the high-Mg diorites critically depends on the pressure at which the melts were generated, the depth of interaction with peridotite and the pressure of melt crystallization. The presence of abundant plagioclase inclusions in the cores of reversely zoned clinopyroxene and amphibole crystals, as well as the negative Sr anomaly in the trace element patterns of clinopyroxene and amphibole indicate that the first crystallization stage (before interaction between the original magma and mantle peridotite) occurred in the plagioclase stability field and not under eclogite-facies conditions. Indeed, the cores of reversely zoned clinopyroxenes have low Na_2O (<0·8 wt %) and Al_2O_3 (<3·6 wt %) contents, distinctly different from eclogite pyroxenes. The flat REE pattern in the core of CS17-3 further argues against the involvement of significant garnet, which would sequester the HREE (Klein *et al.*, 2000), during clinopyroxene crystallization. The constant whole-rock Dy/Yb ratios (~2·0) also suggest little or no garnet fractionation (Macpherson *et al.*, 2006; Macpherson, 2008). This is in agreement with the maximum pressure of ~9 kbar obtained from the low-Mg# core of amphibole in sample FS2-1 (Fig. 15). All these observations indicate that the first stage of crystallization occurred at crustal pressures (<10 kbar) rather than at

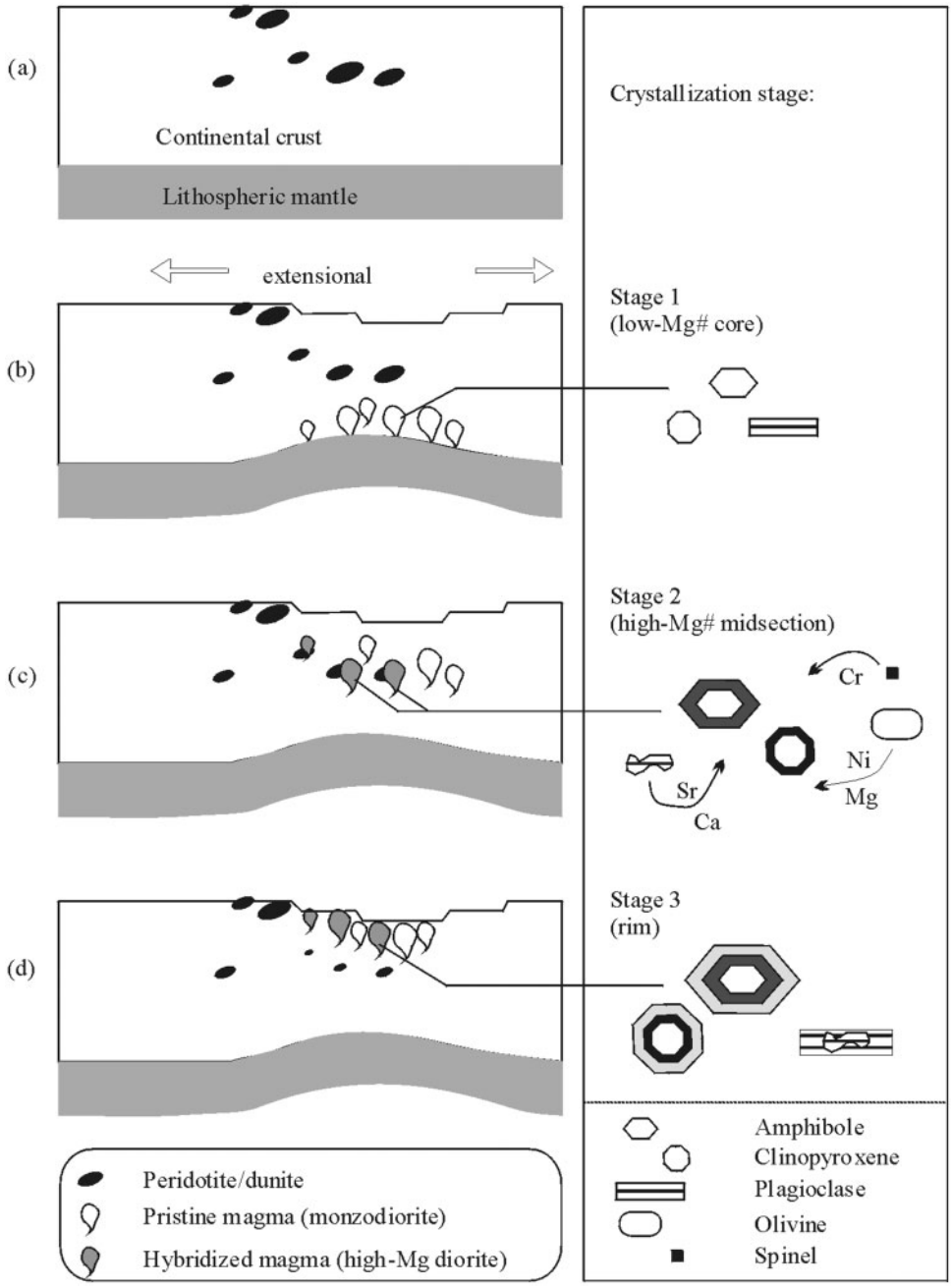

Fig. 17. Schematic illustration of the formation of high-Mg diorite through assimilation of mantle peridotite by felsic magma at crustal depths. Magma evolution processes are recorded by the compositional zonings of clinopyroxene and amphibole, which show three major stages of crystallization.

mantle depths, most probably within the lower crust (Fig. 17).

It is more difficult to constrain the depth of the generation of the original magma. The REE patterns of the recalculated melts assumed to be in equilibrium with the low-Mg# cores of reverse-zoned clinopyroxenes (Fig. 16) do not show significant HREE depletion or fractionation of $(Y/Yb)_N$, indicating that garnet was not a dominant residual phase at the conditions of initial monzodiorite melt generation. On the contrary, amphibole and/or clinopyroxene may be the major residual phase as indicated by the relatively low Y/Yb ratios (9–10) of the bulk-rocks

(Qian, 2001). Together with the εNd (t) values, this provides evidence that the original adakite magma of the Han-Xing diorite–monzodiorite was most probably produced in the lower continental crust at a depth shallower than that required for the stability of eclogite.

Maximum pressures of the second stage of crystallization were estimated from the compositional zoning of amphibole FS2-1, using the Al-in-hornblende geobarometer (Schmidt, 1992). The Al content of the high-Mg# midsection is significantly lower than that of the low-Mg# core and yielded a maximum pressure of ~6·5 kbar (~20 km depth). As outlined above, these calculated pressures represent a maximum because of the higher crystallization temperature of the amphiboles with respect to the experimental calibration (e.g Anderson & Smith, 1995). In any case, the data demonstrate that assimilation of the peridotites occurred at lower pressures than the first stage of crystallization; that is, within the continental crust.

The final magma emplacement depth should be shallower than ~5 km, as is indicated by the pressure estimated for the outer part of the rim of amphibole phenocrysts in sample FS2 as well as for amphibole microcrysts around clinopyroxene (e.g. CS45-1) or interstitial to plagioclase. This is supported by field observations that the plutons are hypabyssal and intrude into nonmetamorphosed sediments.

PETROGENETIC MODEL

A delamination model has been previously proposed to explain the petrogenesis of the Mesozoic HMAs (including the Han-Xing high-Mg diorites) from the central and eastern parts of the NCB (Gao *et al.*, 2004, 2006; Xu *et al.*, 2006*a*, 2006*b*, 2008, 2009; Huang *et al.*, 2008). In this model, the continental crust of the eastern NCB was thickened, and the mafic lower crust was eclogitized and delaminated into the underlying mantle lithosphere. The ascending initial adakite liquids from partial melting of the delaminated eclogitic rocks reacted with the surrounding mantle peridotite, thus gaining their high-Mg character. This model is clearly incompatible with our observation that melt generation and the first stage of crystallization, as well as the assimilation of peridotite, all occurred at crustal levels. Therefore at least for the Han-Xing high-Mg diorites the delamination model is not valid and an alternative model is required.

Figure 17 summarizes the observed stages of magma evolution and mineral crystallization and our interpretation of the tectonic activity that resulted in the formation of the Han-Xing dioritic complex. First, slices of mantle peridotite were obducted and incorporated into the middle–upper crust during an early orogenic event, most probably the formation of the Trans-North China Orogen (Fig. 17a). More than 10 peridotite lenses of several to about a hundred meters in diameter crop out within the late Archean Zanhuang group 25–30 km to the NW of the Fushan pluton, extending northeastward for a distance of more than 30 km (BGHP, 1972). Although the original petrologic characteristics and tectonic setting of these ultramafic rocks are not known, their outcrop confirms the existence of peridotites at crustal levels in the region (central NCB). According to Zhao *et al.* (2001, 2005), the eastern block of the NCB faced a major ocean to the west in the late Archean to early Paleoproterozoic, and the east-dipping subduction of oceanic crust beneath the western margin of the Eastern Block resulted in the formation of magmatic arcs, which were then incorporated into the Trans-North China Orogen during a collisional event at ~1·8 Ga. This is consistent with the Late Archean to Paleoproterozoic Re-depletion model ages of the xenoliths in the Han-Xing high-Mg diorites. Whether or not these peridotite bodies in the Zanhuang group resemble the mantle xenoliths in the Han-Xing complex and cratonic mantle lithosphere beneath the Mesozoic NCB in terms of their petrological and geochemical characteristics needs to be tested in future.

Second, the pristine monzodiorite melt was produced in the early Cretaceous by partial melting of the lower crust in an extensional tectonic setting (Fig. 17b). The resultant magma batches ascended, preferentially following pre-existing faults, to middle or upper crustal depths where some of them interacted with previously emplaced peridotite bodies (Fig. 17c), allowing assimilation of peridotite at crustal depths. During this stage, the peridotitic olivine and spinel and the earlier crystallized plagioclase were consumed, and the high-Mg# portions of the reversely and normally zoned clinopyroxene and amphibole crystals crystallized. Finally, the magma batches, some of which have been hybridized by assimilation of mantle peridotite, were emplaced and crystallized at a shallow crustal level, forming the coexisting high-Mg diorite and monzodiorite plutons (Fig. 17d), which have similar incompatible element but highly variable MgO, Cr and Ni concentrations. This model explains not only the general trend of the plutons becoming more felsic from west to east, but also the juxtaposition of coeval olivine-bearing high-Mg diorite and monzodiorite plutons locally.

Our petrogenetic model for the Han-Xing high-Mg diorites might be valid also for other HMAs in the eastern NCB. The La/Yb and Sr/Y ratios of most of the high-Mg diorites from Han-Xing and the eastern part of the NCB are identical (Table 4). The relative flat HREE patterns do not indicate an eclogitic residue (Fig. 18). As has been pointed out by Moyen (2009), the high Ba, Sr and Sr/Y characteristics may be partially inherited from the source (lower crust) and do not necessarily indicate delamination. Interestingly, mantle peridotites are also present in the Archean basement close to the Tietonggou HMA pluton in western Shandong province (BGSP, 1992), allowing the

Table 4: Average compositions for high-Mg diorites from Han-Xing and the eastern part of the NCB and sanukitoids from the Setouchi volcanic belt and Archean terranes

	High-Mg diorite, NCB				Sanukitoid									
	Han-Xing $n=31$		ENCB $n=28$		Martin05 $n=31$		Superior $n=36$		Pilbara $n=4$		Baltic $n=41$		Setouchi $n=97$	
	av.	SD	av.	SD	av.	SD	av.	SD	av.	SD	av.	SD	av.	SD
SiO_2	56·34	2·89	59·33	2·16	58·76	2·90	57·37	3·35	61·14	1·22	58·25	2·65	58·89	2·62
TiO_2	0·67	0·18	0·71	0·19	0·74	0·30	0·67	0·20	0·57	0·05	0·67	0·11	0·60	0·12
Al_2O_3	15·87	1·63	15·53	0·98	15·80	0·90	15·67	1·12	14·52	0·35	15·93	1·71	16·04	0·69
Fe_2O_3	7·72	1·26	6·54	1·28	5·87	1·50	6·55	1·96	6·99	0·97	6·92	1·34	5·80	0·99
MnO	0·10	0·03	0·10	0·02	0·09	0·02	0·10	0·03	0·09	0·02	0·11	0·02	0·11	0·02
MgO	4·79	3·44	4·10	1·33	3·90	1·30	4·91	1·76	4·15	0·86	4·72	1·59	6·50	1·57
CaO	5·80	1·19	5·32	1·03	5·57	1·50	6·17	1·70	4·92	0·39	5·47	1·33	5·98	0·92
Na_2O	4·63	1·32	4·28	1·20	4·42	0·70	4·47	0·81	3·79	0·16	4·29	0·81	3·37	0·44
K_2O	2·50	0·83	2·04	0·94	2·78	0·80	2·94	0·91	2·09	0·24	2·44	0·94	1·83	0·28
P_2O_5	0·31	0·05	0·25	0·08	0·39	0·10	0·42	0·13	0·31	0·09	0·35	0·14	0·16	0·02
Mg#	52·4	13·0	59·8	7·9			0·59	0·1	0·54	0·03	0·57	0·05	0·69	0·02
A/CNK	0·76	0·08	0·83	0·09	0·77		0·73	0·11	0·83	0·05	0·82	0·12	0·87	0·07
Li	11·1	6·08	18·9	7·51										
Sc	15·2	6·86	14·7	4·21			9·64	1·28	12·8	1·5	16·6	6·5	21·4	2·8
V	153	50	120	34		19	93	42	102	4	121	29		
Cr	138	194	183	123		85	159	133	181	50	192	121	451	155
Co	22·6	13·2	35·2	21·9			24·8	9·5			22·3	6·8	35·8	5·0
Ni	99·3	142	96·4	88·5	72·0	35·0	99·9	56·8	91·0	26·7	84·9	51·3	162	44
Ga	47·8	40·0	18·6	1·8			21·7	2·0	17·2	0·5	26·8	4·47		
Rb	43·5	22·8	49·9	26·9	65·0	22·0	60·2	22·5	93·3	11·0	78·0	43·9	76·9	7·5
Sr	741	109	733	238	1170	638	1387	532	544	60	877	465	315	11
Y	17·1	1·8	15·6	3·0	18·0	11·0	20·0	10·0	17·1	2·4	17·6	5·6	13·8	0·9
Zr	136	29	157	48	165	129	149	64	142	11	144	61	118	9
Nb	6·07	1·09	6·87	1·53	10·0	8·00	7·26	2·63	6·65	1·25	5·69	2·76	5·63	0·56
Cs	0·63	0·58	4·72	5·19					5·43	2·43			5·74	0·96
Ba	1126	371	934	500		563	1686	583	896	174	1088	580	346	73
La	31	6	29	13	60	28	74	29	49	9	41	17	13	3
Ce	60	11	58	22	126	47	119	49	98	23	83	36	26	5
Pr	7·31	0·98	6·87	2·53					11·4	3·21	9·69	3·90	3·30	0·10
Nd	28·7	3·6	26·6	9·1	54·8	16·0	62·1	16·2	43·3	13·9	40·8	16·1	12·9	0·4
Sm	5·49	0·57	4·76	1·24	9·80	3·00	10·7	2·71	6·03	0·78	6·82	2·62	2·79	0·44
Eu	1·73	0·18	1·38	0·34	2·30	0·62	2·63	0·62	1·60	0·20	1·65	0·74	0·85	0·14
Gd	4·60	0·57	3·98	0·99	6·00	1·40	7·02	2·18	4·67	0·40	5·49	2·03	2·57	0·04
Tb	0·63	0·07	0·55	0·14					0·63	0·06	0·67	0·21	0·45	0·06
Dy	3·39	0·41	2·91	0·65	3·20	0·80	3·40	1·14	2·90	0·26	3·07	0·97	2·44	0·04
Ho	0·66	0·08	0·56	0·12			0·68	0·36	0·57	0·06	0·55	0·16	0·50	0·01
Er	1·84	0·22	1·53	0·32	1·41	0·50	1·48	0·71	1·50	0·17	1·41	0·47	1·45	0·04
Tm	0·27	0·03	0·23	0·04			0·20	0·14			0·20	0·07	0·21	0·01
Yb	1·75	0·19	1·46	0·28	1·32	0·70	1·18	0·60	1·30	0·10	1·30	0·40	1·53	0·15
Lu	0·26	0·03	0·23	0·04	0·26	0·10			0·20	0·00	0·19	0·06	0·23	0·03
Hf	3·73	0·76	4·23	1·11			3·24	1·38			3·36	1·46	2·95	0·13
Ta	0·34	0·07	0·49	0·12			0·40	0·21	0·60	0·17	0·27	0·15	0·43	0·03
Pb	7·60	3·13	15·7	7·59			17·1	11·0	17·9	3·66	24·6	8·41	21·1	2·36
Th	3·45	1·06	6·19	2·71			7·26	3·34	10·4	2·15	6·63	4·35	6·45	0·78
U	0·89	0·31	2·14	1·64			1·61	0·93	2·65	0·70	1·08	0·72	2·16	0·12
Nb/La	0·20	0·04	0·26	0·07			0·09	0·04	0·14	<0·01	0·15	0·08	0·36	0·01
La/Yb	18	4	20	7·7			90	49	34	2	32	14	8	2
Sr/Y	44	7	51	23			82	64	32	3	53	25	23	2
Dy/Yb	1·9	0·1	2·0	0·1			3·4	0·8	2·2	0·1	2·4	0·4	1·8	0·03

Samples with SiO_2 <62 wt % have been chosen for the calculation. SD, standard deviation. Data sources are the same as in Fig. 4. ENCB, eastern part of the North China block. Martin05, cited from Martin *et al.* (2005).

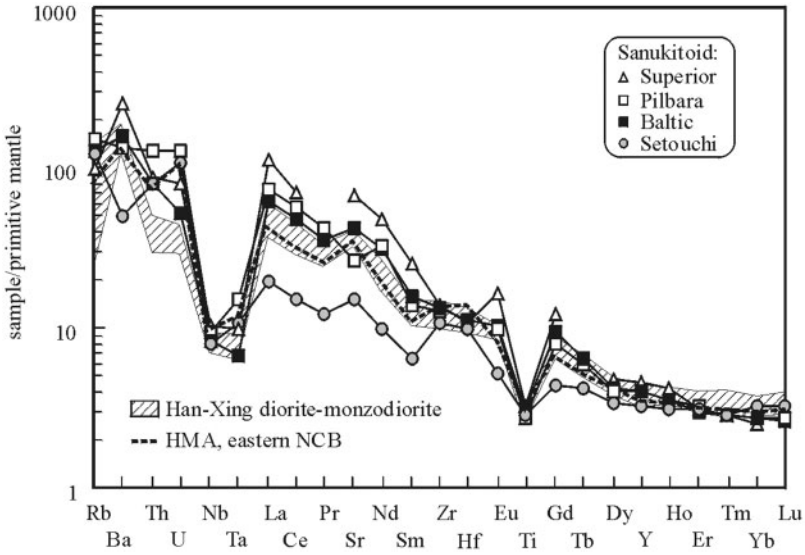

Fig. 18. Primitive mantle-normalized incompatible element patterns, illustrating the comparison between the Han-Xing diorite–monzodiorites and the average compositions of high-Mg adakites from the eastern NCB (Gao *et al.*, 2004; Xu *et al.*, 2006*a*, 2006*b*, 2008; Huang *et al.*, 2008), Miocene sanukitoids from the Setouchi volcanic belt, Japan (Tatsumi & Ishizaka, 1982*a*, 1982*b*; Tatsumi *et al.*, 2006), and Archean sanukitoids from the Superior Province (Shirey & Hanson, 1984; Stern *et al.*, 1989; Stern & Hanson, 1991; Stevenson *et al.*, 1999), the Pilbara Craton (Smithies & Champion, 2000) and the Baltic Shield (Lobach-Zhuchenko *et al.*, 2005, 2008; Heilimo *et al.*, 2010). Average data are listed in Table 4. Normalization data are after Sun & McDonough (1989).

possibility of reaction beween pristine adakite melt and peridotite at crustal depths, similar to the circumstances of the Han-Xing complex and some high-Mg adakites from magmatic arcs (Payot *et al.*, 2007; Streck *et al.*, 2007; Grégoire *et al.*, 2008). It has to be evaluated in future studies whether or not the HMAs from the eastern NCB are similar to the Han-Xing high-Mg diorites in terms of their petrogenesis.

Comparison of Han-Xing high-Mg diorite with high-Mg adakite, Setouchi sanukitoid and Archean sanukitoid, and implications for crust evolution

Three distinct models have been proposed for the generation of HMAs that are related to different tectonic settings and that have contrasting implications for crust formation. Melting of an enriched mantle source that has been metasomatized by slab-derived melts, such as proposed for sanukitoids from the Setouchi volcanic belt, Japan and from late Archean terranes represents new crust formation in a subduction zone environment (Shirey & Hanson, 1984; Stern *et al.*, 1989; Tatsumi, 2008). In a second model HMAs are produced by hybridization of slab-derived melts with olivine-bearing peridotite in the mantle wedge (Kay, 1978; Kelemen, 1995; Yogodzinski *et al.*, 1995; Rapp *et al.*, 1999, 2010). As the source of the initial partial melt is within the subducted crustal rocks, this process represents crustal recycling. Classical examples of this process are some of the circum-Pacific high-Mg adakites (e.g. Kay, 1978; Yogodzinski *et al.*, 1995; Stern & Kilian, 1996). A third model unrelated to subduction has been proposed for HMAs that occur in an intracratonic setting such as the NCB (Gao *et al.*, 2004; Xu *et al.*, 2006*a*, 2006*b*, 2008, 2009; Huang *et al.* 2008). This model proposes that delamination of lower crust leads to partial melting under eclogite-facies conditions and that the resultant melts then interact with the peridotite that replaces the removed thickened lower crust. Therefore, this model is characterized by a net loss of crustal material. We have proposed a fourth model in which partial melting of the lower crust produces monzodiorite melts that interact with ultramafic rocks that have previously been emplaced within the crust. This model represents intra-crustal differentiation. In this section we evaluate if the rocks produced by these different processes display distinct chemical characteristics. The comparison with Archean sanukitoids then shows to what extent the tectonic environment in the Archean can be reconstructed using bulk-rock characteristics.

Major and trace element compositions of the Han-Xing diorites are compared with those of the Setouchi sanukitoids, circum-Pacific adakites and high-Mg diorites of the NCB, as well as Archean sanukitoids, in total alkali–SiO_2 (Fig. 4a), Sr/Y–Y, Yb–Al_2O_3, $(La/Yb)_N$–Yb_N and Ba–Sr diagrams (Fig. 7). The fields defined for these various rock suites, especially those of the circum-Pacific adakites and Archean sanukitoids, overlap significantly. The most distinct and restricted fields are defined by the Setouchi

sanukitoids, which have low Sr and Ba contents, and low Sr/Y and La/Yb. There are some distinct differences between late Archean sanukitoids and the Miocene sanukitoids from the Setouchi volcanic belt, Japan, in terms of major and trace elements (see Figs 4, 5 and 7). As has been noted by Shirey & Hanson (1984) and Stern *et al.* (1989), Archean sanukitoids have lower MgO, Cr and Ni, and higher Na_2O, K_2O, Sr and LREE abundances and LREE/HREE ratios, compared with the Setouchi sanukitoids. The Setouchi sanukitoids also tend to have higher Yb and lower Sr/Y, but these values are still within the range of Archean sanukitoids (Fig. 7a–c). The $(La/Yb)_N$ ratio is conspicuously lower for the Setouchi sanukitoids (4–9) than for Archean sanukitoids (>10) (Fig. 7c). The Han-Xing rocks tend to be lower in Al_2O_3 and higher in K_2O/Na_2O, K_2O+Na_2O, Y, Yb and Ba compared with the circum-Pacific adakites, but fall well within the range of Archean sanukitoids in terms of these values (Figs 4 and 7). Most of the high-Mg diorites from the eastern part of the NCB overlap with the Han-Xing diortites, apart from a few samples that have lower Y, Yb and higher Sr/Y. The latter signature may be achieved from a variety of processes: deeper melting with more abundant residual garnet, interaction of felsic melts with mantle peridotite, and magmatic processes such as AFC involving fractionation of garnet at lower crustal depths (Macpherson *et al.*, 2006; Alonso-Perez *et al.*, 2009; Moyen, 2009). Alternatively, such a signature might be partially inherited from the magma source (Moyen, 2009).

The similarity between the Han-Xing suite, high-Mg adakites from the eastern NCB, and sanukitoids from the Archean terranes (the Superior Province, the Pilbara Craton and the Baltic Shield) are evident when average bulk-rock compositions (Table 4) are compared in primitive mantle-normalized trace element diagrams (Fig. 18). Only samples with $\leq$62 wt % SiO_2 have been selected to depress the effects of possible differentiation. The Han-Xing diorite–monzodiorite samples are similar to the high-Mg adakites from the eastern NCB and Archean sanukitoids from the Pilbara Craton and the Baltic Shield, in terms of average major and trace element contents (e.g. MgO, TiO_2, Al_2O_3, Na_2O, K_2O, P_2O_5, Cr, Ni, Sr, Ba, La, Zr, Y and Sr/Y) and incompatible trace element patterns. The differences are within a factor of ~2, demonstrating the overall geochemical similarities between these average rock compositions. Archean sanukitoids from the Superior Province, Canada, have the highest average Sr, Ba, La and Y and lowest Yb contents and consequently a higher Y/Yb. In contrast, the Setouchi sanukitoids are more than two times lower in average La, Sr and Ba contents and La/Yb, relative to the Archean sanukitoids and the Han-Xing rocks.

As has been pointed out by Martin *et al.* (2005) and shown by the above comparison, Archean sanukitoids are compositionally similar to high-Mg adakites. Magmas with major and trace element compositions similar to adakites can be produced not only by partial melting of subducting slabs, but also by partial melting of lower continental crust in intracontinental settings (e.g. Zhang *et al.*, 2001; Xu *et al.*, 2002; Chung *et al.*, 2003; Wang *et al.*, 2005). In this study we have shown that high-Mg diorites with similar geochemical characteristics can form unrelated to subduction in a cratonic setting. Therefore, caution is needed in using a typical chemical 'adakite-signature', as present in sanukitoids, as direct evidence for subduction processes. Indeed, late Archean sanukitoids generally appear to have formed in late- to post-orogenic or anorogenic settings, and are not directly linked to contemporaneous subduction (Stern *et al.*, 1989; Stevenson *et al.*, 1999; Smithies & Champion, 2000; Whalen *et al.*, 2004; Bibikova *et al.*, 2005; Lobach-Zhuchenko *et al.*, 2005, 2008; Heilimo *et al.*, 2010). Considering the close geochemical similarities between the Han-Xing rocks and Archean sanukitoids, we suggest that our petrogenetic model for the Han-Xing high-Mg diorites should be considered for the generation of some of the Archean sanukitoids. Our model requires that peridotites were incorporated into lower to mid-crustal levels prior to partial melting of the lower crust. Although it is possible that this might happen through tectonic activity, we consider it more likely that ultramafic layers formed as deep-seated cumulates related to extensive mafic to ultramafic magmatism in Archean times, as Archean sanukitoids are commonly associated with mafic and/or ultramafic rocks (e.g. komatiite) (Stern *et al.*, 1989; Stern & Hanson, 1991; Smithies *et al.*, 2004; Lobach-Zhuchenko *et al.*, 2005). If late Archean sanukitoids formed during partial melting and ultramafic rock assimilation at crustal depths, as proposed here for the genesis of the Mesozoic Han-Xing diorite–monzodiorite, then they document crustal fractionation through anatexis—similar to TTG—rather than crust destruction through lower crust delamination or crustal growth by partial melting of enriched mantle peridotite.

CONCLUSIONS

The petrology, bulk-rock geochemistry, compositional zoning of clinopyroxene and amphibole crystals, and compositions of mineral inclusions from the cores of reversely zoned clinopyroxenes collectively document that the early Cretaceous Han-Xing high-Mg diorites from the central North China block were formed by assimilation of mantle peridotite by felsic monzodiorite magma at crustal depths.

Trace element traverses of reversely zoned clinopyroxenes and amphiboles document three major stages of crystallization. Cumulus clinopyroxene, amphibole and minor plagioclase crystallized from a monzodiorite melt during the first stage at lower to mid-crustal pressures. Neither the original melt nor the cumulus clinopyroxene displays

significant HREE depletion, indicating that garnet was not a major phase during the partial melting event and cumulate formation. The second stage of crystallization is characterized by high-Mg# clinopyroxene and amphibole midsections with high Cr and Ni contents, related to the assimilation of peridotite material. The maximum depth of the peridotite assimilation was estimated to be ~20 km, using the Al-in-amphibole geobarometer for the high-Mg# midsection of a reversely zoned amphibole, and thus probably occurred at mid-crustal levels. The third stage of crystallization is related to final emplacement at shallow crustal levels.

The formation of high-Mg andesitic rocks requires crust–mantle interaction and has previously been related to three main processes: (1) partial melting of mantle that has been enriched in incompatible elements by crustal melts, mainly in subduction zones; (2) interaction of slab-derived melts with the mantle wedge and variable assimilation of peridotite material; (3) delamination and partial melting of mafic lower crust and interaction with overlying peridotites. The crustal depth of original magma generation, the interaction with peridotite material at mid-crustal levels and the intra-continental setting observed in this study are inconsistent with any of the proposed models for high-Mg andesitic magma genesis. We propose a new model in which the pristine felsic magma was formed by partial melting at lower crustal depths during extension. In a second step, ultramafic material that was previously emplaced in the crust either by tectonic activity or by magmatic processes (as ultramafic cumulates) interacted with the rising pristine magma to produce the high-Mg rocks. The findings of our study might shed light on the petrogenesis of other high-Mg andesitic rocks such as the Mesozoic high-Mg adakites from the eastern part of the North China block and some late Archean sanukitoids.

SUPPLEMENTARY DATA

Supplementary data for this paper are available at *Journal of Petrology* online.

ACKNOWLEDGEMENTS

We are grateful to C. Allen, Q. Mao, Y. G. Ma, F. Brink, G. Hunter, X. D. Jin, H. P. Zhu, H. Y. Li, M. F. Chu, S. L. Chung, C. Y. Lee, T. Y. Lee, Y. H. Lee, Y. M. Luo and J. Q. Wang for arrangement and technical help in LA-ICP-MS, electron microprobe, ICP-MS and XRF analyses. Z. Y. Chu, F. K. Chen, C. F. Li and P. Xiao are appreciated for their help with the Sr–Nd isotope analyses. Discussions with H. St. C. O'Neill, D. H. Green, J. J. Yang, J. H. Guo and W. Lin have been fruitful. Q. Zhang, G. J. Guo and S. L. Zhang participated in part of the fieldwork. T. Falloon, R. Rapp and C. MacPherson are thanked for their constructive reviews, and R. Frost is thanked for his editorial handling and thoughtful suggestions. This work was supported by the National Natural Science Foundation of China (grant numbers 90914008, 40472047, 40872057) and a 2007–2008 Visiting Research Fellowship from the Chinese Academy of Sciences to Q.Q. and by the Australian Research Council to J.H.

REFERENCES

Alonso-Perez, R., Muntener, O. & Ulmer, P. (2009). Igneous garnet and amphibole fractionation in the roots of island arcs: experimental constraints on andesitic liquids. *Contributions to Mineralogy and Petrology* **157**, 541–558.

Anderson, J. L. & Smith, D. R. (1995). The effects of temperature and f_{O2} on the Al-in-hornblende barometer. *American Mineralogist* **80**, 549–559.

Arth, J. G. & Hanson, G. N. (1972). Quartz diorites derived by partial melting of eclogite or amphibolite at mantle depths. *Contributions to Mineralogy and Petrology* **37**, 161–174.

Atherton, M. P. & Petford, N. (1993). Generation of sodium-rich magmas from newly underplated basaltic crust. *Nature* **362**, 144–146.

Ayers, J. C., Dunkle, S., Gao, S. & Miller, C. F. (2002). Constraints on timing of peak and retrograde metamorphism in the Dabie Shan ultrahigh-pressure metamorphic belt, east–central China, using U–Th–Pb dating of zircon and monazite. *Chemical Geology* **186**, 315–331.

BGHP, (1972). *Manual of geological maps (scale 1:200 000) of Zuoquan (J-49-XXX) and Changzhi (J-49-XXXVI), People's Republic of China*, Bureau of Geology, Hebei Province.

BGSP, (1992). *Manual of geological maps (scale 1:200 000) of Tai'An (J-50-34), People's Republic of China*, Bureau of Geology, Shandong Province.

Bibikova, E. V., Petrova, A. & Claesson, S. (2005). The temporal evolution of sanukitoids in the Karelian Craton, Baltic Shield: an ion microprobe U–ThPb isotopic study of zircons. *Lithos* **79**, 129–145.

Blundy, J. D. & Holland, J. B. (1990). Calcic amphibole equilibrium and a new amphibole–plagioclase geothermometer. *Contributions to Mineralogy and Petrology* **104**, 208–224.

Brey, G. P. & Köhler, T. (1990). Geothermobarometry in four-phase lherzolites II. New thermobarometers, and practical assessment of existing thermobarometers. *Journal of Petrology* **31**, 1353–1378.

Chen, B., Jahn, B. M., Arakawa, Y. & Zhai, M. G. (2004). Petrogenesis of the Mesozoic intrusive complexes from the southern Taihang Orogen, North China Craton: elemental and Sr–Nd–Pb isotopic constraints. *Contributions to Mineralogy and Petrology* **148**, 489–501.

Chen, B., Tian, W., Jahn, B. M. & Chen, Z. C. (2008). Zircon SHRIMP U–Pb ages and *in-situ* Hf isotopic analysis for the Mesozoic intrusions in South Taihang, North China craton: Evidence for hybridization between mantle-derived magmas and crustal components. *Lithos* **102**, 118–137.

Chen, L. (2009). Lithospheric structure variations between the eastern and central North China Craton from S- and P-receiver function migration. *Physics of the Earth and Planetary Interiors* **173**, 216–227.

Chen, L. H. & Zhou, X. H. (2005). Subduction-related metasomatism in the thinning lithosphere: Evidence from a composite dunite–orthopyroxenite xenolith entrained in Mesozoic Laiwu high-Mg diorite, North China Craton. *Geochemistry, Geophysics, Geosystems* **6**, Q06008, doi:10.1029/2005GC00938.

Chung, S. L., Liu, D. Y., Ji, J. Q., Chu, M. F., Lee, H. Y., Wen, D. J., Lo, C. H., Lee, T. Y., Qian, Q. & Zhang, Q. (2003). Adakites from

continental collision zones: melting of thickened lower crust beneath southern Tibet. *Geology* **31**, 1021–1024.

Condie, K. C. (1999). Mafic crustal xenoliths and the origin of the lower continental crust. *Lithos* **46**, 95–101.

Danyushevsky, L. V., Falloon, T. J., Crawford, A. J., Tetroeva, S. A., Leslie, R. L. & Verbeeten, A. (2008). High-Mg adakites from Kadavu Island Group, Fiji, southwest Pacific: Evidence for the mantle origin of adakite parental melts. *Geology* **36**, 499–502.

Defant, M. J. & Drummond, M. S. (1990). Derivation of some modern arc magmas by melting of young subducted lithosphere. *Nature* **347**, 662–665.

Defant, M. J., Clark, L. F., Stewart, R. H., Drummond, M. S., de Boer, J. Z., Maury, R. C., Bellou, H., Jackson, T. E. & Restrepo, J. F. (1991*a*). Andesite and dacite genesis via contrasting processes: the geology and geochemistry of El Valle volcano, Panama. *Contributions to Mineralogy and Petrology* **106**, 309–324.

Defant, M. J., Richerson, P. M., de Boer, J. Z., Stewart, R. H., Maury, R. C., Bellon, H., Drummond, M. S., Feigenson, M. D. & Jackson, T. E. (1991*b*). Dacite genesis via both slab melting and differentiation: petrogenesis of La Yeguada volcanic complex, Panama. *Journal of Petrology* **32**, 1101–1142.

Defant, M. J., Xu, J. F., Kepezhinskas, P., Wang, Q., Zhang, Q. & Xiao, L. (2002). Adakites: some variations on a theme. *Acta Petrologica Sinica* **18**, 129–142.

De Hoog, J. C. M., Gall, L. & Cornell, D. H. (2010). Trace-element geochemistry of mantle olivine and application to mantle petrogenesis and geothermobarometry. *Chemical Geology* **270**, 196–215.

Deng, J. F., Su, S. G., Zhao, G. C. & Liu, C. (2004). Structural elements association of Yanshan orogenic belt, North China. *Geological Journal of China Universities* **10**, 315–323 (in Chinese with English abstract).

Engebretson, D., Cox, A. & Gordon, R. G. (1985). Relative plate motions between ocean and continental plates in the Pacific basin. In: *Geological Society of America, Special Papers* **206**, 1–59.

Gao, S., Luo, T. C., Zhang, B. R., Zhang, H. F., Han, Y. W., Zhao, Z. D. & Hu, Y. K. (1998). Chemical composition of the continental crust as revealed by studies in East China. *Geochimica et Cosmochimica Acta* **62**, 1959–1975.

Gao, S., Rudnick, R. L., Yuan, H. L., Liu, X. M., Liu, Y. S., Xu, W. L., Ling, W. L., Ayers, J., Wang, X. C. & Wang, Q. H. (2004). Recycling lower continental crust in the North China craton. *Nature* **432**, 892–897.

Gao, S., Rudnick, R. L., Xu, W. L., Yuan, H. L., Hu, Z. C. & Liu, X. M. (2006). Lithospheric evolution of the North China Craton: Evidence from high-Mg adakitic rocks and their entrained xenoliths. *Goldschmidt Conference Abstracts* **2006**, A193.

Gao, S., Rudnick, R. L., Xu, W. L., Yuan, H. L., Liu, Y. S., Walker, R. J., Puchtel, I. S., Liu, X. M., Huang, H., Wang, X. R. & Yang, J. (2008). Recyling deep cratonic lithosphere and generation of intraplate magmatism in the North China Craton. *Earth and Planetary Science Letters* **270**, 41–53.

Grégoire, M., Jego, S., Maury, R. C., Polve, M., Payot, B., Tamayo, R. A. & Yumul, G. P., Jr (2008). Metasomatic interactions between slab-derived melts and depleted mantle: Insights from xenoliths within Monglo adakite (Luzon arc, Philippines). *Lithos* **103**, 415–430.

Grove, T. L. & Bryan, W. B. (1983). Fractionation of pyroxene-phyric MORB at low pressure: An experimental study. *Contributions to Mineralogy and Petrology* **84**, 293–309.

Halla, J. (2005). Late Archean high-Mg granitoids (sanukitoids) in the southern Karelian domain, eastern Finland: Pb and Nd isotopic constraints on crust–mantle interactions. *Lithos* **79**, 161–178.

Heilimo, E., Halla, J. & Hölttä, P. (2010). Discrimination and origin of the sanukitoid series: Geochemical constraints from the Neoarchean western Karelian Province (Finland). *Lithos* **115**, 27–39.

Hermann, J., Müntener, O. & Günther, D. (2001). Differentiation of mafic magma in a continental crust-to-mantle transition zone. *Journal of Petrology* **42**, 189–206.

Hirose, K. (1997). Melting experiments on lherzolite KLB-1 under hydrous conditions and generation of high-magnesian andesitic melts. *Geology* **25**, 42–44.

Huang, F. S. & Xue, S. Z. (1990*a*). The petrographical and geochemical characteristics and genesis of the Han Xing intrusive complex. *Acta Petrologica et Mineralogica* **9**, 203–212 (in Chinese with English abstract).

Huang, F. S. & Xue, S. Z. (1990*b*). The discovery of the mantle-derived ultramafic xenoliths in Handan Xingtai intrusive complex and their mineralogical–geochemical characteristics. *Acta Petrologica Sinica* **4**, 40–45 (in Chinese with English abstract).

Huang, F., Li, S. G., Dong, F., He, Y. S. & Chen, F. K. (2008). High-Mg adakitic rocks in the Dabie orogen, central China: Implications for foundering mechanism of lower continental crust. *Chemical Geology* **255**, 1–13.

Jiang, N., Liu, Y. S., Zhou, W. G., Yang, J. H. & Zhang, S. Q. (2007). Derivation of Mesozoic adakitic magmas from ancient lower crust in the North China craton. *Geochimica et Cosmochimica Acta* **71**, 2591–2608.

Jurewicz, A. J. G. & Watson, E. B. (1988). Cations in olivine, Part 1: Calcium partitioning and calcium–magnesium distribution between olivines and coexisting melts, with petrologic applications. *Contributions to Mineralogy and Petrology* **99**, 176–185.

Kamei, A., Owada, M., Nagao, T. & Shiraki, K. (2004). High-Mg diorites derived from sanukitic HMA magmas, Kyushu Island, southwest Japan arc: evidence from clinopyroxene and whole rock compositions. *Lithos* **75**, 359–371.

Kawabata, H. & Shuto, K. (2005). Magma mixing recorded in intermediate rocks associated with high-Mg andesites from the Setouchi volcanic belt, Japan: implications for Archean TTG formation. *Journal of Volcanology and Geothermal Research* **140**, 241–271.

Kawasaki, T., Okusako, K. & Nishiyama, T. (1993). Anhydrous and water-saturated melting experiments of an olivine andesite from Mt Yakushi-Yama, northeastern Shikoku, Japan. *Island Arc* **2**, 228–237.

Kay, R. W. (1978). Aleutian magnesian andesites: melts from subducted Pacific ocean crust. *Journal of Volcanology and Geothermal Research* **4**, 117–132.

Kay, R. W. & Kay, S. M. (1991). Creation and destruction of lower continental crust. *Geologische Rundschau* **80**, 259–278.

Kay, R. W. & Kay, S. M. (1993). Delamination and delamination magmatism. *Tectonophysics* **219**, 177–189.

Kelemen, P. B. (1995). Genesis of high Mg# andesites and the continental crust. *Contributions to Mineralogy and Petrology* **120**, 1–19.

Klein, M., Stosch, H. G., Seck, H. A. & Shimizu, N. (2000). Experimental partitioning of high field strength and rare earth elements between clinopyroxene and garnet in andesitic to tonalitic systems. *Geochimica et Cosmochimica Acta* **64**, 99–115.

Kovalenko, A., Clemens, J. D. & Savatenkov, V. (2005). Petrogenetic constraints for the genesis of Archaean sanukitoid suites: geochemistry and isotopic evidence from Karelia, Baltic Shield. *Lithos* **79**, 147–160.

Kushiro, I. (1974). Melting of hydrous upper mantle and possible generation of andesitic magma: an approach from synthetic systems. *Earth and Planetary Science Letters* **22**, 294–299.

Kushiro, I. (2007). Origin of magmas in subduction zones: a review of experimental studies. *Proceedings of the Japan Academy, Series B* **83**, 1–15.

Leake, B. E., Woolley, A. R., Arps, C. E. S. *et al.* (1997). Nomenclature of amphiboles: report of the subcommittee on amphiboles of the international mineralogical association, commission on new minerals and minerals names. *Canadian Mineralogist* **35**, 219–246.

Li, S. G., Jagoutz, E., Chen, Y. Z. & Li, Q. L. (2000). Sm–Nd and Rb–Sr isotopic chronology and cooling history of ultrahigh pressure metamorphic rocks and their country rocks at Shuanghe in the Dabie Mountains, Central China. *Geochimica et Cosmochimica Acta* **64**, 1077–1093.

Libourel, G. (1999). Systematics of calcium partitioning between olivine and silicate melt: implications for melt structure and calcium content of magmatic olivines. *Contributions to Mineralogy and Petrology* **136**, 63–80.

Lin, W., Faure, M., Monie, P. & Wang, Q. C. (2007). Polyphase Mesozoic tectonics in the eastern part of the North China Block: insights from the eastern Liaoning Peninsula massif (NE China). In: Zhai, M. G., Windley, B. F., Kusky, T. M. & Meng, Q. R. (eds) *Mesozoic Sub-Continental Lithospheric Thinning under Eastern Asia. Geological Society, London, Special Publications* **280**, 153–170.

Lin, W., Faure, M., Monie, P., Schärer, U. & Panis, D. (2008). Mesozoic extensional tectonics in eastern Asia; the south Liaodong Peninsula metamorphic core complex (NE China). *Journal of Geology* **116**, 134–154.

Liu, J. L., Davis, G. A., Ji, M., Guan, H. M. & Bai, X. D. (2008). Crustal detachment and destruction of the North China craton: constraints from late Mesozoic extensional structures. *Earth Science Frontiers* **15**, 72–81 (in Chinese with English abstract).

Lobach-Zhuchenko, S. B., Rollinson, H., Chekulaev, V. P., Arestova, N. A., Kovalenko, A. V., Ivanikov, V. V., Guseva, N. S., Sergeev, S. A., Matukov, D. I. & Jarvis, K. E. (2005). The Archaean sanukitoid series of the Baltic Shield: geological setting, geochemical characteristics and implications for their origin. *Lithos* **79**, 107–128.

Lobach-Zhuchenko, S. B., Rollinson, H., Chekulaev, V. P., Savatenkov, V. M., Kovalenko, A. V., Martin, H., Guseva, N. S. & Arestova, N. A. (2008). Petrology of a late Archaean, highly potassic sanukitoid pluton from the Baltic Shield: insights into late Archaean mantle metasomatism. *Journal of Petrology* **49**, 393–420.

Ma, X. Y. (1989). *Lithospheric dynamics map of China and adjacent seas (scale 1:4 000 000) and explanatory notes*. Beijing: Geological Publishing House.

Macpherson, C. G. (2008). Lithosphere erosion and crustal growth in subduction zones: Insights from initiation of the nascent East Philippine Arc. *Geology* **36**, 311–314.

Macpherson, C. G., Dreher, S. T. & Thirlwall, M. F. (2006). Adakites without slab melting: High pressure differentiation of island arc magma, Mindanao, the Philippines. *Earth and Planetary Sciences Letters* **243**, 581–593.

Martin, H. (1987). Petrogenesis of Archaean trondhjemites, tonalites, and granodiorites from Eastern Finland: major and trace element geochemistry. *Journal of Petrology* **28**, 921–953.

Martin, H., Chauvel, C. & Jahn, B. M. (1983). Major and trace element geochemistry and crustal evolution of Archaean granodioritic rocks from eastern Finland. *Precambrian Research* **21**, 159–180.

Martin, H., Smithies, R. H., Rapp, R., Moyen, J.-F. & Champion, D. (2005). An overview of adakite, tonalite–trondhjemite–granodiorite (TTG), and sanukitoid: relations and some implications for crustal evolution. *Lithos* **79**, 1–24.

Maruyama, S., Isozaki, Y., Kimura, G. & Terabayashi, M. (1997). Paleogeographic maps of the Japanese Islands: Plate tectonic synthesis from 750 Ma to the present. *Island Arc* **6**, 121–142.

Middlemost, E. A. K. (1994). Naming materials in the magma/igneous rock system. *Earth-Science Reviews* **37**, 215–224.

Morris, P. A. (1995). Slab melting as an explanation of Quaternary volcanism and aseismicity in southwest Japan. *Geology* **23**, 395–398.

Moyen, J. F. (2009). High Sr/Y and La/Yb ratios: The meaning of the 'adakitic signature'. *Lithos* **112**, 556–574.

Moyen, J. F., Martin, H., Jayananda, M. & Auvray, B. (2003). Late Archaean granites: a typology based on the Dharwar Craton (India). *Precambrian Research* **127**, 103–123.

Mysen, B. & Boettcher, A. L. (1975). Melting of a hydrous mantle: II. Geochemistry of crystals and liquids formed by anatexis of mantle peridotite at high pressure and high temperatures as a function of controlled activities of water, hydrogen, and carbon dioxide. *Journal of Petrology* **16**, 549–593.

Payot, B. D., Jego, S., Maury, R. C., Polve, M., Grégoire, M., Ceuleneer, G., Tamayo, R. A., Jr, Yumul, , G., P., Jr, Bellon, H. & Cotton, J. (2007). The oceanic substratum of Northern Luzon: Evidence from xenoliths within Monglo adakite (the Philippines). *Island Arc* **16**, 276–290.

Peacock, S. M., Rushmer, T. & Thompson, A. B. (1994). Partial melting of subducting oceanic crust. *Earth and Planetary Science Letters* **121**, 227–244.

Petford, N. & Atherton, M. (1996). Na-rich partial melts from newly undeplated basaltic crust: the Cordillera Blanca Batholith, Peru. *Journal of Petrology* **37**, 1491–1521.

Qian, Q. (2001). Adakite: geochemical characteristics and genesis. *Acta Petrologica et Mineralogica* **20**, 297–306 (in Chinese with English abstract).

Qian, Q., O'Neill, H. St. C. & Hermann, J. (2010). Comparative diffusion coefficients of major and trace elements in olivine at ~950°C from a xenocryst included in dioritic magma. *Geology* **38**, 331–334.

Rapp, R. P. (2003). Experimental constraints on the origin of compositional variations in the adakite–TTG–sanukitoid–HMA family of granitoids. *Geophysical Research Abstracts* **5**, abstract 08123.

Rapp, R. P. & Watson, E. B. (1995). Dehydration melting of metabasalt at 8–32 kbar: Implications for continental growth and crust–mantle recycling. *Journal of Petrology* **36**, 891–931.

Rapp, R. P., Watson, E. B. & Miller, C. F. (1991). Partial melting of amphibolite/eclogite and the origin of Archean trondhjemites and tonalites. *Precambrian Research* **51**, 1–25.

Rapp, R. P., Shimizu, N., Norman, M. D. & Applegate, G. S. (1999). Reaction between slab-derived melts and peridotite in the mantle wedge: experimental constraints at 3·8 GPa. *Chemcial Geology* **160**, 335–356.

Rapp, R. P., Xiao, L. & Shimizu, N. (2002). Experimental constraints on the origin of potassium-rich adakites in eastern China. *Acta Petrologica Sinica* **18**, 293–302.

Rapp, R. P., Norman, M. D., Laporte, D., Yaxley, G. M., Martin, H. & Foley, S. F. (2010). Continental formation in the Archean and chemical evolution of the cratonic lithosphere: Melt–rock reaction experiments at 3–4 GPa and petrogenesis of Archean Mg-diorites. *Journal of Petrology* (in press).

Ratschbacher, L., Hacker, B. R., Webb, L. E., McWilliams, M., Ireland, T., Dong, S. W., Calvert, A., Chateigner, D. & Wenk, H. R. (2000). Exhumation of the ultrahigh-pressure continental crust in east central China: Cretaceous and Cenozoic unroofing and the Tan-Lu fault. *Journal of Geophysical Research* **105(B6)**, 13303–13338.

Roeder, P. L. & Emslie, R. F. (1970). Olivine–liquid equilibrium. *Contributions to Mineralogy and Petrology* **29**, 275–289.

Rudnick, R. L. (1995). Making continental crust. *Nature* **378**, 571–578.

Rudnick, R. L. & Gao, S. (2003). Composition of the continental crust. In: Rudnick, R. L. (ed.) *Treatise on Geochemistry, Vol. 3. The Crust*. In: Amsterdam: Elsevier, pp. 1–64.

Schmidt, M. W. (1992). Amphibole composition in tonalite as a function of pressure: an experimental calibration of the Al-in-hornblende barometer. *Contributions to Mineralogy and Petrology* **110**, 304–310.

Sen, C. & Dunn, T. (1994). Dehydration melting of a basaltic composition amphibolite at 1·5 and 2·0 GPa: Implications for the origin of adakites. *Contributions to Mineralogy and Petrology* **117**, 394–409.

Sengör, A. M. C., Natal'in, B. A. & Burtman, V. S. (1993). Evolution of the Altaid tectonic collage and Palaeozoic crustal growth in Eurasia. *Nature* **364**, 299–307.

Shimizu, Y., Arai, S., Morishita, T., Yurimoto, H. & Gervilla, F. (2004). Petrochemical characteristics of felsic veins in mantle xenoliths from Tallante (SE Spain): an insight into activity of silicic melt within the mantle wedge. *Transactions of the Royal Society of Edinburgh: Earth Sciences* **95**, 265–276.

Shirey, S. B. & Hanson, G. N. (1984). Mantle-derived Archean monzodiorite and trachyandesites. *Nature* **310**, 222–224.

Sisson, T. W. & Grove, T. L. (1993). Experimental investigations of the role of H_2O in calc-alkaline differentiation and subduction zone magmatism. *Contributions to Mineralogy and Petrology* **113**, 143–166.

Skjerlie, K. P. & Patiño Douce, A. E. (2002). The fluid-absent partial melting of a zoisite-bearing quartz eclogite from 1·0 to 3·2 GPa; Implications for melting in thickened continental crust and for subduction processes. *Journal of Petrology* **43**, 291–314.

Smithies, R. H. & Champion, D. C. (2000). The Archaean high-Mg diorite suite: links to tonalite–trondhjemite–granodiorite magmatism and implications for early Archaean crustal growth. *Journal of Petrology* **41**, 1653–1671.

Smithies, R. H., Champion, D. C. & Sun, S. S. (2004). Evidence for early LREE-enriched mantle source regions: diverse magmas from the c. 3·0 Ga Mallina Basin, Pilbara Craton, NW Australia. *Journal of Petrology* **45**, 1515–1537.

Song, X. Y. & Feng, Z. Y. (1999). Minor element geochemistry of Mesozoic magmatic intrusions of southern Taihang Mountains. *Journal of Geology and Mineral Resources of North China* **14**, 1–17 (in Chinese with English abstract).

Springer, W. & Seck, H. A. (1997). Partial fusion of basic granulites at 5 to 15 kbar: implications for the origin of TTG magmas. *Contributions to Mineralogy and Petrology* **127**, 30–45.

Stern, C. R. & Kilian, R. (1996). Role of the subducted slab, mantle wedge and continental crust in the generation of adakites from the Andean Austral Volcanic Zone. *Contributions to Mineralogy and Petrology* **123**, 263–281.

Stern, R. A. & Hanson, G. N. (1991). Archean high-Mg granodiorite: a derivative of light rare earth element-enriched monzodiorite of mantle origin. *Journal of Petrology* **32**, 201–238.

Stern, R. A., Hanson, G. N. & Shirey, S. B. (1989). Petrogenesis of mantle-derived, LILE-enriched Archean monzodiorites and trachyandesites (sanukitoids) in southwestern Superior Province. *Canadian Journal of Earth Sciences* **26**, 1688–1712.

Stern, R. A., Hanson, G. N. & Shirey, S. B. (1990). Petrogenesis of mantle-derived, LILE-enriched Archean monzodiorites and trachyandesites (sanukitoids) in southwestern Superior Province: Reply. *Canadian Journal of Earth Sciences* **27**, 1136–1137.

Stevenson, J. A., Daczko, N. R., Clarke, G. L., Pearson, N. & Klepeis, K. A. (2005). Direct observation of adakite melts generated in the lower continental crust, Fiordland, New Zealand. *Terra Nova* **17**, 73–79.

Stevenson, R., Henry, P. & Gariépy, C. (1999). Assimilation–fractional crystallization origin of Archean sanukitoid suites: Western Superior Province, Canada. *Precambrian Research* **96**, 83–99.

Streck, M. J., Leeman, W. P. & Chesley, J. (2007). High-magnesian andesite from Mount Shasta: A product of magma mixing and contamination, not a primitive mantle melt. *Geology* **35**, 351–354.

Sun, S. S. & McDonough, W. F. (1989). Chemical and isotopic systematics of oceanic basalts: implications for mantle composition and processes. In: Saunders, A. D. & Norry, M. J. (eds) *Magmatism in the Ocean Basins. Geological Society, London, Special Publications* **42**, 313–345.

Tatsumi, Y. (1981). Melting experiments on a high-magnesian andesite. *Earth and Planetary Science Letters* **54**, 357–365.

Tatsumi, Y. (1982). Origin of high-magnesian andesites in the Setouchi volcanic belt, southwest Japan, II. Melting phase relations at high pressures. *Earth and Planetary Science Letters* **60**, 305–317.

Tatsumi, Y. (2008). Making continental crust: The sanukitoid connection. *Chinese Science Bulletin* **53**, 1620–1633.

Tatsumi, Y. & Ishizaka, K. (1981). Existence of andesitic primary magma: an example from southwest Japan. *Earth and Planetary Science Letters* **53**, 124–130.

Tatsumi, Y. & Ishizaka, K. (1982*a*). Origin of high-magnesian andesites in the Setouchi volcanic belt, southwest Japan, I. Petrographical and chemical characteristics. *Earth and Planetary Science Letters* **60**, 293–304.

Tatsumi, Y. & Ishizaka, K. (1982*b*). Magnesian andesite and basalt from Shodo-Shima island, southwest Japan, and their bearing on the genesis of calc-alkaline andesites. *Lithos* **15**, 161–172.

Tatsumi, Y., Nakashima, T. & Tamura, Y. (2002). The petrology and geochemistry of calc-alkaline andesites on Shodo-Shima island, SW Japan. *Journal of Petrology* **43**, 3–16.

Tatsumi, Y., Shukuno, H., Sato, K., Shibata, T. & Yoshikawa, M. (2003). The petrology and geochemistry of high-magnesium andesites at the western tip of the Setouchi volcanic belt, SW Japan. *Journal of Petrology* **44**, 1561–1578.

Tatsumi, Y., Suzuki, T., Kawabata, H., Sato, K., Miyazaki, T., Chang, Q., Takahashi, T., Tani, K., Shibata, T. & Yoshikawa, M. (2006). The petrology and geochemistry of Oto-Zan composite lava flow on Shodo-Shima Island, SW Japan: Remelting of a solidified high-Mg andesite magma. *Journal of Petrology* **47**, 595–629, doi:10.1093/petrology/egi087.

Thompson, R. N. & Gibson, S. A. (2000). Transient high temperatures in mantle plume heads inferred from magnesian olivines in Phanerozoic picrites. *Nature* **407**, 502–506.

Waight, T. E., Weaver, S. D., Muir, R., Maas, R. & Eby, G. N. (1998). The Hohonu batholith of North Westland, New Zealand: granitoid compositions controlled by source H_2O contents and generated during tectonic transition. *Contributions to Mineralogy and Petrology* **130**, 225–239.

Wang, Q., McDermott, F., Xu, J. F., Bellon, H. & Zhu, Y. T. (2005). Cenozoic K-rich adakitic volcanic rocks in the Hohxil area, northern Tibet: Lower-crustal melting in an intracontinental setting. *Geology* **33**, 465–468.

Wang, Y. J., Fan, W. M., Zhang, H. F. & Peng, T. P. (2006). Early Cretaceous gabbroic rocks from the Taihang Mountains: Implications for a paleosubduction-related lithospheric mantle beneath the central North China Craton. *Lithos* **86**, 281–302.

Whalen, J. B., Percival, J. A., McNicoll, V. J. & Longstaffe, F. J. (2004). Geochemical and isotopic (Nd–O) evidence bearing on the origin of late- to post-orogenic high-K granitoid rocks in the Western Superior Province: implications for late Archean tectonomagmatic processes. *Precambrian Research* **132**, 303–326.

Witt-Eickschen, G. & O'Neill, H. St. C. (2005). The effect of temperature on the equilibrium distribution of trace elements between clinopyroxene, orthopyroxene, olivine and spinel in upper mantle peridotite. *Chemical Geology* **221**, 65–101.

Wu, F. Y., Lin, J. Q., Wilde, S. A., Zhang, X. O. & Yang, J. H. (2005*a*). Nature and significance of the Early Cretaceous giant igneous event in eastern China. *Earth and Planetary Science Letters* **233**, 103–119.

Wu, F. Y., Zhao, G. C., Wilde, S. A. & Sun, D. Y. (2005*b*). Nd isotopic constraints on crustal formation in the North China Craton. *Journal of Asian Earth Sciences* **24**, 523–545.

Wu, F. Y., Yang, J. H., Wilde, S. A. & Zhang, X. O. (2005*c*). Geochronology, petrogenesis and tectonic implications of Jurassic granites in the Liaodong Peninsula, NE China. *Chemical Geology* **221**, 127–156.

Wyllie, P. J. & Wolf, M. B. (1993). Amphibolite dehydration-melting: sorting out the solidus. In: Prichard, H. M., Alabaster, T., Harris, N. B. W. & Neary, C. R. (eds) *Magmatic Processes and Plate Tectonics. Geological Society, London, Special Publications* **76**, 405–416.

Xiao, L. & Clemens, J. D. (2007). Origin of potassic (C-type) adakite magmas: Experimental and field constraints. *Lithos* **95**, 399–414.

Xiong, X. L. (2006). Trace element evidence for growth of early continental crust by melting of rutile-bearing hydrous eclogite. *Geology* **34**, 945–948.

Xu, J. F., Shinjo, R., Defant, M. J., Wang, Q. & Rapp, R. P. (2002). Origin of Mesozoic adakitic intrusive rocks in the Ningzhen area of east China: Partial melting of delaminated lower continental crust? *Geology* **30**, 1111–1114.

Xu, J. W., Zhu, G., Tong, W. X., Cui, K. R. & Liu, Q. (1987). Formation and evolution of the Tancheng–Lujiang wrench fault system: a major shear system to the northwest of the Pacific Ocean. *Tectonophysics* **134**, 273–310.

Xu, W. L. & Gao, Y. (1990). Rare earth element geochemistry of intrusive rock series of Yanshan stage from Han-Xing district, Hebei province, China. *Acta Petrologica Sinica* **2**, 43–50 (in Chinese with English abstract).

Xu, W. L. & Lin, J. Q. (1991). The discovery and study of mantle-derived dunite inclusions in hornblende-diorite in the Handan–Xingtai Area, Hebei. *Acta Geologica Sinica* **1**, 30–41 (in Chinese with English abstract).

Xu, W. L., Wang, D. Y., Gao, S. & Lin, J. Q. (2003*a*). Discovery of dunite and pyroxenite xenoliths in Mesozoic diorite at Jinling, western Shandong and its significance. *Chinese Science Bulletin* **48**, 1599–1604.

Xu, W. L., Wang, D. Y., Wang, Q. H. & Lin, J. Q. (2003*b*). Petrology and geochemistry of two types of mantle-derived xenoliths in Mesozoic diorite from western Shandong province. *Acta Petrologica Sinica* **19**, 623–636 (in Chinese with English abstract).

Xu, W. L., Gao, S., Wang, Q. H., Wang, D. Y. & Liu, Y. S. (2006*a*). Mesozoic crustal thickening of the eastern North China craton: Evidence from eclogite xenoliths and petrologic implications. *Geology* **34**, 721–724.

Xu, W. L., Wang, Q. H., Wang, D. Y., Guo, J. H. & Pei, F. P. (2006*b*). Mesozoic adakitic rocks from the Xuzhou–Suzhou area, eastern China: Evidence for partial melting of delaminated lower continental crust. *Journal of Asian Earth Sciences* **27**, 230–240.

Xu, W. L., Hergt, J. M., Gao, S., Pei, F. P., Wang, W. & Yang, D. B. (2008). Interaction of adakitic melt–peridotite: Implications for the high-Mg# signature of Mesozoic adakitic rocks in the eastern North China Craton. *Earth and Planetary Science Letters* **265**, 123–137.

Xu, W. L., Yang, D. B., Pei, F. P., Wang, F. & Wang, W. (2009). Mesozoic lithospheric mantle modified by delaminated lower continental crust in the North China Craton: constraints from compositions of amphiboles from peridotite xenoliths. *Journal of Jilin University (Earth Science Edition)* **39**, 606–617 (in Chinese with English abstract).

Xu, W. L., Yang, D. B., Gao, S., Pei, F. P. & Yu, Y. (2010). Geochemistry of peridotite xenoliths in Early Cretaceous high-Mg# diorites from the Central Orogenic Block of the North China Craton: The nature of Mesozoic lithospheric mantle and constraints on lithospheric thinning. *Chemical Geology* **270**, 257–273.

Xu, Y. G. (2007). Diachronous lithospheric thinning of the North China Craton and formation of Daxin'anling–Taihangshan gravity lineament. *Lithos* **96**, 281–298.

Yang, L. H. & Li, Q. Z. (1980). *Crustal stress field of the North China block*. Beijing: Seismic Publishing House, pp. 1–132 (in Chinese).

Yogodzinski, G. M., Kay, R. W., Volynets, O. N., Koloskov, A. V. & Kay, S. M. (1995). Magnesian andesite in the western Aleutian Komandorsky region: Implications for slab melting and processes in the mantle wedge. *Geological Society of America Bulletin* **107**, 505–519.

Zhang, Q., Qian, Q., Wang, E. Q., Wang, Y., Zhao, T. P., Hao, J. & Guo, G. J. (2001). An East China Plateau in mid–late Yanshanian period: implication from adakites. *Chinese Journal of Geology* **36**, 248–255 (in Chinese with English abstract).

Zhang, S. H., Zhao, Y., Kröner, A., Liu, X. M., Xie, L. W. & Chen, F. K. (2009). Early Permian plutons from the northern North China Block: constraints on continental arc evolution and convergent margin magmatism related to the Central Asian Orogenic belt. *International Journal of Earth Sciences* **98**, 1441–1467.

Zhao, G. C., Sun, M., Wilde, S. A. & Li, S. Z. (2005). Late Archean to Paleoproterozoic evolution of the North China Craton: Key issues revisited. *Precambrian Research* **136**, 177–202.

Zhao, G. C., Wilde, S. A., Cawood, P. A. & Sun, M. (2001). Archean blocks and their boundaries in the North China Craton: lithological, geochemical, structural and *P–T* path constraints and tectonic evolution. *Precambrian Research* **107**, 45–73.

Zheng, T. Y., Chen, L., Zhao, L., Xu, W. W. & Zhu, R. X. (2006). Crust–mantle structure difference across the gravity gradient zone in North China Craton: Seismic image of the thinned continental crust. *Physics of the Earth and Planetary Interiors* **159**, 43–58.

Zhou, X. M. & Li, W. X. (2000). Origin of Late Mesozoic igneous rocks in Southeastern China: implications for lithosphere subduction and underplating of mafic magmas. *Tectonophysics* **326**, 269–287.

Zhu, G., Liu, G. S., Niu, M. L., Song, C. Z. & Wang, D. X. (2003). Transcurrent movement and genesis of the Tan-Lu fault zone. *Geological Bulletin of China* **22**, 200–207 (in Chinese with English abstract).

Zhu, G., Song, C. Z., Wang, D. X., Liu, G. S. & Xu, J. W. (2001). $^{40}Ar/^{39}Ar$ geochronological study on the strike-slip ages of the Tan-Lu fault zone and its tectonic significance. *Science in China (Series D)* **31**, 250–256 (in Chinese).

Zhu, G., Wang, D. X., Liu, G. S., Niu, M. L. & Song, C. Z. (2004). Evolution of the Tan-Lu fault zone and its responses to plate movements in west Pacific basin. *Chinese Journal of Geology* **39**, 36–49 (in Chinese with English abstract).

Zhu, G., Wang, Y. S., Liu, G. S., Niu, M. L., Xie, C. L. & Li, C. C. (2005). $^{40}Ar/^{39}Ar$ dating of strike-slip motion on the Tan-Lu fault zone, East China. *Journal of Structural Geology* **27**, 1379–1398.